Axial vibratory driving installation effects on the monopile response to cyclic lateral loading

In partial fulfilment of the requirements for the degree of
***Master of Science** in Applied Earth Sciences*
Geo-Engineering Track

Department of Civil Engineering and Geosciences,
Section of Geo-Engineering,
Delft University of Technology.

Author:	**Student number**
D. Rosenschein Petrosini	5046629
Assessment Committee:	Dr. ir. E. Kementzetzidis - Chairman and Daily Supervisor. Dr. ir. R.B.J. Brinkgreve - Supervisor. Dr. ir. A. Tsetas - Supervisor.
Date of submission:	June 2024

Delft
University of
Technology

Abstract

In response to the urgent need for sustainable energy sources to combat climate change, offshore wind power has emerged as a promising solution. However, the installation process of offshore wind turbines, particularly the driving of monopile foundations, presents challenges, notably concerning underwater noise pollution and its environmental impacts. This research studies the efficacy of an alternative approach to traditional installation methods: the vibratory pile driving, renowned for its minimized noise impact. It focuses on its effects on the long-term performance of monopiles under cyclic lateral loading, through numerical simulations. By addressing certain uncertainties, the aim of this work is to contribute to optimizing offshore wind turbine installation practices and ensuring the stability and performance of monopile foundations in challenging marine environments.

Two models are integrated and merged to address the previous objectives. The first model simulates the dynamic behaviour of the soil after vibratory installation effects. Meanwhile, the second model analyzes monopile response to lateral loading induced by environmental factors like wind and waves. The *OpenSees* software is employed for the computation of 3D finite element analyses, and the soil, represented as dry, initially dense, Karlsruhe fine sand, is modeled using the SANISAND constitutive model, which relies on the Critical State Soil Mechanics framework, to accurately capture stress and state-dependent behaviour. Only half of the monopile's embedment depth is evaluated, due to computational constraints.

Both the behaviour of the soil after the vibro-installation process and after the lateral loading are evaluated. Significant vertical and radial displacement occurs during pile driving, leading to settlement around the pile shaft and mudline as soil densify. Horizontal displacement patterns indicate an initial outward movement followed by lateral drawing-in towards the pile shaft, driven by soil compaction and rearrangement induced by installation vibrations. Notably, post-installation, there is a marked increase in relative density around the pile shaft, enhancing soil strength and friction, particularly near the pile tip. This densification, along with changes in mean effective stress, significantly affects soil behaviour and sets the stage for subsequent lateral loading.

After the lateral loading stage, the influence of installation on pile response becomes apparent. Post-installation soil conditions profoundly impact lateral displacement patterns, with vibro-installed piles exhibiting larger displacements during initial loading cycles compared to wished-in-place piles. Throughout lateral loading cycles, localized soil densification and remoulding further influence stiffness and displacement patterns. Notably, the relative density changes reflect these alterations, showing the intricate interplay between installation effects and lateral loading response. Overall, the results emphasize the necessity of considering installation processes in predicting pile behaviour accurately.

While this study provides valuable insights into the behaviour of piles in dry sand conditions, it also underscores several limitations that necessitate further research. Future investigations should address these limitations to provide more robust insights into the behaviour of offshore wind monopiles and inform more effective design and installation practices in the renewable energy sector.

Acknowledgements

I would like to convey my sincere appreciation to the persons whose support and guidance have been invaluable throughout the process of completing this MSc. Thesis. The fulfilment of this work would not have been possible without them.

First and foremost, I want to express my deepest gratitude to my thesis committee for their immense support, expert guidance, and invaluable insights during this journey. Their commitment to my academic development and the numerous hours dedicated to reviewing and advising on my work have been very beneficial. I am profoundly thankful to Vagelis Kementzetzidis for generously offering me the possibility to developing this project by his side, for the chance to explore new horizons within the Geotechnical Engineering world, and for his continuous mentorship and encouragement. His guidance, feedback, and patience in addressing my numerous questions have played a pivotal role. I also want to extend my appreciation to the other members of my committee: Ronald Bringreve, for consistently being available, providing prompt feedback, pushing me to progress from the early stages of my research, and helping me improve my time management skills; and Athanasios Tsetas, for his invaluable contributions, kindness, and for always being genuinely keen on sharing his extensive knowledge with me, his contagious enthusiasm and passion for what he does were really inspiring.

I would also like to express my gratitude to my family who have been a source of support and motivation during these challenging times. I am eternally thankful for their sacrifices that have enabled me to pursue this master’s degree, for their faith in me, and their patience during this moment of my life. They have truly been my pillars of strength, and their words of encouragement were fundamental to finish this project. Lastly, I want to thank my friends, both old and new, whether near or far away from me, for being part of this journey and for offering me invaluable moral support and occasional distractions precisely when I needed them the most.

This work would not have been possible without the guidance, support, and motivation of these persons. Thank you for being part of this significant milestone in my academic journey.

Contents

List of Figures

List of Tables

1 | Introduction

1.1 Background and motivation

In recent years, there has been a growing recognition of the pressing necessity to tackle climate change and reduce greenhouse gas emissions. This recognition has grown due to mounting scientific evidence revealing the profound impact of climate change on our planet. To address this issue effectively, experts propose transitioning to sustainable energy sources. The reason for this is that traditional fossil fuels like coal, oil, and gas, which have served as the main energy sources for many years, are also major culprits behind greenhouse gas emissions. Therefore, shifting towards sustainable energy sources is now gaining increasing importance as a crucial step in combating climate change.

As our planet strives towards a more sustainable future to combat the harmful impacts of climate change and foster a healthier environment for future generations, research indicates that offshore wind power is one of the most promising and rapidly expanding sources of renewable energy. In fact, by 2020 it had become one of Europe's largest form of electricity generation capacity, exhibiting the most rapid development rate among all energy sources. It had, up to that year, a total installed offshore wind capacity of 25 GW, equivalent to 5,402 grid-connected wind turbines across 12 countries (Ramírez et al., 2021). Currently, there is over 30 GW of installed capacity (5,954 functioning turbines), up to date ("European Offshore Wind Farms Map Public", 2023), and some analysts project the sector to expand sixfold globally by 2030 (BNEF, 2018). By harnessing the power of the wind, offshore wind turbines are capable of generating electricity counting with higher wind speeds and fewer visual and noise impacts than their onshore counterparts, making them an attractive solution for sustainable energy production (Sánchez et al., 2019).

The ocean is a formidable and ever-changing environment, and constructing wind farms offshore requires careful consideration of many factors, including the type of foundation used on the offshore wind turbines (OWTs) and their installation. Such foundation is subjected to a combination of loading (axial and lateral loading, and bending and torsional moments, all generated by environmental conditions) and it is responsible for supporting the weight of the wind turbine (O'Kelly & Arshad, 2016). Moreover, it must be designed to resist and absorb the load cycles of varying direction exerted by the sea and by the wind. The most commonly used type for OWTs are monopiles (Sunday & Brennan, 2021), especially in Europe, where more than 80% are founded using this type of piled foundation ("European Offshore Wind Farms Map Public", 2023; Ramírez et al., 2020, 2021).

The installation of offshore monopiles is most commonly performed by means of impact hammering (Merchant, 2019), i.e. by driving the pile into the seabed using a percussive piling hammer to repeatedly strike its head (typically several thousand times, until reaching the required depth) with an energy of up to several thousand kilo-joules. As the impact induces a force at the top of the foundation, this causes a compressional wave propagating along the pile in axial direction, reaching the tip and pushing the pile into the ground. Despite being a highly sturdy, robust, and effective installation technique (Tsetas et al., 2023), its primary drawback is the significant noise levels produced during the process of driving the piles into the seabed. As the compression wave travels along the pile and reaches the tip, it causes the monopile to undergo radial expansion due to the Poisson's ratio effect (Achenbach, 1973), resulting in the generation of high-amplitude pulses of underwater noise (van Rhijn, 2017).

The aforementioned underwater noise produced by the installation process of monopiles offshore is linked, by scientific evidence, to various detrimental effects on marine mammals, sea turtles, fish, and invertebrates, that range from site avoidance to permanent auditory damage (Merchant, 2019; Tsetas et al., 2023). As a result, many governmental agencies and regulators are enforcing restrictions for the noise level produced during pile driving and underwater noise pollution and its mitigation measures have become a prominent concern on the policy agenda. For this reason, there is an increasing interest in researching the applicability of other techniques and a growing spotlight is being cast on the use of vibratory driving. This method has been shown to minimize the underwater noise levels and, hence, to reduce the potential for harm to marine mammals and other marine life, since it leads to lower piling loads compared to impact hammering. Some research are now focusing on this, such as the GDP project in The Netherlands, by developing the 'Gentle Driving of Piles' technique based on the simultaneous application of low-frequency/axial and high-frequency/torsional vibrations to drive the pile in a "gentler" manner (Metrikine et al., 2020).

Furthermore, research has shown that the installation of piles affects the state, structure, and properties of the surrounding soil. Additionally, it has been observed that different installation techniques can yield varying effects and may have distinct impacts on the pile's behaviour when the wind turbine is operational and exposed to subsequent cyclic lateral loads from the offshore environment. These differences could potentially hinder the turbine's long-term performance. Unfortunately, when it comes to vibratory driven piles, the suitability of current foundation design practices for lateral loading remains uncertain, as these methods have been traditionally studied, developed, and designed based on experience with impact-driven piles (Staubach et al., 2022). As this novel installation technique is characterized by low noise levels, short installation times and low costs (Tsetas et al., 2023) it is worth addressing unresolved questions related to such vibratory post-installation effects to hasten the transition from impact hammering to a gentler installation technique. Since the effects of this installation method on the bearing capacity and life-time performance of the monopile are still unknown to some extent, further research is vital for optimizing the process and ensuring the long-term performance and stability of offshore wind turbines installed with vibro-driving.

1.2 Objectives and Research Questions

Building on the aforementioned motivation, this work presents a numerical investigation into how the vibratory installation technique affects the lateral response of tubular piles to subsequent cyclic lateral loading, considering a pile with an outer diameter of D = 0.76 m embedded 8 m into dry, dense sand. To achieve this, a soil-monopile 3D Finite Element model is developed using non-linear sand modelled with the Manzari-Dafalias constitutive model. This purpose is accomplished by combining two existing models: The output loads produced in the pile-soil interface from a model that simulates the vibratory installation process (Tsetas et al., 2023) are used as an input in a 3D finite-element model that reproduces the non-linear cyclic soil behaviour on a long-term, when the pile is subjected to lateral loads (Kementzetzidis et al., 2019). The latter accounts for the interaction between the foundation and the surrounding soil. Hence, the main objective of this study is to address the following research question:

"What is the effect of vibratory pile driving on the long-term performance of monopiles installed offshore and subjected to environmental cyclic loads?"

To achieve such purpose of addressing some uncertainties associated with the OWT's response during storms accounting for installation effects, the study centers on the following research sub-questions:

- What are the changes in soil properties and structure during vibratory driving and in the long-term?
- How the initial soil conditions influence and impact the extent of these changes?

This M.Sc. thesis adopts a well-defined and structured approach. The forthcoming chapters (Chapters 2 and 3) delve into and elaborate on the methodology employed to fulfill the study's objectives, including details about the model generation, parameters, and variables. Theoretical aspects and concepts are also included in both chapters to enhance the overall understanding of the project. Chapter 4 presents the obtained results, providing valuable insights into the performance of monopiles after installation, under subsequent lateral loading. Lastly, Chapter 5 concludes the thesis by offering a brief overview of the work and discussing its significant findings.

2 | Methodology

As previously mentioned, the objective of this research project is to comprehend the impact of vibratory pile driving on monopile stability and the surrounding soil on a long term. This chapter primarily centers on providing a concise explanation of the adopted approach to attain this objective and address the research question.

Conducting this study involves the integration of two separate models: the first model accommodates vibratory installation effects and is formulated by Tsetas et al. (2023) as a component of a doctoral program; while the second model assesses soil behaviour under lateral cyclic loading conditions and is formulated by Kementzetzidis et al. (2019) during his pursuit of a M.Sc. in Geotechnical Engineering, both at the Technical University of Delft in The Netherlands. The subsequent sections first provide an overview and theoretical description of the vibratory installation concept, together with its effects, and of the lateral loading process. Afterwards, descriptions of both models, followed by an explanation of the procedure used to combine them is presented. Some key aspects of the Finite Element Method are also discussed, and finally, the tested scenarios in terms of applied loading are outlined.

It is important to note that in this research, the soil modelled is considered dry, despite being intended for offshore wind applications (where soils are typically water-saturated). This choice and simplification are primarily due to the fact that numerical analyses involving multi-phase processes are significantly more complex, computationally intensive, and time-consuming compared to single-phase analyses. The limitations and advantages of this simplification are discussed in detail in Section 3.2.2 of this report.

2.1 Vibratory Installation of Monopiles

The monopile, one of the most widely utilized offshore foundations (Figure 2.1) due to its ease of installation, cost-effectiveness, and logistical advantages (O'Kelly & Arshad, 2016), comprises a single circular hollow pile. Typically deployed in shallow water depths ranging from 20 to 40 meters, this foundation type is primarily installed into the seabed through large impact hammers or vibratory pile driving, i.e. vibro-piling. As discussed in the preceding chapter, while the former method is the most widely and commonly employed, it does possess certain limitations that can be addressed through the employment of the latter approach.

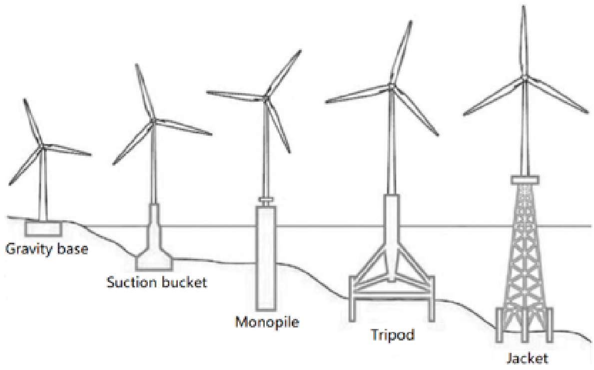

Figure 2.1: Different types of offshore foundations. (*Retrieved from Xie and Lopez-Querol (2021)*).

While impact driving, as described before, involves using a large hammer to strike the top of the pile and drive it into the seabed, vibratory driving utilizes the harmonic rotation of eccentric masses, powered by hydraulic motors, to generate a rapidly alternating sinusoidal vertical force applied to the pile. The rotation of these weights is such that it counteracts horizontal vibrations, allowing only vertical vibrations to be transmitted into the pile. This results in a periodic force acting in a single plane and directed toward the center-line of the shaft (Nedwell et al., 2003), which must overcome the static and dynamic resistance along the pile shaft and at the tip to penetrate the pile into the ground (Feng & Deschamps, 2000). In simpler words, when using vibratory pile driving, the consistent upward and downward movement of the pile diminishes the soil's shear resistance. This leads to a condition where the soil loses its particle structure and transforms into a kind of localized liquefied state.

This installation technique offers several advantages compared to impact driving, such as faster driving of the pile, quieter operations, and easier transportation of the needed equipment. By employing this method, it becomes possible to drive even extremely large piles and it significantly reduces the amplitude of underwater noise compared to piles driven by impact. In addition, vibro-piling generates continuous sound, unlike the more disturbing intermittent sound produced by impact driving, and, overall, it produces significantly lower piling loads (Feng & Deschamps, 2000).

Nevertheless, impact driving remains preferred for several reasons. Its extensive historical use has led to the development of reliable estimation and design methods, such as wave equation analyses, which can accurately predict driving resistance and aid in equipment selection (Massarsch et al., 2021). Additionally, stress wave measurements can be employed after driving to estimate the bearing capacity of the pile. In contrast, when it comes to vibratory driving, reliable scientific tools for equipment selection are lacking, and there is a significant level of uncertainty when assessing the bearing capacity of piles following vibratory installation (Bosscher et al., 1998).

2.1.1 Installation Effects

The pile installation process leads to significant changes in the primary state parameters of the surrounding sandy soil, causing notable stress and deformation regardless of the installation method. This introduces a critical source of uncertainty in the analysis and design of pile foundations, as the operation involved alters the soil's characteristics and stress-strain states, impacting pile settlement and bearing capacity.

In a broad sense, while driving the pile, the sandy soil is displaced both vertically and radially to facilitate the penetration of the pile, compressing the soil around it (Kabeta, 2022). As a result, the final stress distribution is quite different from the in-situ stress in the free field, as observed in the sketch from Figure 2.2, retrieved from al-Omari et al. (2017). The aforementioned compression may cause the soil to compact and become denser (depending on the initial relative density of the soil), which may lead to increased soil strength and friction along the sides of the pile.

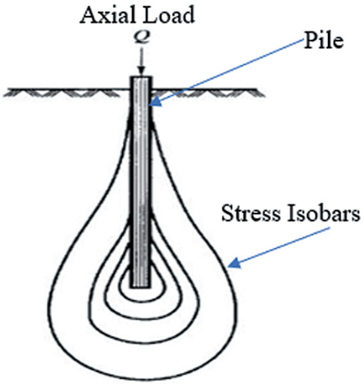

Figure 2.2: Stress distribution after the installation of a pile. (*Retrieved from al-Omari et al. (2017)*).

As a simplified process, in terms of vibratory installation, while the profile experiences vibratory vertical movement it transmits shear stresses and shear strains to the adjacent soil laterally. Simultaneously, it induces normal soil movement beneath the pile tip (Holeyman, 2002). Certain writers assert that the base resistance of the pile increments as the number of cycles applied increases, owing to the compaction of sandy soil near the pile toe. Conversely, the radial stress acting on the shaft decreases with the number of cycles due to the densification of the sandy soil adjacent to the pile shaft (Kabeta, 2022). Moreover, as the distance between the pile tip and the ground surface increases, there is a tendency for friction fatigue phenomenon to occur, resulting in a further reduction in radial stress. This is more pronounced for this pile driving technique due to the induced cyclic shearing (Staubach et al., 2022).

The effects of vibratory pile driving on dry sandy soils are further evaluated, analyzed, and reported in subsequent chapters of this report.

2.1.2 Vibratory Installation Model

The process for simulating the vibratory pile installation used in this research, as outlined by Tsetas et al. (2023), involves a non-linear dynamic pile–soil interaction model where the pile is represented by a thin cylindrical shell via a semi-analytical finite element approach. It depicts the soil medium as a layered half-space using the Thin-Layer Method (TLM) coupled with Perfectly Matched Layers (PMLs) to characterize the underlying half-space. Furthermore, the entire three-dimensional model exhibits axisymmetry, given the symmetry of all the elements in the model with respect to the vertical axis. The non-linearity in the model is represented and concentrated at the pile-soil interface region, while the rest of the soil body exhibits linear elasticity. A schematic of such model is shown in Figure 2.3, where the application of a dynamic ring load is observed. The model allows for this input excitation to either be directly applied at the pile head or at a certain component, taking into account the overall interaction (Tsetas et al., 2023).

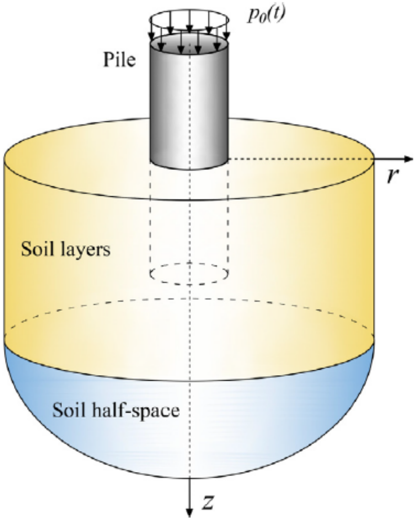

Figure 2.3: Model used to simulate the vibratory pile installation process: A pipe pile partially embedded in a layered soil medium. (*Retrieved from Tsetas et al. (2023)*).

The authors characterize this approach as a "computationally efficient yet accurate scheme" due to the comprehensive integration of its elements. Such integration allows it to effectively capture the vibratory installation process' physical aspects while simultaneously maintaining computational efficiency and practical relevance in engineering applications. Moreover, its accuracy is supported by a thorough comparison of the model predictions with pile installation data from field tests and the description of the pile–soil interaction by a history-dependent frictional interface characterized by real S-CPT measurements (Tsetas et al., 2023).

2.2 Lateral Loading

In structural analyses, lateral loading refers to the application of horizontal forces on a structure. In the context of an offshore wind turbine monopile, these lateral forces primarily originate from environmental factors such as wind and waves.

When designing and evaluating offshore structures, addressing lateral loading is crucial. Estimating the potential lateral forces is essential to ensure the structure can endure these loads and maintain stability. Various factors, including wind speed and wave conditions, influence lateral loading. Nowadays, advanced modelling and analysis techniques are employed to simulate environmental conditions, assessing their impact on the monopile's stability and structural integrity.

The cyclic pressures exerted by these forces on the monopile, displaying variations in both direction and amplitude, lead to changes in the stiffness of the surrounding soil over time. Additionally, the piles, being stiff in bending, may undergo rigid body rotation when subjected to such loads. Consequently, substantial movements occur at the pile base, potentially mobilizing significant resisting base shear force and moments (Wang et al., 2023). This alters the interaction between the foundation and the soil, posing challenges for the OWT, and such cumulative effect of irreversible deformation is attributed to potential failure.

2.2.1 Lateral Loading Model

This model, developed by Kementzetzidis et al. (2019), involves the analysis and understanding of offshore wind turbine dynamic interactions with a sandy seabed, using three-dimensional finite element modelling techniques. It specifically focuses on establishing a connection between how the wind turbine structure responds to the external lateral forces it experiences (like wind and waves), and how the seabed's non-linear behaviour affects such response. By employing this approach, the research surpasses the limitations of traditional non-3D analysis methods, enabling a more intricate comprehension of complex interactions between wind turbines, monopile foundations, and sandy soils under dynamic conditions.

This model is the basis of the current research and is further developed and described in subsequent sections of this report. The first model, previously described in Section 2.1.2, is not described upon further, as its output is the primary focus. Delving into the specific intricacies of the vibratory installation itself is beyond the scope of this thesis.

2.3 Finite Element Methodology

The present study employs the Finite Element Method (FEM) for soil dynamics analyses, a powerful and versatile numerical technique for analyzing and simulating complex physical soil phenomena. This method yields outcomes including displacements, stress and strain distribution, time history, etc., needed for understanding the soil behaviour when subjected to external loading.

The focus of soil dynamics lies in understanding the behaviour and response of soil under specific loads. It involves and deals with analyzing and predicting how soils react to these loads, along with examining how soil-structure systems respond to them, employing the FEM in this case.

It is important to highlight that the key distinction between static and dynamic analyses lies in the nature of the load. Dynamic analyses deal with rapidly changing loads, which introduce inertial effects, making it a time-dependent process. For instance, when a vibratory load is applied to a soil medium, it causes acceleration, generating inertial forces that are accounted for in this type of analyses. This approach helps to understand the real-time response of the soil to dynamic loads, even at different frequencies. In contrast, static analyses assume that loads are applied slowly enough to prevent the generation of these accelerations, thus failing to capture the time-dependent effects.

Since this research aims to model soil behaviour under cyclic loading, a dynamic analysis is performed. A static analysis would fail to capture the accumulation of strain from repeated loading cycles, the effects of repeated loading and unloading, and the evolution of stiffness and strength properties, which are typically revealed through dynamic analyses.

The subsequent sub-sections explore and delve into the fundamental principles and applications of FE analysis, crucial for assessing soil behaviour under dynamic loading. Additionally, some of its critical aspects are discussed, underlying the mathematical foundations that govern it.

Key factors such as mesh generation, time-step, boundary conditions, and other considerations essential for FE analysis are highlighted in later chapters.

2.3.1 Governing Equations and Numerical Solution

In the context of soil dynamics problems, the choice of solutions may vary based on whether it is approached as a one-phase problem or a multi-phase problem. The former solution can be applied to address the problem in scenarios where the soil is dry, without any fluid in its pores, when it is water-saturated but exhibits high permeability, or when the load is applied gradually enough to prevent pressure build-up. Conversely, the latter solution is employed in nearly all other cases when the soil is water-saturated. The present research, which focuses on analyzing dry sand, is treated as a one-phase problem, and the following section outlines and focuses on its governing equations. The dry soil simplification is further expanded in Section 3.2.2.

Following the work by Hughes (1987), the so-called strong and weak formulations of the momentum balance are here adopted as a base to describe the dynamic mechanical response of the soil. Though a three-dimensional problem is solved on this research, the foundation of the strong formulation lies in considering a simple case of a one-dimensional embedded bar with a length L, subjected to a dynamic tension loading σ(t) at x=L. The time-dependent boundary conditions of the problem consist of both Dirichlet conditions, specifying a fixed displacement at the embedment point (u(0) = 0), and Neumann conditions at the end of the bar (σ(L) = σ(t)).

The analysis commences with the equation of dynamic equilibrium, which is represented by the one-dimensional wave propagation equation, together with the equation of strain compatibility and the constitutive relation for elastic behaviour (Equations 2.3.1). The strong formulation represents the equilibrium equation for such beam under dynamic conditions (Equation 2.3.2) and it is obtained by combining these three equations to reach a solution for the displacement. Such solution corresponds to a function that is twice differentiable (in both the whole domain of space and time) (Pisanò, 2022).

$$\frac{\partial \sigma}{\partial x} = \rho \frac{\partial^2 u}{\partial t^2} \qquad \varepsilon = \frac{\partial u}{\partial x} \qquad \sigma = E\varepsilon \tag{2.3.1}$$

$$\frac{\partial}{\partial x}\left(E\frac{\partial u}{\partial x}\right) = \rho \frac{\partial^2 u}{\partial t^2} \tag{2.3.2}$$

An arbitrary differentiable *test* function that fulfils the boundary conditions of the original problem is multiplied on both sides of the strong formulation equation. Owing to this, the weak formulation is reached (Equation 2.3.3) as a *dynamic virtual work principle* by integrating by parts. The final solution for the displacement, only once differentiable, expresses the work carried out by the external forces applied at the boundary of the bar as a summation of the internal forces (stresses) and the inertial forces within the bar (acceleration).

$$\sigma(t).\delta u(L) = \int_0^L \sigma.\delta\varepsilon \, dx + \int_0^L \rho \frac{\partial^2 u}{\partial t^2}.\delta u \, dx \tag{2.3.3}$$

The preceding method can be extended to three-dimensional one-phase boundary value problems, employing both the strong (or differential) formulation and the weak (or integral) formulation. Following a similar approach as described earlier, the strong formulation is obtained by combining the inertial forces from the dynamic equilibrium equation with the compatibility equation and the constitutive relationship for linear elasticity, as illustrated in Equation 2.3.4 using tensor notation (Pisanò, 2022). It is worth noting that the Dirichlet and Neumann conditions are also generalized to three dimensions.

$$\rho \ddot{u}_i = \sigma_{ij,j} + b_i \qquad \varepsilon_{ij} = \frac{1}{2}(u_{i,j} + u_{j,i}) \qquad \sigma_{ij} = D_{ijhk}\varepsilon_{hk} \tag{2.3.4}$$

The initial equation encompasses dynamic equilibrium, which accounts for inertial forces, represented as the divergence of the stress tensor, along with body forces like gravity or other forces acting upon the body. The subsequent equation, the compatibility equation, expresses strain as a function of the displacement vector. Finally, the third equation establishes the constitutive relationship for linear elasticity, describing the correlation between stress and strain tensors. All three equations, combined to formulate the strong solution, are considered within the domain and during the analyzed time interval.

Additionally, the weak formulation, expressed in Equation 2.3.5 in tensor notation, is derived from the strong formulation following the same path as described earlier: by multiplying, on both sides of the strong formulation equation, a *test* function and integrating over the whole spatial domain. Such function, in this case $\omega_i = \delta u_i$, must be differentiable and must belong to the same functional space of the displacement u_i (Pisanò, 2022). This procedure provides an equation in which inertial and internal forces (first and second integrals in Equation 2.3.5, respectively) must be balanced by external forces (body forces, surface tractions, loads applied on the surface or within the domain, etc).

$$\int_{\Omega} \delta u_i \rho \ddot{u}_i \, d\Omega + \int_{\Omega} \delta u_{(i,j)} \sigma_{ij} \, d\Omega = \int_{\Omega} \delta u_i b_i \, d\Omega + \int_{\Gamma_\sigma} \delta u_i t_i \, d\Gamma_\sigma \tag{2.3.5}$$

The weak formulation is a powerful tool for dealing with certain types of partial differential equations in a more flexible and mathematically manageable way. It achieves this by integrating the differential equation by parts and eliminating higher-order derivatives. This "weakening" of the requirement allows for considering more general functions, as it removes the need for the displacement to be twice-differentiable. Additionally, in some cases, strong solutions may not exist or might be difficult to find, making weak solutions a more versatile framework for addressing such situations (Hughes, 1987). In this research, such weak form of the momentum balance is solved.

2.3.2 Space Discretization and Finite Element Formulation

The weak formulation can be discretized in space using the Standard Galerkin finite element method. To achieve this, the unknown function and the test function are approximated by employing finite element spaces, resulting in a system of algebraic equations that can be estimated numerically to obtain the solution (Hughes, 1987).

The Galerkin finite element formulation poses a spatial domain, Ω, divided into a collection of non-overlapping elements, Ω_e. Every element has nodes in which the unknown function, displacement u(x) in this case, is approximated using a polynomial approach, involving a linear combination of basis functions (Equation 2.3.6). These elements are often simple shapes like triangles, quadrilaterals, or tetrahedra in three dimensions, and this spatial discretization simplifies the problem by transforming it into a set of interconnected sub-problems.

$$u(x,t) \approx N(x) \cdot U(t) \qquad\qquad \varepsilon \approx B(x) \cdot U(t) \tag{2.3.6}$$

It is observed from Equation 2.3.6 that the solution in each element is only a function of the vector nodal variables that depends on time, *U(t)*, and a shape function matrix, *N*, that provides a depiction of how the solution is distributed in space. Similarly, for the strain calculation in each element, a compatibility function matrix, *B(x)*, is introduced. These solutions for displacement and strain can be substituted in the weak formulation (Equation 2.3.5) to discretize the problem in space by considering each element separately. Afterwards, the global behaviour of the entire system is determined: the equations established for each element are combined to form a global system of equations by assembling the contributions from each one of them into a larger matrix system.

The resulting ordinary differential equation system after the space-discretization for a linear viscoelastic medium is depicted in the following equation, known as the equation of motion.

$$M\ddot{U}(t) + C\dot{U}(t) + KU(t) = F_{ext}(t) \tag{2.3.7}$$

The first term corresponds to the element's inertia, while the second and third correspond to the soil internal forces. From which:

$$M = \sum_{1}^{N_e} \int_{\Omega_e} N^T \rho N \, d\Omega \tag{2.3.8}$$

$$C = \sum_{1}^{N_e} \int_{\Omega_e} B^T V B \, d\Omega \tag{2.3.9}$$

$$K = \sum_{1}^{N_e} \int_{\Omega_e} B^T D B \, d\Omega \tag{2.3.10}$$

$$F_{ext} = \sum_{1}^{N_e} \int_{\Omega_e} N^T b \, d\Omega + \sum_{1}^{N_e} \int_{\Gamma_{\sigma e}} N^T t \, d\Gamma_{\sigma e} \tag{2.3.11}$$

Where the elastic stiffness matrix, *K*, and the viscous physical material damping matrix, *C*, are assembled once prior to time integration (Pisanò, 2022). Additionally, the internal force term is observed to be implicitly linked to the global (tangent) stiffness matrix and to the viscous damping, which may arise either from the constitutive level (viscous soil behaviour) or be introduced through numerical Rayleigh damping (Zienkiewicz et al., 1999). For this research, the latter approach is employed to account for material and numerical dissipation, utilizing damping parameters *a* and *b*, and expressing proportionality to the mass and stiffness matrices in the form of $C_{Rayleigh} = aM + bK$. This is further explored in Section 3.1.

Solving the system of equations together with the boundary conditions of the problem, yields the unknowns, in this case displacements, across the entire domain. This is often done numerically using iterative methods.

2.3.3 Time Integration Schemes

In dynamic finite element analyses, the goal is to obtain a time domain solution for the equation of motion originating from the weak formulation (Equation 2.3.7) to understand its progression in time. To achieve this, step-by-step integration methods are used to obtain such solution at discrete time intervals. The crucial aspects of these integration schemes are that they need to be unconditionally stable for linear problems and that they must hold second-order accuracy and possess algorithmic damping, simultaneously (Hughes & Hilber, 1978).

Nonetheless, according to Strang and Fix (1973), modes corresponding to medium-to-high frequencies tend to become increasingly inaccurate in some methods, due to poor spatial discretization and an absence of algorithmic damping. For example the Newmark method, which is the most widely utilized integration scheme in geotechnics due to its unconditional stability, results in excessive numerical oscillations when higher frequencies are used as input. Besides, even though if numerical dissipation is introduced into the Newmark scheme the oscillations are damped, the method loses its second-order accuracy (Kontoe et al., 2008).

As vibro-installation of monopiles is one of the main focus of this research, and it induces high frequencies into the soil, the time integration scheme proposed by Hilber et al. (1977), also known as the Hilber-Hughes-Taylor Method, is chosen. The primary rationale behind this selection is that the method possesses a combination of unconditional stability and numerical damping capability for high-frequency modes in conjunction with second-order accuracy. When compared with other methods (Wilson-θ method, for example), it is preferred and widely implemented in geotechnical finite element codes and within the structural dynamics community (Kontoe et al., 2008).

The Hilber-Hughes-Taylor Method, hereafter referred to as the HHT method, is a single-step integration algorithm derived from the Newmark (1959) method. In the latter, a family of integration formulas that depend on the parameters γ and β is defined to discretize the displacement and velocity at time t_{k+1} (Equations 2.3.12 and 2.3.13, respectively). Δt represents the integration step size, while t_k and t_{k+1} denote two consecutive time intervals (t_{k+1} = t_k+Δt). However, the HHT method introduces a third parameter, α, into the equation of motion, resulting in Equation 2.3.14 (Negrut et al., 2007).

$$u(t_{k+1}) = u(t_k) + \dot{u}(t_k)\Delta t + (\frac{1}{2} - \beta)\ddot{u}(t_k)\Delta t^2 + \beta\ddot{u}(t_{k+1})\Delta t^2 \tag{2.3.12}$$

$$\dot{u}(t_{k+1}) = \dot{u}(t_k) + (1 - \gamma)\ddot{u}(t_k)\Delta t + \gamma\ddot{u}(t_{k+1})\Delta t \tag{2.3.13}$$

$$M\ddot{u}(t_{k+1}) + (1-\alpha)C\dot{u}(t_{k+1}) + \alpha C\dot{u}(t_k) + (1-\alpha)Ku(t_{k+1}) + \alpha Ku(t_k) = (1-\alpha)F_{ext}(t_{k+1}) + \alpha F_{ext}(t_k) \tag{2.3.14}$$

To ensure the promised stability and accuracy properties of the HHT method, it is essential to select a value for α within the range of -0.33 to 0 (Hilber et al., 1977). A smaller value results in increased damping in the numerical solution, whereas setting α=0 leads to a solution without numerical damping (Negrut et al., 2007). Furthermore, γ and β should be set to $\gamma = 0.5 - \alpha$ and $\beta = (1-\alpha)^2/4$.

2.3.4 Solution Algorithms

Following the process described earlier, it becomes necessary to employ an iterative solution scheme for each step increment as, for non-linear problems, the relationship between the stresses and strains is unknown. The most commonly utilized methodology to achieve the solution of the equation of motion is the Newton iteration method, also known as the Newton-Raphson method, due to its capabilities and efficiency compared to other methods (Akram & ul Ann, 2015). This method is an optimization algorithm aimed at iteratively refining better approximations to locate the roots or zeros of a real-valued function in a sequential manner.

In a very concise and simple manner for only one variable, the Newton-Raphson method begins with an initial guess, close to the true root of a function. It then approximates the function and its slope by a straight line, determined using calculus, and calculates the x-coordinate where this line intersects the x-axis, providing a more accurate estimate of the root than the initial guess. Further, this process is repeated iteratively to converge towards the actual root of the non-linear function (Akram & ul Ann, 2015). Additionally, this algorithm might also be expanded and used for a system of equations with *k* variables using the Jacobian matrix instead of the slope used in the simple case. This Jacobian represents the partial derivatives of each equation with respect to each variable, i.e. it describes how each equation changes with small changes in the variables.

In this research, the Modified Newton algorithm is employed due to its efficiency in comparison with the original Newton: in the iterations, the tangent at the initial guess is used instead of the current tangent, meaning that the Jacobian system is formed only once at the beginning of each step.

All the theoretical information previously presented and described corresponds to the different parameters and conditions set up in the finite element model to run the analyses. Although this whole process is automatically performed by the OpenSees software, it is important to know the theory behind it to be able to select the proper and most accurate modelling conditions.

The comprehensive theoretical information discussed earlier serves as the foundation for defining the various parameters and conditions essential for the finite element model used in the analyses. While the OpenSees software automates this entire process, understanding the underlying theory is crucial for selecting the most appropriate and precise modelling conditions, making informed decisions and ensuring the accuracy and reliability of the simulation results.

2.4 Approach

In order to successfully achieve the comprehensive objectives outlined within this project, the used strategic approach involves the integration of the two previously described models. The initial phase of such integration centers around the utilization of the Tsetas et al. (2023) model, which generates data related to the loads produced within the interface between the monopile and the soil during the process of vibratory pile installation. These generated loads, obtained as the output of the aforementioned model, are utilized as the input for the Kementzetzidis et al. (2019) model: they are applied on the three-dimensional non-linear domain, altering the state of the foundation soil, which, in turn, affects the monopile's behaviour after installation; and the monopile is, then, subjected to environmental loads (wind, waves) to simulate the lateral loading. By merging these two models, the lateral behaviour of the monopile and the non-linear vicinity soil is observed and the effects of the installation process are accounted for.

This exchange of information creates an important link between the two models, helping them work together to gradually build a complete understanding of how the vibratory installation process affects the surrounding soil and the overall stability of the offshore wind turbine on a long term. By combining these models, the process of installing vibratory monopiles and some of the complexities involved regarding the performance of the offshore foundation are tackled.

The following list outlines the procedure for integrating both models and, consequently, accomplishing the objectives of this study.

- Once the soil and monopile properties, boundary conditions, model parameters (including algorithm, solver, integrator, and analysis type), time-step size, and mesh geometry (further elaborated in the upcoming section) are defined, the entire process starts with a gravitational analysis, often referred to as the soil self-weight stage. At this stage, the numerical model of the soil, devoid of any structural components, is subjected to its own weight to understand the initial stress state and how it affects the constitutive behaviour of the soil in subsequent loading stages. To achieve this, specific displacement conditions are set, ensuring that nodes sharing the same Z-coordinate are tied in their vertical displacement. This constraint aims to attain a uniform settlement across the entire mesh. In this instance, this stage is executed in 20 gradual increments, which proves adequate for obtaining the initial state of stress and strain. This step serves to establish the initial geostatic stress distribution in the soil.
- After the gravity stage, the loads generated in the pile-soil interface during the vibro-installation process, obtained as an output from the installation model previously described, are simulated. In order to produce such loads, Tsetas et al. (2023)'s model uses as input: the shear modulus profile of the soil, estimated using a constitutive equation (Equation 3.2.4) proposed by Manzari and Dafalias (1997) and explained in subsequent sections (Section 3.2); the cone resistance profile with depth, calculated via empirical expressions and correlation factors posed by Jamiolkowski et al. (2003) (Equation 3.2.9); the geometry and properties of the monopile; the selected damping conditions; and the soil properties and parameters such as the elastic shear incremental modulus, the Poisson's ratio, mass density, initial void ratio and relative density. All these parameters are further elaborated and explained in Chapter 3.
- Following the completion of the simulation and modelling for vibratory installation, the forces generated on the shaft as a result of this procedure are extracted and incorporated into the second model. They are introduced as ring loads aligned with the relevant time-step and mesh discretization. These input excitations are allocated to all the nodes encompassing the monopile shaft, considering both their depth and the corresponding time-step of their occurrence.
- Once these loads are incorporated into the second model and the soil reaction to them is estimated, the elements that originally represented the soil are now replaced by pile elements. This includes assigning the defined material and properties of the pile to the previously replaced elements, while preserving the initial FE mesh. Additionally, a fictitious section of the pile is generated to be able to simulate and apply lateral loads, and its corresponding properties are defined. The latter corresponds to new elements connected via rigid links to the mudline monopile elements. In reality, this stage occurs concurrently with the preceding one, but this is the adopted approach adaptable for the numerical merge of the two models.
- Finally, the monopile undergoes lateral loading, and the cumulative impact of such forces, predominantly from wind and waves, are simplified and depicted by applying them in a designated section created specifically for this purpose, at the mudline. The excitation is applied solely along the positive X-direction, mimicking the environmental forces commonly experienced in offshore settings. Moreover, it is carefully selected so that it complies with the widely accepted methodology for the Ultimate Limit State (ULS) design limit, i.e. the load is high enough to produce a displacement of the pile head of at least 10% of the diameter of the monopile. It is also selected as high enough to cause non-linearity in the soil but slow enough not to cause any inertial effects. This is further explained in Subsection 2.6.

- The procedure was intended to be repeated for three vibration frequencies employed for the pile installation: 16 Hz, 23 Hz, and 30 Hz, to assess their influence on the long-term behaviour of the monopile and draw comparisons among them. However, due to computational limitations, only the scenario with a frequency of 30 Hz is examined in the remainder of this thesis. Additionally, a baseline scenario is incorporated in the analysis for comparison, focusing on lateral loading of the monopile without considering installation effects, i.e. considering the pile as wished-in-place (WIP).

2.5 Tested Scenarios

As previously mentioned, three loading case-scenarios of vibratory driving frequencies were going to be evaluated within the framework of the analysis program of this research, all obtained as an output of the vibratory installation model described in Section 2.1.2. Nonetheless, due to limited computational and time resources available, only one of them is presented (vibratory frequency of 30 Hz).

Similarly, modelling the entire pile driving process is challenging considering the high computational cost. For this reason, only the last four meters of vibratory installation are analyzed, i.e. from 4 m to 8 m depth, since they are considered to be more critical. This assumes that the first four meters of the pile are wished-in-place, reducing the driving time to 288.5 seconds of installation. The computational time to run the vibro-installation model of the entire 8 m pile and obtain the output loads generated in the soil was around 1 hour.

Additionally, a base case of the more widely used wished-in-place assumption (scenario without any applied installation load) is included in the numerical study for comparison. A summary of the examined scenarios is found below.

- Driving force with an amplitude of 522,102 kN and a vibratory driving frequency of 30 Hz. The active force is active for 337.31 seconds to achieve the installation of the 8 meters monopile. The loads that are generated with this vibration frequency at the pile-soil interface at the depths of 4.5 m, 6 m, and 7.5 m are depicted in Figures 2.4, 2.5, and 2.6, respectively. In these figures, the first horizontal line with null values corresponds to the top meters before reaching the evaluated depth of installation and, as expected, the 4.5 m depth plot (Figure 2.4) starts sensing the loads before the 6 m depth plot (Figure 2.5) and the 7.5 m plot (Figure 2.6). To the right of these graphs, a zoom-in of the initial load response at those depths is shown.
- Case without installation loads and featuring exclusively the applied lateral loads (Section 2.6); employed as a reference point for comparative analysis.

The chosen specification of 30 Hz is a typical value for vibratory drivers used in the industry and the amplitude displayed in the figures below is distributed uniformly amongst all the nodes situated within the pile shaft at the shown particular depth.

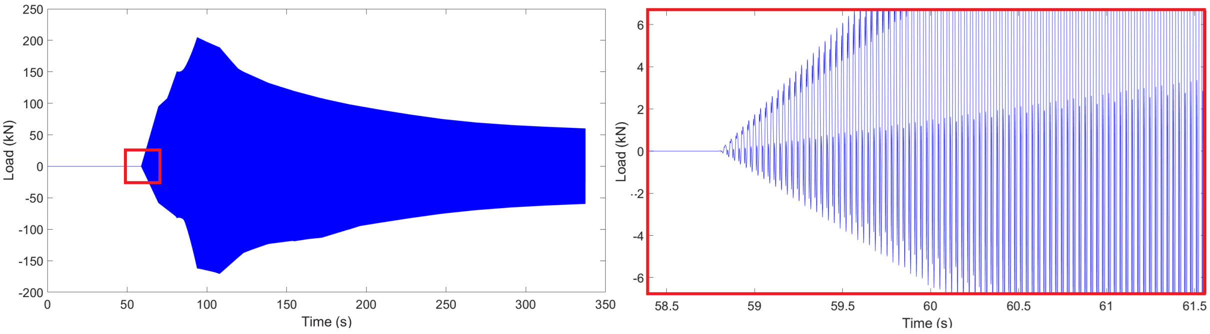

Figure 2.4: Installation loads produced with a driving frequency of 30 Hz at a depth of 4.5 m.

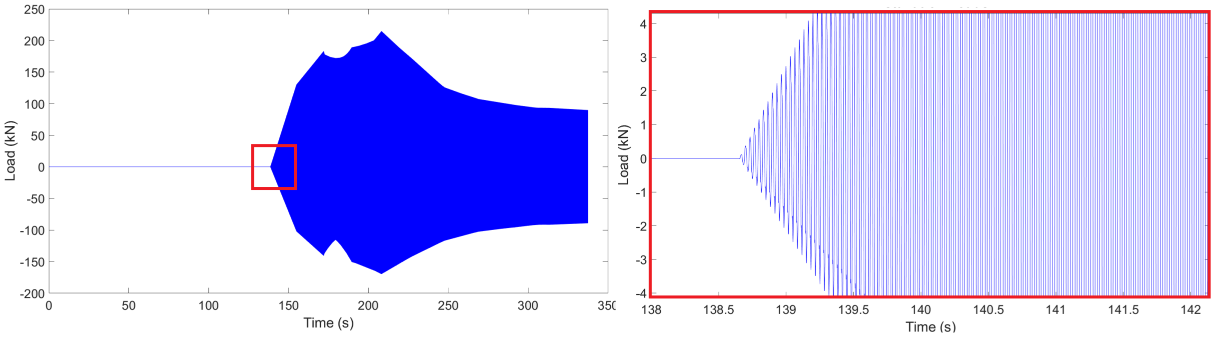

Figure 2.5: Installation loads produced with a driving frequency of 30 Hz at a depth of 6 m.

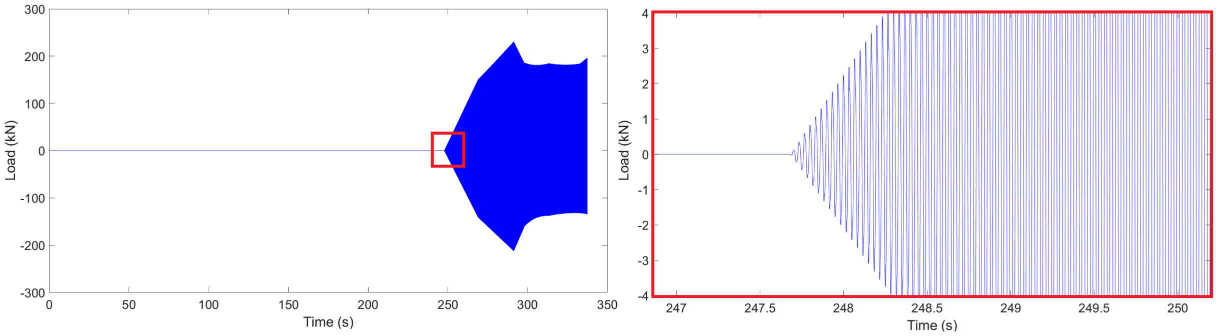

Figure 2.6: Installation loads produced with a driving frequency of 30 Hz at a depth of 7.5 m.

2.6 Applied Lateral Loads

After the installation process is completed and the installation loads, output coming from the model developed by Tsetas et al. (2023), have been incorporated into the current model as part of the dynamic analysis, the system experiences the influence of lateral forces, predominantly originating from wind and waves. To simplify the representation of their cumulative effects, these lateral loads are applied on the monopile at mudline elevation in the positive X-direction, following the guidelines in Sections 2.4 and 3.3.

The bearing capacity is defined as the load that leads to the ultimate state first, in either direction. Given the inherent challenges in accurately estimating the true ultimate capacity of a monopile, this research adopts the practical approach of employing the 10% diameter rule of thumb for pile bearing capacity, widely accepted as a ULS design. This empirical guideline stipulates that the maximum permissible displacement of a pile under external lateral loads should typically not exceed 10% of the pile's diameter. Consequently, the applied load that results in a 10% diameter displacement is regarded as the ultimate bearing capacity in this context.

For this reason, and as explained in previous sections, the applied excitation is selected so that it is high enough to produce a displacement of the pile head of at least 10% of the diameter of the monopile and to cause non-linearity in the soil, and slow enough not to cause any inertial effect. Initially, the soil undergoes testing purely under lateral loads, without any installation or additional external forces. This preliminary assessment aims to determine the theoretical bearing capacity, specifically identifying the load magnitude that results in a 0.1 times the diameter displacement. For this evaluation, the load pattern plotted in Figure 2.7 is applied, ensuring a high-enough load to reach the desired displacement on the first loading cycle.

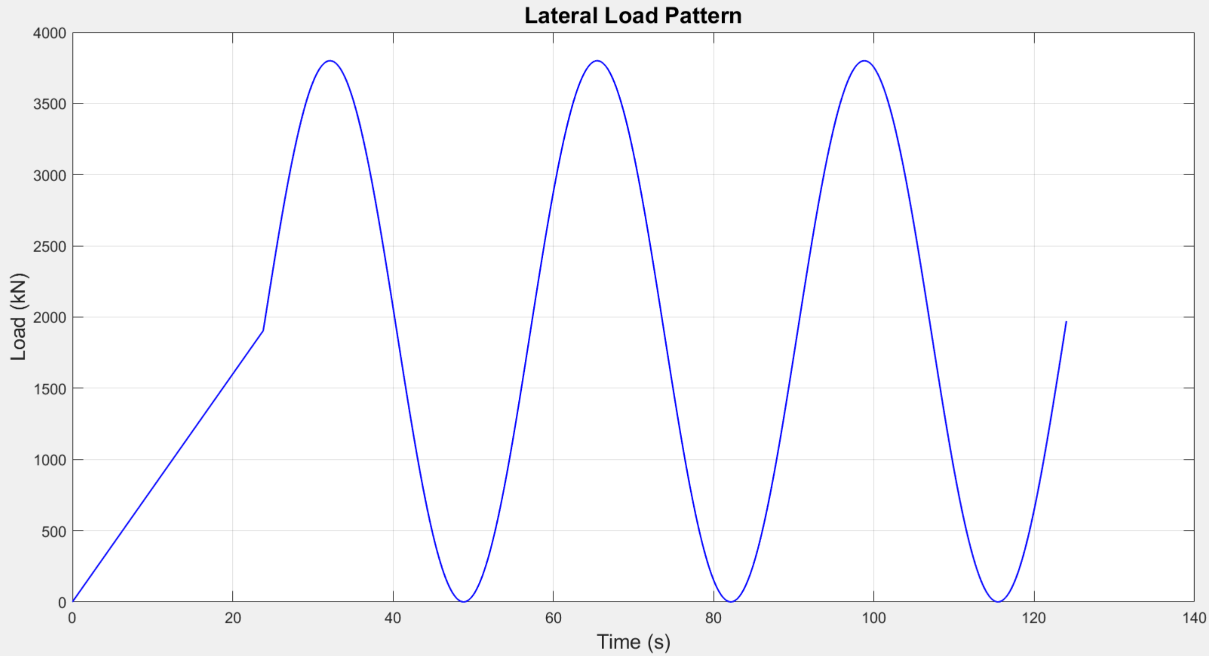

Figure 2.7: Load pattern of the initial stage lateral load.

The resulting load-displacement chart for the initial phase to determine the maximum load is depicted in Figure 2.8, showcasing the application of a maximum load of 3850 kN. Examining the figure, it becomes evident that the load responsible for generating a displacement of 10% of the diameter (0.076 m) during the first cycle is 2000 kN. This assessment is performed with the soil and pile characteristics described in previous sections of this report, but using a smaller mesh due to time constraints.

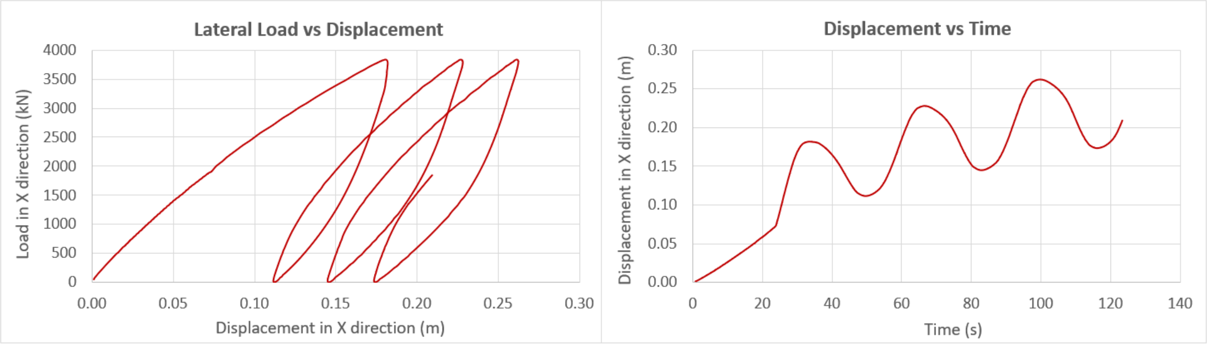

Figure 2.8: Load - displacement plot of the initial stage lateral load.

Consequently, following the first stage, the chosen lateral load for all the examined vibratory installation scenarios matches the 2000 kN particular maximum load value. Figure 2.9 showcases this load, comprising 10 cycles applied over a duration of 346 seconds at a frequency of 0.03 Hz and with an amplitude of 1000 kN. Its corresponding displacement response can be observed in Figure 2.10. The lateral loading stage is analyzed with a 0.2 seconds time-step and the same analysis settings selected for the installation phase. The chosen frequency is slightly lower than the typical frequencies found in an offshore environment, but it remains close to realistic values.

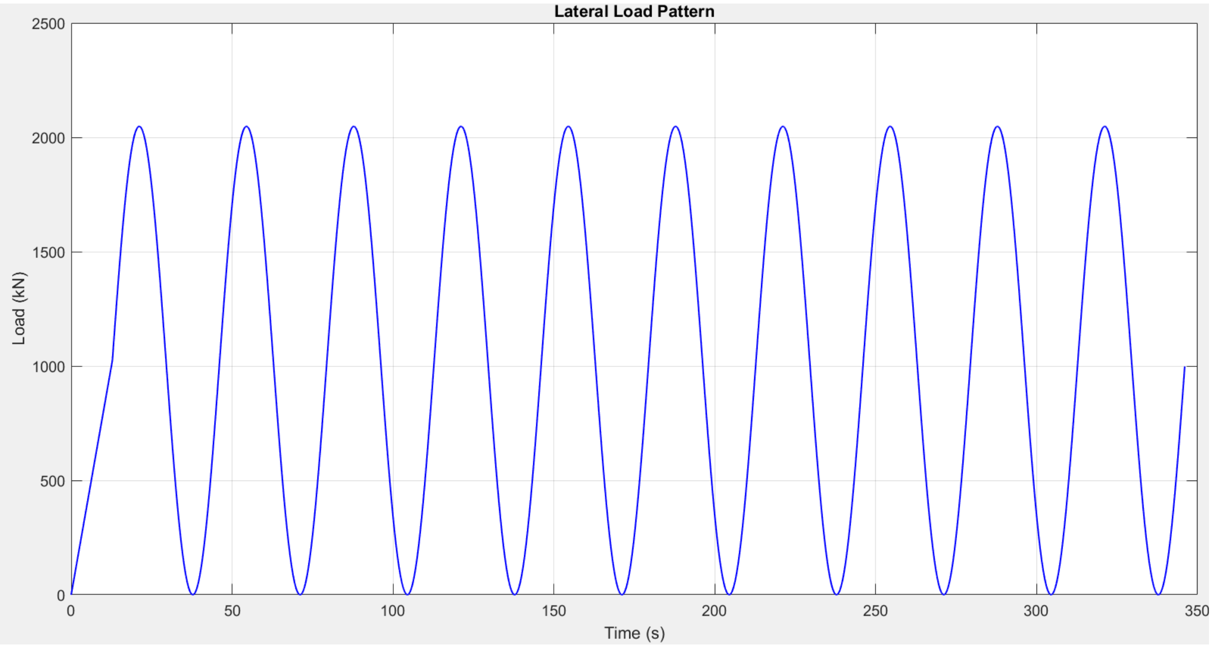

Figure 2.9: Load pattern of the lateral load to be applied after the installation stage.

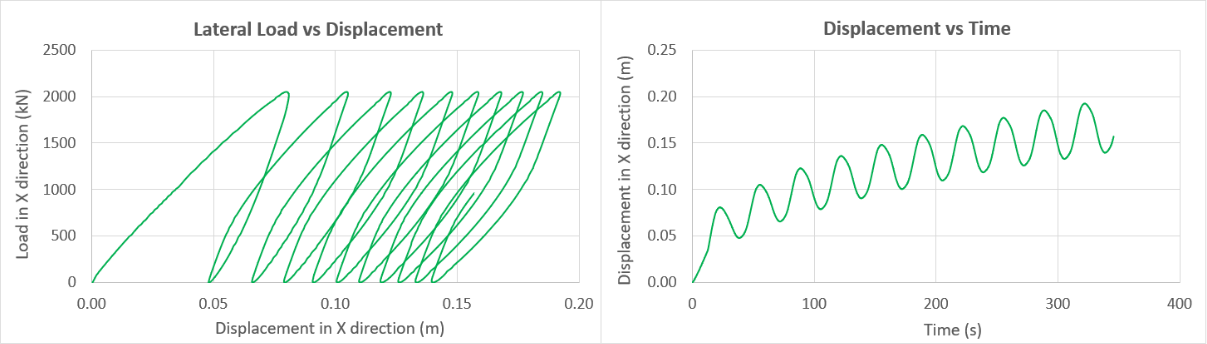

Figure 2.10: Load - displacement plot of the lateral load to be applied after the installation stage.

It is worth highlighting that, as depicted earlier, the load includes a gradual increase from 0 to 1000 kN at a uniform rate of 80 kN/s (monotonic loading stage), followed by the cyclic loading stage. This specific loading sequence is deliberately chosen to simulate one-way cyclic loading conditions. Recent research, including Haiderali et al. (2015), underscores the significance of such loading scenarios. They state that foundations experience greater challenges and exhibit a higher propensity for cyclic deformations accumulation when subjected to one-way loading, compared to two-way loading. This bias in loading direction represents a critical consideration and a more cautious approach in the design and assessment of foundation systems.

3 | Model

This chapter centers on the introduction and comprehensive explanation of the numerical model that is utilized, in later stages of this research, for simulating and examining the soil's response following the vibro-installation of the pile and the successful installation and lateral loading of the wind turbine. This model plays a pivotal role in grasping the intricate interplays happening within the soil and is the main aid to answer the research questions and uses, as a base, the model developed by Kementzetzidis et al. (2019). Through a thorough delineation of the model's attributes, assumptions, and capabilities, a strong groundwork is established for the upcoming sections of this study. The current chapter has been divided into segments to enhance clarity, addressing aspects such as mesh generation, the types of elements employed, the soil chosen for modelling, the specific mesh geometry and time-step selected, the properties and modelling of the monopile, and the boundary conditions.

It is important to emphasize that, as previously stated in this report, the model developed by Tsetas et al. (2023) is solely used to acquire the soil loads generated during the vibro-driving process. The researcher has not engaged in utilizing the model for obtaining these loads, as it is beyond the scope of this MSc. Thesis. Such loads serve as an input for the model generated by Kementzetzidis et al. (2019). Consequently, the subsequent sections will exclusively focus on describing the latter model, with no further elaboration on the former.

3.1 General Aspects and Description

The *OpenSeesPL* pre- and post-processor software is employed on this research to create the three-dimensional soil mesh. It includes the soil elements as well as those elements that, after the installation process, correspond to the monopile and the soil inside of it. Subsequently, the 3D model is introduced for computation into the *OpenSees* software, using scripts written in the *Tcl* programming language. *OpenSees* (Open System for Earthquake Engineering Simulation) is a package copyrighted by the University of California, Berkeley, that is designed to generate software applications capable of emulating the behaviour of structural and geotechnical systems under seismic conditions or cyclic loads overall. Its main goal is to improve the modelling and computational simulation in earthquake engineering (OpenSees Official Webpage, 2006) and, due to this enhanced competence, it effectively captures intricate non-linear phenomena and the viscous-plastic behaviour of soils. Due to these factors, it has been chosen for the numerical analyses in this project.

The *Paraview* software, which allows the performing of data analysis and user-friendly data visualization, is adopted throughout the research as a post-processor to track the displacements, stresses, strains, and other important outcomes of the analyses in the nodes and elements from the model.

The soil continuum and the embedded portion of the monopile are discretised and modelled using one-phase, low-order, eight-node hexahedral elements (bricks) with physically stabilized single-point integration, implemented in the OpenSees framework as *SSPBrick* elements. These elements, formulated as *H1ssp* elements by McGann et al. (2015), are chosen for their stabilization scheme, accuracy, increased computational efficiency, and their enhanced assumed strain field, which makes them devoid of volumetric and shear locking issues. They are configured in three dimensions and three degrees of freedom, as depicted in Figure 3.1. A depiction of an example of a generic, basic model for the numerical analysis after the monopile and the wind turbine are in place is shown in Figure 3.2 and every detail related to the mesh, soil, and monopile is further developed in subsequent sections.

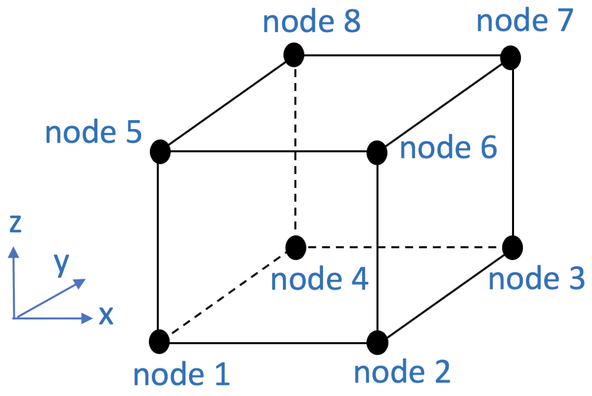

Figure 3.1: Brick element in OpenSees. (*Retrieved from OpenSees Official Webpage (2006)*).

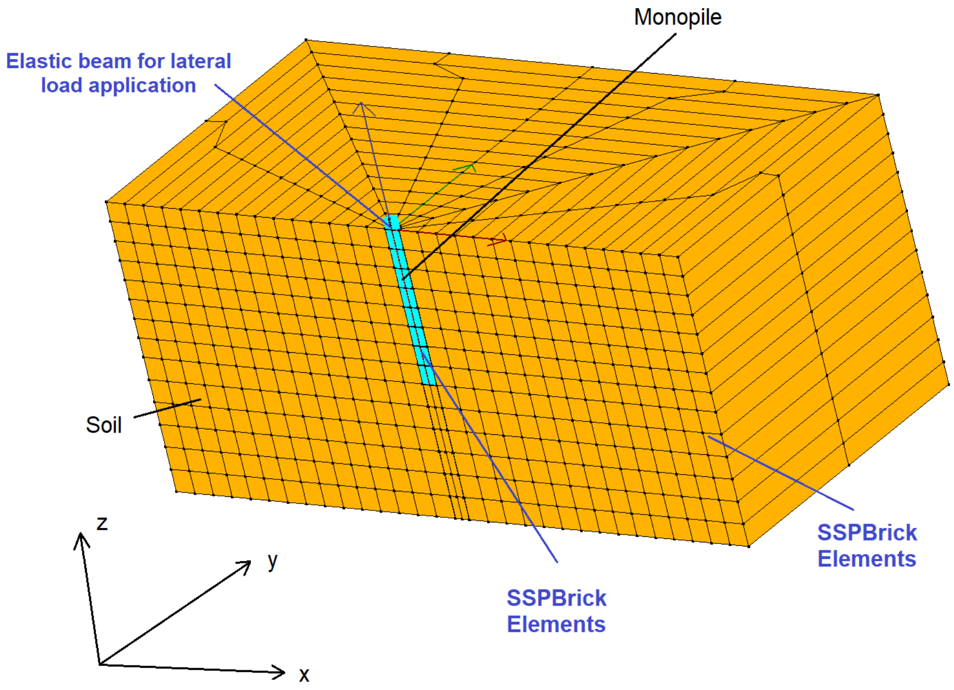

Figure 3.2: Example of a soil-monopile system mesh.

Modelling the cyclic behaviour of a monopile and surrounding soil through numerical simulations demands significant computational resources. This is owed to the problem's substantial size, non-linear and intricate nature, and the necessity for time integration methods to predict the system's temporal evolution (Xie & Lopez-Querol, 2021). Due to this, and because both the geometry and loads exhibit symmetry, only one-half segment of the model is simulated to enhance the computational efficiency, as observed in Figure 3.2. The elements are subjected to gravity (-9.81 m/s^2) as constant body force in the global z-direction.

Moreover, within this study, the modelled soil exhibits damping arising from both radiation damping, which entails the dissipation of waves in an expanding medium, and hysteretic damping, an inherent material property of the soil (Kementzetzidis et al., 2019). While this intrinsic damping effectively accounts for the influences stemming from vibrations at low frequencies, the analysis incorporates an extra damping source to accommodate energy dissipation resulting from the high-frequency oscillations arising from the vibro-installation process: Rayleigh damping. It is introduced into the simulation uniformly on the nodes' degrees of freedom, with the properties shown in Table 3.1. The damping matrix updates at every time-step and each node in the model experiences damping forces based on its velocity and displacement.

Table 3.1: Damping Parameters

Rayleigh damping parameter	Value	Unit
Damping ratio, ζ	2.0	$\%$
Lower frequency, f_i	0.8	Hz
Higher frequency, f_j	100.0	Hz
Factor applied to elements mass matrix, α_m	1.995 x 10^{-1}	s^{-1}
Factor applied to elements stiffness matrix, α_k	6.316 x 10^{-5}	s

The Rayleigh damping ratio, ζ, quantifies the level of damping in the system and provides insights into how the system's vibrations decay over time, i.e. it characterizes the rate at which the amplitude of a damped oscillation decreases (Chopra, 1995). The frequencies, ω_i and ω_j, correspond to the selected range of frequencies depicted in Figure 3.3. Further, the constants α_m and α_k are linked to these frequencies and the damping ratio of the system via the expressions depicted in Equation 3.1.1. These coefficients define the damping matrix, *C*, as shown in Equation 3.1.2, and represent its proportionality to the mass (*M*) and stiffness (*K*) matrices, dealing with forces generated by velocities of the model and with forces generated by strain rates of the model, respectively (Ekanayake et al., 2013).

$$\alpha_m = \zeta \frac{2\omega_i\omega_j}{\omega_i + \omega_j} \qquad \alpha_k = \zeta \frac{2}{\omega_i + \omega_j} \tag{3.1.1}$$

$$C_{Rayleigh} = \alpha_m \cdot M + \alpha_k \cdot K \tag{3.1.2}$$

Typically, the values presented in Table 3.1 are selected based on laboratory tests, aiming to accurately depict the real behaviour of the soil. However, due to the absence of experimental data in this particular study, a conservative approach is taken on the selection of these parameters. This involves considering a wide spectrum of frequencies below the ζ=2$\%$ to primarily address the attenuation of low frequencies resulting from the soil's self-excitation upon the introduction of loads into the system. Additionally, since frequencies around 20 Hz are predominantly anticipated from the vibrations induced by the installation loads, a sufficiently high upper limit frequency (ω_j) is chosen to minimize damping effects within the frequency range of primary interest. Furthermore, this choice, combined with the ζ=2$\%$, is made with care to prevent excessive damping and overly excessive filtering of certain ground motion components. Figure 3.3 illustrates ω_i and ω_j, revealing a lower damping ratio between them and significant damping at very low frequencies (ω < ω_i).

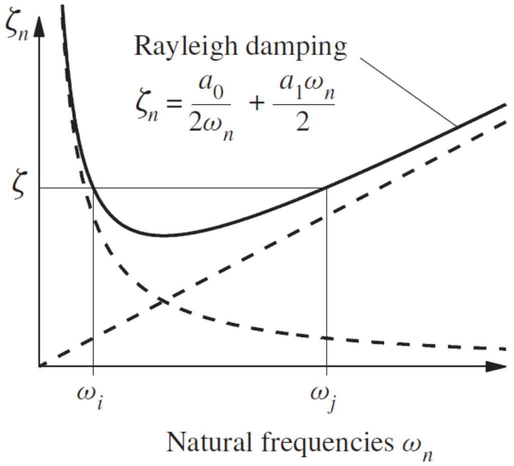

Figure 3.3: Rayleigh damping plot representing the variation of modal damping ratios with natural frequency. (*Retrieved from Chopra (1995)*).

All in all, including a 2$\%$ Rayleigh damping factor is justified by considering its primary role in damping out small vibrations. This choice is particularly relevant because larger vibrations are already effectively dampened by the inherent hysteretic damping characteristics of the constitutive model, as it exhibits a notable increase as strain amplitudes rise, but becomes negligible at small strains. To ensure a realistic representation of damping effects at lower strain levels, the incorporation of Rayleigh damping becomes essential.

The process of discretizing a problem in time and space to apply the finite element method might introduce high-frequency oscillations or instability in the solution which can lead to inaccurate or unrealistic results. Therefore, numerical damping is sometimes needed, which involves introducing artificial damping in a way that it effectively dissipates high-frequency energy. Nonetheless, while this can stabilize the simulation, it can also lead to a loss of accuracy in capturing the true physical behaviour of the soil response, since it does not represent a physical or real damping mechanism but rather a mathematical artifact. For this reason, the *HHT method* is selected as the time integration scheme for this research, elaborated in Section 2.3.3.

If the time-step chosen is too large or the integration method is not chosen carefully, numerical damping becomes necessary. As depicted in subsequent sections with a detailed explanation of the time-step and mesh discretization for this study, this process is carefully and thoroughly carried out. Accordingly, a low numerical damping is applied. As demonstrated in Section 2.3.3, reducing the value of α intensifies damping in the numerical solution, while higher α values correspond to reduced numerical damping. Specifically for this case, α is set to -0.10, γ is set to 0.5 - α = 0.60, and β is set to (1 - α)^2/4 = 0.30.

3.2 Soil

The soil used on this study is modelled as Karlsruhe fine sand. To account for both the installation and post-installation lateral effects, it is imperative to employ a constitutive model capable of accurately representing the stress and state-dependent behaviour of sand. Thus, the study employs the SANISAND model (Manzari & Dafalias, 2004). Before stating the soil characteristics, an overview and technical description of the key concepts, theories, and empirical studies related to the soil constitutive model is presented to establish a solid foundation and theoretical framework for the research and to provide a context for the subsequent research findings and discussions.

3.2.1 Soil Constitutive Model

Derived from mechanics, soil constitutive models are fundamental formulations utilized to define and characterize soil materials. They offer both qualitative and quantitative insights into the mechanical behaviour of the soil, serving as tools for illustrating the stress-strain relationship based on the soil's stress state. Additionally, they enhance the description of the material by highlighting its significant features.

The behaviour of the soil is influenced and depends on a variety of factors. While tests offer valuable insights into the behaviour of a specific soil sample under some specific test conditions, they cannot cover all possible combinations or scenarios. Moreover, conducting numerous tests to account for every potential combination of characteristics, test set-ups, stress levels, and so on, would be highly unwise and costly. To overcome this limitation, the use of practical constitutive models allows for quick, cost-effective, and reasonably accurate predictions of strength variations and deformation properties across the entire range of relevant stress levels and void ratios. Thus, such models provide a chance to establish a connection between the experimentally observed behaviour of a certain material and equations that possess appropriate physical significance.

A computational analysis of offshore wind turbine systems under environmental loads is intricately tied to the representation of cyclic soil behaviour. In recent years, multiple cyclic soil models have been formulated within different plasticity theories, contributing to a deeper understanding of this phenomenon. On the development of the present research, the soil is modelled using the Manzari-Dafalias comprehensive constitutive model for sands (Manzari & Dafalias, 2004), developed within the Critical State Soil Mechanics (CSSM) theoretical framework and being fully compatible with its principles. This particular model is primarily chosen due to its capability to effectively depict the complex non-linear mechanical behaviour of soils when subjected to cyclic loading with more simplicity and fewer model parameters compared to alternative models. Other advantages of using this model are presented in later sections of this research.

The following sections briefly describe the most important aspects and characteristics of the CSSM theoretical framework, followed by an overview of the Manzari-Dafalias model, its parameters and its advantages.

Critical State Soil Mechanics

Critical state soil mechanics is an effective stress framework that postulates the existence of an 'ideal soil or granular material that flows as a frictional fluid at constant specific volume (ν) when, and only when, the effective pressure (p') and axial-deviatoric stress (q) satisfy Equations 3.2.1 and 3.2.2'. The former determines the magnitude of the deviatoric stress needed to keep such continuous flowing of the soil, and the latter states that the specific volume occupied by unit volume of flowing particles will decrease as the logarithm of the effective pressure increases (Schofield & Wroth, 1968). As a summary, this framework implies that when a soil undergoes continuous deformation, such as shearing, until it transitions into a flowing state, it reaches a critical condition. In this Critical State, shear deformations keep occurring for fixed stresses and zero volumetric strain rate (Manzari & Dafalias, 1997). When coming to such final state, a critical void ratio (e_c), independent of the soil's initial state, is reached as well as a residual strength after large shear strains.

$$q = Mp' \tag{3.2.1}$$

$$\nu = \Gamma - \lambda ln(p') \tag{3.2.2}$$

M represents a stress-ratio and, when Critical State is reached, it is the slope of the CSL in the *p'-q* space (critical friction ratio or Critical State stress-ratio in compression). Furthermore, Γ is the parameter that determines the location of the isotropic normal compression line in the semi-logarithmic compression plane, ν - *ln p'*, and portrays a reference state. λ represents the compression index under isotropic conditions, being the slope of the normal compression line. Both equations are illustrated in the figure below (Figure 3.4).

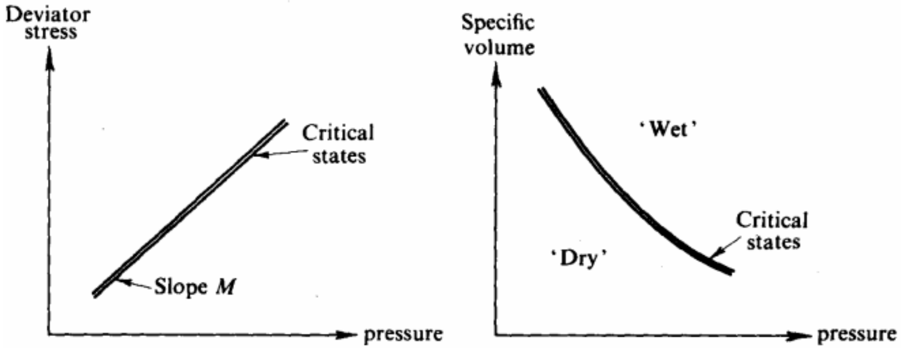

Figure 3.4: Representation of the Critical States. (*Retrieved from Schofield and Wroth (1968)*).

The initial equation (Equation 3.2.1) establishes that the deviatoric stress (q) required to maintain continuous soil flow is the product of a frictional constant (M) and the mean effective stress (p'). It represents a stress-ratio (M=q/p'). Meanwhile, the second equation (Equation 3.2.2), sometimes known as the *normal compression line* (Wood, 1991), asserts that the specific volume occupied by flowing particles per unit volume (ν = 1+e) experiences a logarithmic reduction as the mean effective stress increases. The constants M, Γ, and λ, previously described, represent basic soil properties. These equations allow the definition of a line, or locus, in the void ratio - mean effective stress space (e - ln p' space), which is called the Critical State Line (CSL), depicting the *Critical State* of a given soil. It is worth mentioning that this state does not indicate or represent a state of failure.

Casagrande (1936) was one of the first noticing that, when subjected to shearing, loose soils contracted and dense soils dilated until they reached approximately the same void ratio, later defined as the critical void ratio. A clear example is observed in sands where, at the Critical State, there is neither contraction nor dilation during shear deformation. If the sands are in a state looser than the Critical State, shearing causes contraction. Conversely, if they are in a denser state, shearing leads to dilation. In both scenarios, as shearing occurs, the material tends towards its Critical State, and there is no volume change during subsequent shearing. Such typical material response is visually represented in Figure 3.5: when a material with an initial state that is denser than critical (point a) is subjected to a drained constant-p triaxial compression, it contracts (from a to a_d') and, subsequently, dilates until reaching a_c' on the CSL (e=e_c). Under undrained conditions, point a moves first to a_d", due to the generation of positive pore water pressure, which reduces the effective stress and, then, due to a dilative tendency, it reaches the CSL at point a_c".

On the other hand, when the initial state is looser than critical (point b) the response differs. Under drained constant-p loading, the material contracts and reaches the CSL, without dilation or softening. As depicted in Figure 3.5, if the state at point b is not significantly looser than critical, the constant-p path may even cross the CSL and move to a denser point than critical before turning upward and reaching the CSL again. A similar scenario is observed for the undrained path.

Furthermore, Been and Jefferies (1985) introduced the State Parameter ψ as part of the CSSM framework, which is widely used for soil characterization and plays an important role as a controlling parameter in many soil models based on this principle. This parameter was defined to account for effective confinement stress levels and void ratio effects on the sand response (Been & Jefferies, 1985) and it is characterized as the deviation in void ratio from the soil's end state (Critical State) under the current mean effective stress (Equation 3.2.3). For the previous sand example, as shown in Figure 3.5, when the State Parameter is higher than zero (ψ>0), the sand is in a looser than Critical State. Contrariwise, when the State Parameter is lower than zero (ψ<0), it is in a denser than Critical State. The situation ψ=0 means that the material is already at Critical State.

$$\psi = e - e_c \tag{3.2.3}$$

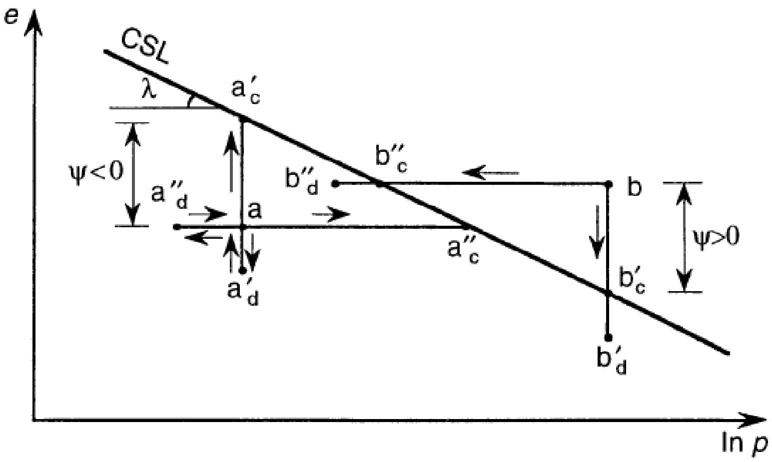

Figure 3.5: Schematic illustration of drained and undrained paths in an e, ln(p) space for a state denser than critical (point a) and looser than critical (point b). (*Retrieved from Manzari and Dafalias (1997)*).

The main parameters that are needed when employing the CSSM framework are the effective friction angle, ϕ', the compression index in one-dimensional compression, C_c (or the compression index in isotropic compression, λ), and the swelling index in one-dimensional compression, C_s (or the isotropic swelling index, κ, for unloading/reloading cases). It should be noted that the Critical State concept is primarily developed using reconstituted or remolded soil samples, which may not accurately represent the effects of factors such as cementation.

Many of the advanced soil models rely on the Critical State Soil Mechanics theory, such as the Cam-Clay model, which uses it as a core and main basis; NorSand; PM4Sand; Hypoplasticity; or Manzari-Dafalias bounding surface plasticity model, which will be used in this research and explained in the following section.

Manzari-Dafalias Constitutive Model

The current study uses the bounding surface plasticity and critical state model proposed by Manzari and Dafalias (2004), which builds upon their earlier research (Manzari & Dafalias, 1997). The latter model has been further expanded to incorporate the effect of fabric changes in sand during shear loading, since it was not able to appropriately model the effective pressure reduction under continuing undrained cyclic loading conditions. It has been considered as the soil constitutive model for this research to involve fewer model parameters, for efficacy and for simplicity.

The Manzari-Dafalias model (2004), hereafter referred to as SANISAND, implements the CSSM concepts and it is a comprehensive multi-axial constitutive model that simulates stress-strain behaviour of sands under both monotonic and cyclic loads, considering drained and undrained conditions. It uses a two-surface formulation of plasticity coupled with the state parameter, ψ, making an explicit use of it. The former takes place in the deviatoric stress-ratio space, the latter is used to define the peak and dilatancy stress-ratios of sand (Manzari & Dafalias, 1997) and they are linked together relating the bounding and dilatancy stress-ratios to the critical stress-ratio by means of ψ. A proposed peak stress-ratio surface is selected as a bounding surface and at ψ=0 both peak and dilatancy stress-ratios becomes critical. Such linkage enables the model to simulate the effects of both hardening and softening, as well as the changes in volume or development of pore water pressure in sand, at various densities and confining pressures. This also allows to employ a unique set of constants or model parameters for a specific type of sand in these simulations, independent of soil density and confining pressure values.

Within the general stress space, there are two distinct surfaces, the bounding surface and the dilatancy surface, as well as a critical surface (coming from the CSSM model). The bounding surface (M^b), used to simulate the (kinematic) hardening and softening behaviour along with the translating yield surface, represents the limit of the material's strength under various stress conditions and defines the maximum stress levels that the material can withstand before undergoing irreversible deformation or failure. It also allows to model reverse and cyclic loading response simulations (Kementzetzidis et al., 2019). On the other hand, the phase transformation or dilatancy surface (M^d) describes the material's tendency to dilate or expand in response to changes in stress. It characterizes the volumetric response and pore pressure development of the material under different states of confinement and density, allowing for the simulation of denser or looser states compared to the Critical State. The position of these surfaces depend on the current value of the state parameter ψ (Roy et al., 2020) and they are depicted in Figure 3.6a, as lines, in the triaxial space and in Figure 3.6b in the stress space.

When the stress-ratio (η=q/p) is above the dilatancy line in Figure 3.6a, dilation occurs, while if it is above the Critical State line and, at the same time, ψ>0, the soil contracts. Furthermore, this constitutive model postulates the existence of an open wedge-type yield surface in the triaxial space *q*, *p* (shaded area in Figure 3.6a), that will move together with the stress-ratio in a typical stress path and that, interacting simultaneously with the previously described surfaces, will aid in the understanding of the behaviour of sands. Such surface is added to delineate the start of the plastic strain region and, from it, it is clear that no deviatoric plastic deformation or volume strains occur if *q* and *p* increase at constant stress-ratio (dη=0) (Roy et al., 2020). If the stress level is within the current yield surface, the soil behaves elastically, i.e. behaviour being controlled by the elastic shear modulus (G) and bulk modulus (K), quantities that are stress level and density dependent (Roy et al., 2020). This could result in unrealistic results for pile driving because it assumes that the soil behaves elastically until it reaches such surface, whereas soils might exhibit non-linear behaviour in cyclic loading prior to approaching this point, specifically in the pile vicinity.

Furthermore, the model does not present a closing 'cap' at increasing *p*, since that would complicate the formulation significantly and it would not add considerable gain in the results when sands are being modelled (Manzari & Dafalias, 1997). The yield surface appears as a circular cone in the multiaxial stress space, with its apex at the origin, and it is circular in the deviatoric stress-ratio plane, as observed in Figure 3.6b.

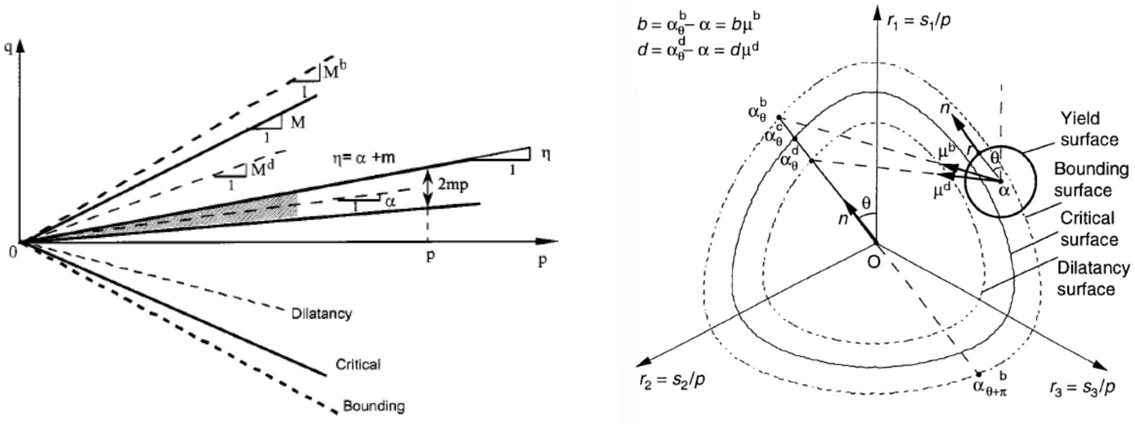

(a) Schematic of the yield, critical, dilatancy, and bounding lines in *q*, *p* space. (*Retrieved from Manzari and Dafalias (2004)*).

(b) Schematic of the stress-ratio π-plane of the yield, bounding, critical and dilatancy surfaces. (*Retrieved from Manzari and Dafalias (1997)*).

Figure 3.6: Manzari-Dafalias (1977, 2004) model surfaces

In addition, Manzari and Dafalias (2004) implemented some adjustments to the original model proposed by Manzari and Dafalias (1997). One significant modification involved incorporating the effect of a change in fabric of non-cohesive soils, which gives a realistic description of the soil response during reverse incremental and cyclic loading. This key addition was the inclusion of a fabric-dilatancy tensor, denoted as *z*, whose evolution during the dilative phase of shearing accounts macroscopically for the change and enables an improved contractile response when the loading is reversed following a phase that induces dilatancy. Thus, in this new version of the model, the dilatancy is made to depend on such tensor.

Constitutive Model Parameters

The SANISAND model uses constants such as the dimensionless modulus, G_0, and the Poisson's ratio, ν, to describe the pressure and density - dependency of the shear modulus, defining a hypoelastic response, i.e. *G* and *K* are considered functions of *p* and current void ratio, as observed in Equations 3.2.4 and 3.2.5. p_{atm} represents the atmospheric pressure, ν is the Poisson's ratio and G_0 is the elastic material constant.

$$G = G_0 p_{atm} \frac{(2.97 - e)^2}{1 + e} \left(\frac{p}{p_{atm}} \right)^{\frac{1}{2}} \tag{3.2.4}$$

$$K = \frac{2(1 + \nu)}{3(1 - 2\nu)G} \tag{3.2.5}$$

Moreover, the kinematic yield surface cone's size and, hence, the size of the elastic domain, is regulated by the parameter *m* (observed in the shaded area in Figure 3.6a), a stress-ratio quantity that is selected to be small in order to induce plastic strain nearly instantaneously upon the initiation of shearing (Ramirez et al., 2018). Further, as previously mentioned, the Critical State surface is defined in the *q - p'* space by the Critical State stress-ratio in triaxial compression, *M*, shown as a straight line in Figure 3.6a, and the ratio of Critical State stress-ratio in extension and compression, *c*. In the *p' - e* space, it is defined by the state line constants λ_c and ξ, and by the void ratio at $p_c = 0$, e_0, as shown in Equation 3.2.6 (suggested by Li and Wang (1998)).

$$e_c = e_0 - \lambda_c \left(\frac{p_c}{p_{atm}} \right)^{\xi} \tag{3.2.6}$$

The constitutive parameters h_0, c_h, and n^b define the plastic modulus, K_p, which plays a crucial role in determining how the soil's state changes in response to strain and, hence, controls the model's hardening and softening behaviour in the deviatoric space (Ramirez et al., 2018; Roy et al., 2020). The main factor that determines the value of K_p is the distance between the current stress state of the material and the bounding surface. On the same note, the amount of incremental plastic volumetric strains is proportional to the distance between the current stress-ratio and its corresponding projection on the dilatancy surface, as described by Rowe's dilatancy theory, i.e. if the stress state is higher, lower or equal to the dilatancy surface, a contractant, dilatant or zero volumetric rate response is obtained, respectively (Rowe, 1962). This is affected by the constitutive parameter n^d, which is a positive material constant that plays a role in determining the mobilized stress-ratio at phase transformation (dilatancy stress-ratio), and by the constitutive parameter that portrays the aforementioned proportionality and influences the rate of dilatancy, A_0. Manzari and Dafalias (2004) describes the latter as a positive quantity that is a function of the state.

Moreover, and as previously described, Manzari and Dafalias (2004) introduced a noteworthy addition to their earlier research, incorporating a symmetric second order fabric dilatancy tensor (z) into the updated model. This change was carried out mainly to account for the influence of fabric changes during sand's dilatation-contraction behaviour. The evolution of this tensor is regulated by two newly introduced parameters, c_z and z_{max}. The former is described as the main controller of the pace of evolution of z, and the latter the maximum value that z can attain.

Table 3.2 presents a summary of the parameters associated with the SANISAND constitutive model (2004). It is observed that it consists of a total of 15 parameters, from which M, c, λ_c, ξ, and e_0, are mainly used to describe the position of the Critical State line; G_0, ν and m mainly influence the elastic behaviour; and h_0, c_h, n^b, A_0, and n^d influence the plastic and dilatancy behaviour. The fabric parameters z_{max} and c_z play a key role in modifying dilatancy. The determination of most of all these parameters is based ideally in triaxial drained and undrained tests (static and cyclic) over a range of relative densities and confining stresses (Kementzetzidis et al., 2019).

Table 3.2: SANISAND Model Parameters

Model Constant	Variable	Description
Elasticity	G_0	Dimensionless shear modulus constant
	ν	Poisson's ratio
Critical State	M	Critical State stress-ratio in triaxial compression
	c	Ratio of Critical State stress-ratio in extension and compression
	λ_c	State line constant
	e_0	Void ratio at p=0
	ξ	State line constant
Yield Surface	m	Constant that determines the size of the yield contour (size of the elastic domain)
Plastic Modulus	h_0	Scalar parameter
	c_h	Scalar parameter
	n^b	Positive material constant that influences the bounding stress-ratio
Dilatancy	A_0	Dilatancy constant
	n^d	Positive material constant that influences the dilatancy stress-ratio
Fabric Dilatancy Tensor	z_{max}	Maximum value that z can attain
	c_z	Controller of the pace of evolution of z

Possibilities and advantages of using the SANISAND model

Compared to other constitutive models, the SANISAND model sets itself apart and stands out by uniquely integrating several advantages. While such advantages are found individually in other models, this model excels in bringing them together. Some of these noteworthy advantages include:

- It is capable of capturing the complex non-linear stress-strain behaviour of soils under various loading conditions.
- The model is based on Critical State soil mechanics. This is possibly its most attractive feature due to the simplicity and well-established framework of the Critical State theory for describing the mechanical behaviour of soils.
- The simplicity of the mathematical formulation and the number of parameters involved in the definition of its yield surface results in simple general constitutive equations. Furthermore, the model's numerical efficiency is high because it only needs to update the yield surface due to kinematic and isotropic hardening. The remaining surfaces are entirely determined by the value of the state parameter, ψ.
- The need for accurate soil constitutive models to predict soil behaviour often leads to complex models with numerous parameters, some of which may even lack clear physical interpretation. In contrast, SANISAND utilizes a small number of parameters, with a calibration comparatively straightforward when compared to other models.
- The fact that the dilatancy and the peak-stress ratio depend on the state parameter unifies the constitutive description of sandy soils. This allows to define a specific set of model constants for a particular type of sand, which remains consistent regardless of variations in soil density or the applied pressure.
- The next step is solely determined by the current state of the model, without requiring any usage of memory or recollection of past stress reversal points or accumulated strain measures.
- According to Manzari and Dafalias (1997), the SANISAND model can attain equivalent outcomes to multi-surface models while requiring significantly less computational effort. Moreover, it encompasses extra attributes, such as softening and zero dilatancy at Critical State.
- Due to the addition of an evolving fabric-dilatancy tensor that is able to model the fabric changes in the soil, it is widely used to simulate the effective stress reduction under undrained cyclic loading which gives a realistic description of soil response in reverse loading.
- On the same note, due to this fabric-dilatancy tensor, the model is able to capture different cyclic loading phenomena, such as liquefaction in saturated sands. This is essential for assessing the seismic stability of structures on sandy soils.

The SANISAND model, which incorporates a wedge-type open yield surface, is not able to capture the oedometric behaviour accurately, according to some studies carried out by Wichtmann et al. (2019). They declare that in order to account for a correct assessment of the volumetric behaviour under oedometric conditions, or for cases where the settlement is of interest, the yield surface shape should be reformulated. Moreover, it is stated on their analyses that the SANISAND model does not perform optimally under monotonic conditions. Nonetheless, as the scope of this research encompasses only cyclic loads, the SANISAND model is considered as the preferred choice.

3.2.2 Evaluated Soil

As previously mentioned and described, the soil for this study is modelled as Karlsruhe fine sand, dry, employing the SANISAND model (Manzari & Dafalias, 2004). The parameters specific to this sand and those utilized in the research are sourced in Table 3.3. The determination of these parameter values for this particular sand involved laboratory experiments and subsequent calibration conducted by Wichtmann et al. (2019). The authors outline the calibration procedure as follows:

- The Critical State parameters, e_0, λ, and ξ were derived from data obtained from numerous undrained monotonic triaxial tests conducted on Karlsruhe fine sand, encompassing variations in initial relative density and mean effective stress.

- The values of M_c, M_e, and consequently, *c*, were extracted from the slope of the final phase of effective stress paths observed in undrained monotonic triaxial tests. Specifically, these values were determined using the Mohr-Coulomb relations, and a critical friction angle of φ_c = 33.1º, in conjunction with the expression $M_e = 6 \sin \varphi_c / (3 + \sin \varphi_c)$.
- The value for the *m* parameter was adopted from the work of Manzari and Dafalias (2004) in order to ensure an accurate representation of the small-strain response.
- According to Wichtmann et al. (2019) in their calibration process for the SANISAND parameters of the Karlsruhe fine sand, the shear modulus coefficient, G_0, was selected to achieve a realistic estimation of the initial stiffness in drained monotonic triaxial tests. Moreover, it was subsequently slightly adjusted based on cyclic tests to achieve a better reproduction of stiffness.
- To approximate the experimental data for oedometric stiffness, this type of sand required a considerably low and unrealistic value for the Poisson's ratio.
- h_0 and c_h were adjusted iteratively to achieve the closest possible match between the stress-strain relationship $q(\varepsilon_1)$ obtained from simulated results and that measured in drained monotonic triaxial tests. Likewise, n^b was adopted to replicate the peak deviatoric stresses measured in these tests, while n^d and A_0 were chosen to reproduce the volumetric response $\varepsilon_v(\varepsilon_1)$ in the best possible manner.
- Lastly, the fabric-related parameters z_{max} and c_z were chosen to emulate the cyclic mobility effect observed in one of the performed undrained cyclic triaxial tests.

The comprehensive explanation of the meanings for each of the parameters in Table 3.3 is located in the Section 3.2.1 of this report.

Table 3.3: Material parameters of the SANISAND model for Karlsruhe fine sand (Wichtmann et al., 2019)

Parameter	Value	Unit	Laboratory test used for calibration
e_0	1.103	–	Critical State line in *e-p* space
λ	0.122	–	Critical State line in *e-p* space
ξ	0.205	–	Critical State line in *e-p* space
M_c	1.34	–	Undrained monotonic triaxial test
c	0.70	–	Undrained monotonic triaxial test
m	0.05	–	–
G_0	150.00	–	Drained monotonic triaxial test and undrained cyclic triaxial test
ν	0.05	–	Oedometric test
h_0	10.50	–	Drained monotonic triaxial test and undrained cyclic triaxial test
c_h	0.75	–	Drained monotonic triaxial test
n^b	1.20	–	Drained monotonic triaxial test
A_0	0.90	–	Drained monotonic triaxial test
n^d	2.00	–	Drained monotonic triaxial test
z_{max}	20.00	–	Undrained cyclic triaxial test
c_z	10,000	–	Undrained cyclic triaxial test

As briefly mentioned earlier, in this analysis the soil medium is modelled as dry for simplicity, making computations and calculations easier and reducing the number of parameters needed. However, this study focuses on offshore wind applications, which involve water-saturated conditions. Saturated soils exhibit different long-term behaviour compared to dry soils, leading to performance issues not predicted by the models studying the latter. This discrepancy arises because such models do not account for excess pore pressure generation, consolidation, liquefaction potential, or the different responses under cyclic loading conditions.

Nonetheless, studying soil and monopile behaviour under dry conditions can still provide valuable insights that can aid in understanding pile installation in offshore environments. These studies provide a foundational and preliminary understanding:

- Studying the interaction between monopiles and dry soil helps establish fundamental principles and mechanisms such as stress distribution or pile deflection under different loads. These principles are also applicable to saturated conditions, though modified by factors like pore pressure.
- Understanding how a dry soil reacts to different loads can provide initial insights into how the monopile might behave under similar loading conditions in saturated soils. The qualitative behaviour (stress concentration zones, deformations) will have similarities, even if the quantitative aspects differ.
- Observations from dry soil studies can serve as a benchmark for validating more complex models that include saturation effects. They can even serve as a starting point for building the whole infrastructure for more complicated numerical analyses in the future, i.e. with saturated soil analyses. Further, different parameters can be compared against saturated conditions to identify the most critical factors influenced by such saturation.
- In some scenarios, dry soils have a higher shear strength when compared to saturated soil, potentially providing a conservative upper bound.

On another note, the analyses center on initially dense soil conditions, specifically with a relative density of $D_R = 80\%$, as the primary emphasis is placed on dense soil states, which are frequently more relevant in the offshore environment. The initial void ratio of the soil is e = 0.76, linked and consistent with the initial relative density. Further, the soil mass density is $\rho_s = 1.60$ g/cm^3. These soil properties and initial conditions are summarized in Table 3.4.

Table 3.4: Soil properties and initial conditions

Initial relative density, D_R	Initial void ratio, e	e_{min}	e_{max}	Soil mass density, ρ_s
%	–	–	–	g/cm^3
80.0	0.76	0.67	1.10	1.60

Given the research's primary objective, it is crucial to highlight Equation 3.2.7. This equation forms the fundamental basis for calculating relative density at each examined time-step, which is critical since it affects the foundation's ability to resist such lateral forces. Understanding the variability of this parameter in these type of analyses bears paramount importance: relative density has a significant effect on safe bearing capacity of sandy soils and, in general, on how the foundation soil behaves under different loading scenarios.

It is expressed in terms of void ratio and, specifically, it is defined as the ratio of the difference in void ratios of a cohesionless soil in its loosest state (e_{max}) and its natural state (e) to the difference between the void ratio in its loosest state and its densest state (e_{min}). Equation 3.2.8, (Upadhyaya, 2005) illustrates the relationship between the void ratio and its corresponding plastic volumetric strain. The relative density is obtained by the combination of these two expressions, being the plastic volumetric strain derived as an output of the FE analyses.

$$R_D = \frac{e_{max} - e}{e_{max} - e_{min}} \tag{3.2.7}$$

$$d\varepsilon_v = -\frac{de}{1 + e_i} \tag{3.2.8}$$

Furthermore, the maximum and minimum void ratios for the Karlsruhe sand were established through standardized laboratory tests on minimum and maximum density, conducted by the research team that also calibrated the SANISAND parameters specific to this sand type. They are documented in Wichtmann et al. (2019) and shown on Table 3.4.

Using the specified parameters and the formulation introduced by Manzari and Dafalias (2004) for the SANISAND material, shown in Equation 3.2.4, the initial depth evolution of the shear modulus within the examined soil is plotted. Concurrently, the cone resistance's (q_c) variation with depth is also plotted. The latter is derived from an empirical equation for evaluating geotechnical properties of sands, put forth by Jamiolkowski et al. (2003) and shown below in Equation 3.2.9. It employs the relative density, vertical effective stress, and certain empirical correlation factors as input parameters. Both depth profiles are illustrated in Figure 3.7), they are used as one of the intakes for the vibratory-piling model and, hence, to obtain the loads generated by this installation procedure.

$$q_c = C_o p_a \cdot (\sigma'/p_a)^{C_1} \cdot exp(C_2 D_R) \tag{3.2.9}$$

q_c corresponds to the penetration resistance of a cone penetration test, D_R is the relative density of the soil as decimal, σ' refers to an initial effective geostatic stress, p_a represents the atmospheric pressure expressed in the same unit system of stress and penetration resistance, and C_o, C_1, and C_2 are non-dimensional empirical correlation factors that, after some experimental fittings performed by Jamiolkowski et al. (2003) for similar sands, were determined to be 17.68, 0.50 and 3.10, respectively.

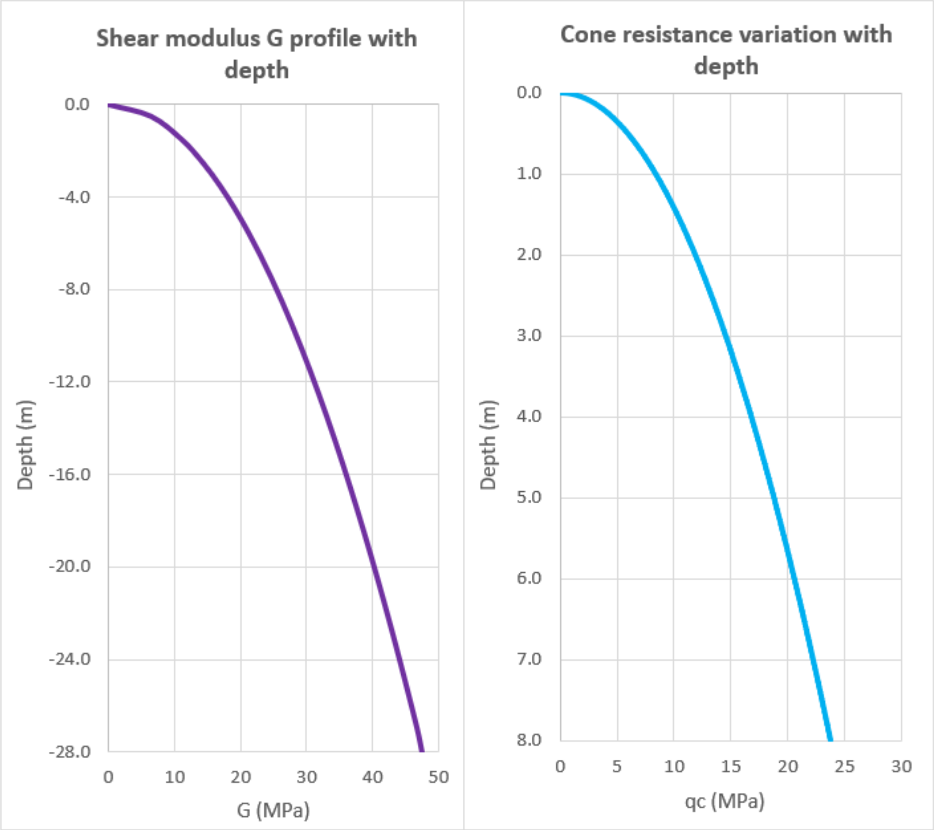

Figure 3.7: Evolution of certain soil parameters with the depth. Left: G profile vs depth. Right: q_c profile vs depth.

3.3 Monopile

In addition to the soil conditions detailed earlier, the model features a 762 mm outer diameter, 15.9 mm thickness steel pipe monopile driven 8 m into the Karlsruhe homogeneous fine sand. As highlighted before, the modelling approach for this offshore foundation employs 8-node hexahedral SSPBrick elements, which effectively eliminate shear locking. This feature permits users to adopt a coarser mesh, enhancing accuracy when dealing with problems primarily influenced by bending forces, as is the case in this particular study (McGann et al., 2015). The pile is represented in the simulation as a linear-elastic isotropic three-dimensional hollow solid structure, utilizing the linear-elastic characteristics of steel outlined in Table 3.5. Given its considerably higher stiffness compared to the adjacent soil, the likelihood of the pile undergoing excessive strains beyond its yield threshold is minimal.

Table 3.5: Monopile properties

Property	Value	Unit
Outer diameter, D_o	0.7620	m
Inner diameter, D_i	0.7302	m
Thickness, t	0.0159	m
Embedment length, L	8.0	m
Young Modulus, E	210.0	GPa
Poisson's ratio, ν	0.3	–
Mass density, ρ_p	7.85	g/cm^3
Section	Circular	–

On the other hand, after the installation of the monopile is carried out, some theoretical elements are integrated at the mudline to accommodate the application of lateral loads stemming from the offshore environment, as described in Section 2.4. They are included at the pile nodes at the mudline. It is modelled and simulated adding linear-elastic beam elements, connected to the the monopile head via rigid links at the mudline (z=0). These elements are introduced into the model exclusively during the lateral loading test (i.e. environmental loads), conducted subsequent to the monopile installation. They are incorporated in three dimensions and feature six degrees of freedom, which allows them to effectively respond to three-dimensional loads, providing both moment and torsion reactions across all three directions.

In what regards to the soil-pile interface, the intention was to create a simple and straightforward representation of the interaction between the soil and the pile. This was planned to be achieved by incorporating elements that depict degraded soil in the vicinity of the monopile, represented by a weaker and more deformable soil material. However, because of time constraints and difficulties in achieving model convergence while attempting to incorporate these elements, such simulation of the interface has not been implemented, and it stands as a recommendation for future studies in this area.

3.4 Boundary Conditions

In the realm of dynamic calculations, the correct selection of boundary conditions holds paramount importance in simulating real-world scenarios with accuracy, owing to the potential impact of wave reflection at these boundaries on the resultant outcomes of the analyses. To mirror the physical environment, a combination of displacement boundary conditions has been meticulously applied.

First, the model requires the symmetric boundary condition (symmetry with respect to the y=0 plane) to be applied to both pile and soil elements, which means that any displacement in the -Y direction for all nodes contained in such symmetrical plane is prevented, i.e. a constraint condition of zero normal displacement is applied there. Furthermore, the nodes at the bottom of the soil layer (with a z = min(z) coordinate) are subjected to roller constraints, enabling movement along the X and Y directions, but restricting any vertical displacement; to reproduce underlying rigid rock conditions. Conversely, the surface of the soil layer is completely unrestricted in its movement across all three dimensions. The system is initially at rest (zero initial velocities and accelerations).

Moreover, when an infinite domain is modelled by finite discrete subdomains, waves exhibit a tendency to reflect upon encountering the finite boundary of the mesh. This phenomenon subsequently exerts a substantial impact on the overall system's response (Kim, 2014). For this reason, the dissipation of vibrational energy at the periphery of the model is simulated integrating artificial absorbing boundary elements called dashpots, or viscous dampers, into the outermost nodes. They operate in conjunction with the existing constraints, facilitating the controlled absorption of energy in the boundaries during dynamic loading and interactions, annihilating such effect of the reflected waves caused by the discretization of the infinite domain. Further, these dashpots are modelled in OpenSees by creating external nodes on the outer nodes of the mesh, with three degrees of freedom, and generating *zero-length elements* with viscous material properties. The nodes subjected to these dashpots showcase a resistive response, effectively emulating damping effects and avoiding that the vibrations reaching these nodes return to the source as artificial disturbances to the real vibrations. This approach is employed since it has demonstrated considerable effectiveness and accuracy in specific research, as detailed in the study by Kim (2014). Additionally, Ong et al. (n.d.) suggests that it is used as a means to minimize the size of the finite element domain.

If during the simulation, for example, lateral stress increases, it typically leads to an increase in the deformation and motion of the soil mesh. The relative velocities at the nodes where dashpots are connected change and dashpots respond to this velocity changes by generating damping forces that oppose such motion. This opposition leads to energy dissipation, which helps in stabilizing the system and reducing the amplitude of vibrations even for situations in which the lateral stress is changing.

An overview of the boundary conditions is illustrated in Figure 3.8, showcasing the restricted vertical displacement at the lower nodes, the unrestricted upper surface, and the lateral dashpots. The visualization is presented in a two-dimensional representation, focusing on the X-Z plane for clarity; however, these conditions are extrapolated in the simulated model to also encompass the three-dimensional plane (Y-plane). It is important to highlight, as depicted in the Figure, that the use of viscous dampers is limited to the lateral boundaries of the mesh. Meanwhile, at the bottom, displacement is solely restricted vertically, simulating an interface with the bedrock. This choice is related to the fact that the selected mesh depth is sufficiently deep, causing the compression waves to almost entirely dissipate before reaching this boundary. This is explained further in Section 3.5 in which the mesh sensitivity analysis is described.

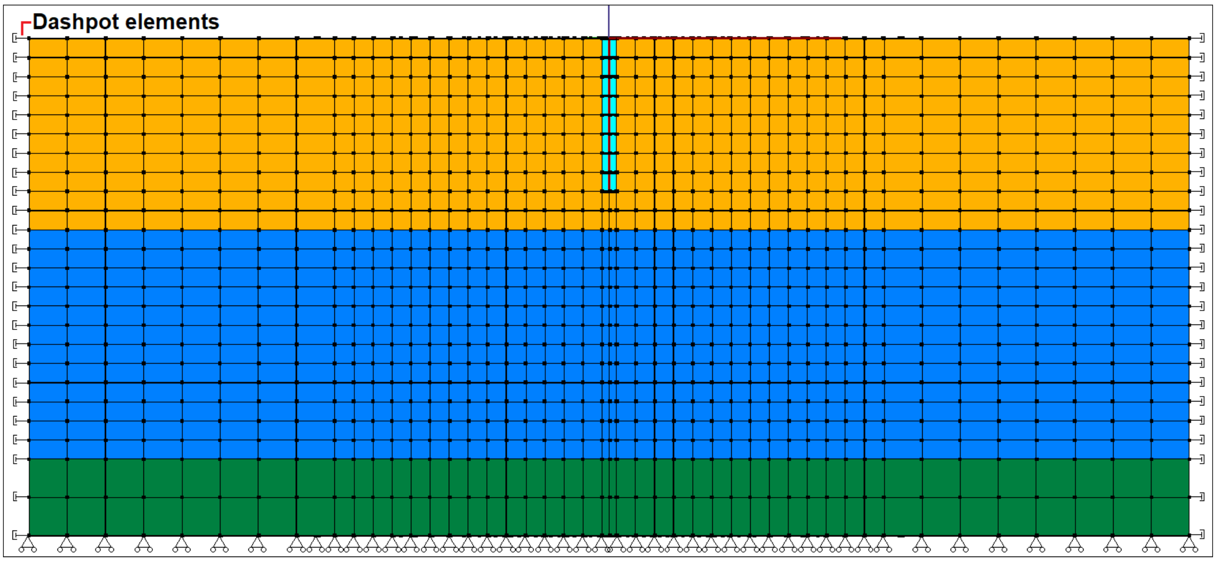

Figure 3.8: Boundary conditions of the problem in 2-D for clarity.

Although the roller boundaries at the bottom of the mesh suggest that compression waves might reflect back, the effects of plasticity, damping, and an appropriately sized mesh in the Z direction reduce this likelihood, as the waves are attenuated before reaching the bottom.

3.5 Sensitivity Analysis

The reliability and fidelity of a numerical simulation are intricately tied to the discretization parameters employed within the simulation. The two main parameters that significantly influence and control its accuracy and computational efficiency are the time-step and the mesh size and geometry (Jeremić et al., 2009). The former dictates the temporal resolution of the simulation, affecting how well the dynamic behaviour of the system is captured over time. Further, the latter defines the spatial discretization, determining the level of detail in representing the geometry and material distribution within the domain.

Although there are readily available guidelines in this matter for dynamic analyses in the context of seismic loads, it is essential to acknowledge the unique considerations that come into play in analyses when dealing with artificial dynamic loads, such as those generated during the vibratory installation of a monopile (Schepers et al., n.d.). Due to this rationale, a sensitivity analysis of FEA results to variations in time-step and mesh size necessitates a comprehensive exploration to determine the optimal combination of these parameters. In this section, a rigorous sensitivity analysis of time-steps and mesh sizes in the context of a finite element model applied to soil subjected to dynamic loading is thoroughly carried out. By systematically varying these parameters and evaluating their impact on the simulation results, the aim is to shed light on the interplay between accuracy and computational cost.

3.5.1 Time-step

The time-step, as a discrete increment in time, plays a pivotal role in capturing the dynamic behaviour of the soil system under varying loading conditions. Accurately capturing the temporal behaviour of the system is crucial: if the time-step is too large, important transient behaviours might be missed, leading to inaccurate results. Further, with such large time-steps, a given wave front might reach two consecutive nodes at the same time, leading to instability (Jeremić et al., 2009; Watanabe et al., 2017).

In this section, the effects of different time-step values on the simulation results is systematically explored, aiming to strike a balance between temporal accuracy and computational cost: selecting an appropriate time-step range that yields truthful results without excessive computational burden. This is achieved by varying the time-step while keeping the domain and mesh size constant: as the time-step decreases, the solution progressively approaches convergence with the real problem's solution. Nonetheless, exceedingly small time-steps need to be avoided, since they can lead to inconsistencies and numerical disruptions.

A sufficiently wide mesh in the three-dimensions is chosen: lateral distance of around 40 times the diameter of the monopile (± 30.37 m in the X-axis and 30.37 m in the Y-axis); depth equivalent to three times the embedment length (24 m); and grid elements of 1 m for both Δx, and Δz (Figure 3.9). The selection of the latter is guided by the theoretical principle for soil dynamics simulations, ensuring a minimum of 8 to 10 nodes per wavelength (Jeremić et al., 2009; Lysmer & Kuhlemeyer, 1969; Watanabe et al., 2017). Furthermore, the soil is considered as an elastic medium.

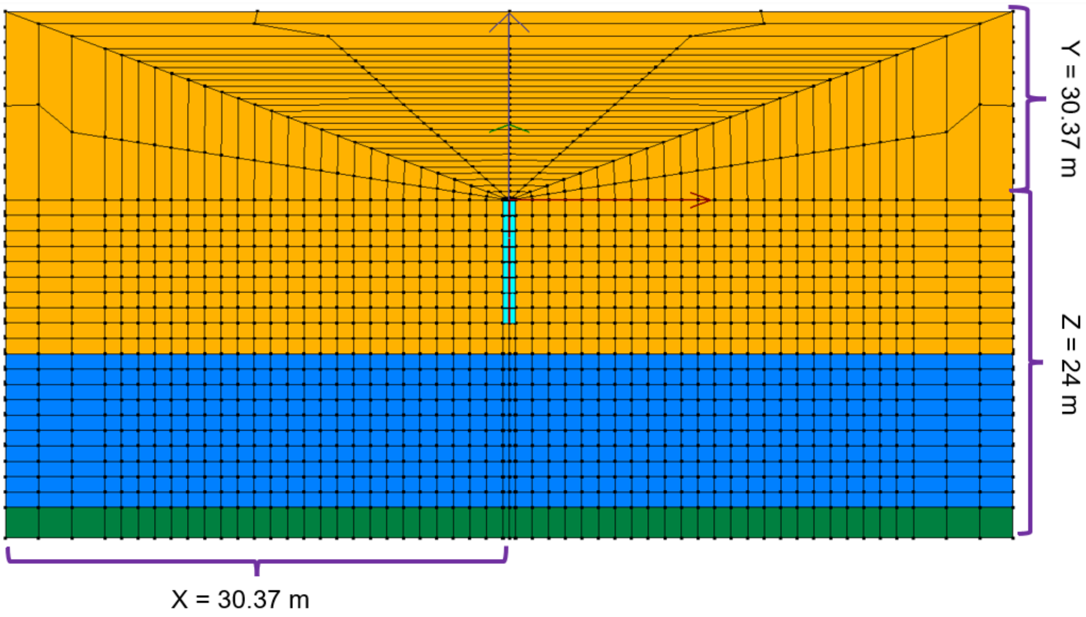

Figure 3.9: Mesh for the time-step evaluation and selection.

Another crucial factor that is important to replicate is the nature of the applied load. In this case, the sensitivity analysis employs loads that are simpler in nature yet share similarities in their properties with the loads generated during the vibro-installation of the monopile. This approach is undertaken primarily to gain insights into the behaviour and to accurately select an appropriate time-step with a rather simpler response. The load command applied for this stage involves a sinusoidal, compression, cyclic load with a frequency of 23 Hz and an amplitude of 560 kN. It is applied to all the nodes within the pile shaft, resulting in an allocation of over 3 kN load amplitude per node in this particular mesh configuration (Figure 3.10). These parameters are chosen as they align with the standard installation configurations for vibro-piling.

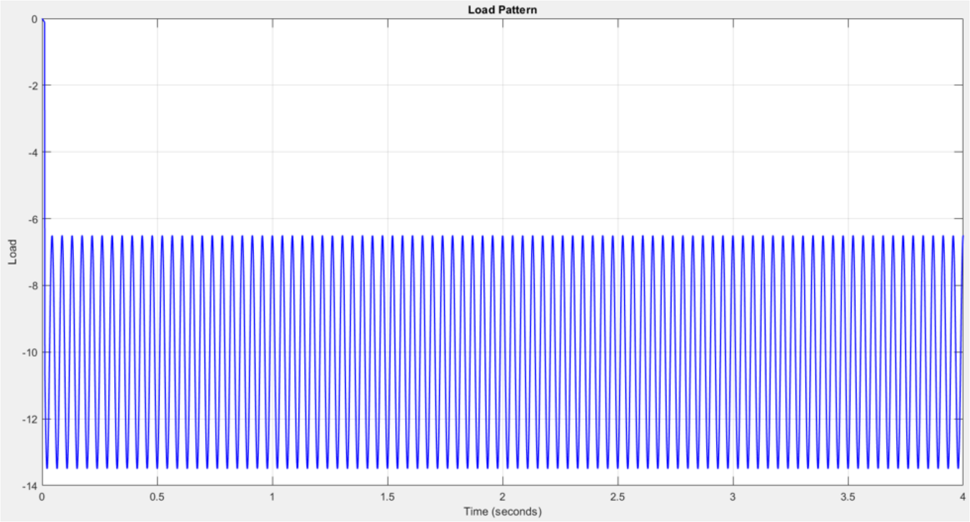

Figure 3.10: Load applied for performing the (time-step) sensitivity analysis.

To establish suitable time-step orders of magnitude to explore in the sensitivity analysis, the formulation proposed by Watanabe et al. (2017), outlined in Equation 3.5.1, is applied. It suggests that, for a linear-elastic analysis, the maximum allowable time-step should be determined by dividing the maximum grid spacing by the shear wave velocity (V_s), which is a function of the Young's modulus, *E*, or the elastic shear modulus, *G*, the soil mass density, ρ, and the Poisson's ratio, ν. Adhering to this expression, an initial time-step of Δt = 0.005 seconds is chosen for the commencement of the time-step sensitivity analysis. It represents a good starting point, as it also coincides with the findings of Jeremić et al. (2009) regarding this matter: the smallest fundamental period of the system (1/f = 0.04 seconds) needs to be represented with at least 10 time-steps.

$$\Delta t \leq \frac{\Delta x}{V_s} \qquad\qquad V_s = \sqrt{\frac{E}{2(1+\nu)\rho}} = \sqrt{\frac{G}{\rho}} \tag{3.5.1}$$

Five different time-steps are examined (0.0002 seconds, 0.0005 seconds, 0.001 seconds, 0.002 seconds, and 0.005 seconds), along with their resulting behaviours, for nodes situated both in close proximity to the pile and at a significant distance from it. Additionally, nodes positioned at the boundaries are monitored to ensure and confirm the accurate performance of the dashpots.

Once the time-dependent displacement in the X and Z directions is assessed, an optimal time-step of Δt = 0.001 seconds is chosen. A demonstration of the elastic time response is depicted in Figure 3.12 focusing on a node situated near the pile's vicinity, at a depth of 2 meters (red circle in Figure 3.11). Notably, at the elected time-step, it is evident that the solution aligns with that obtained from smaller time-steps. A consistent pattern is discernible across all assessed nodes within the mesh. Moreover, the effectiveness of the dashpots is confirmed, evidenced by minimal vibrations near the boundaries and by the absence of vibrations reflection.

Moving forward to subsequent sections, following the determination of both domain size and mesh density, a series of time-steps are once again tested using the new established settings. The purpose is to double-check the consistency and validate the suitability of the chosen time-step.

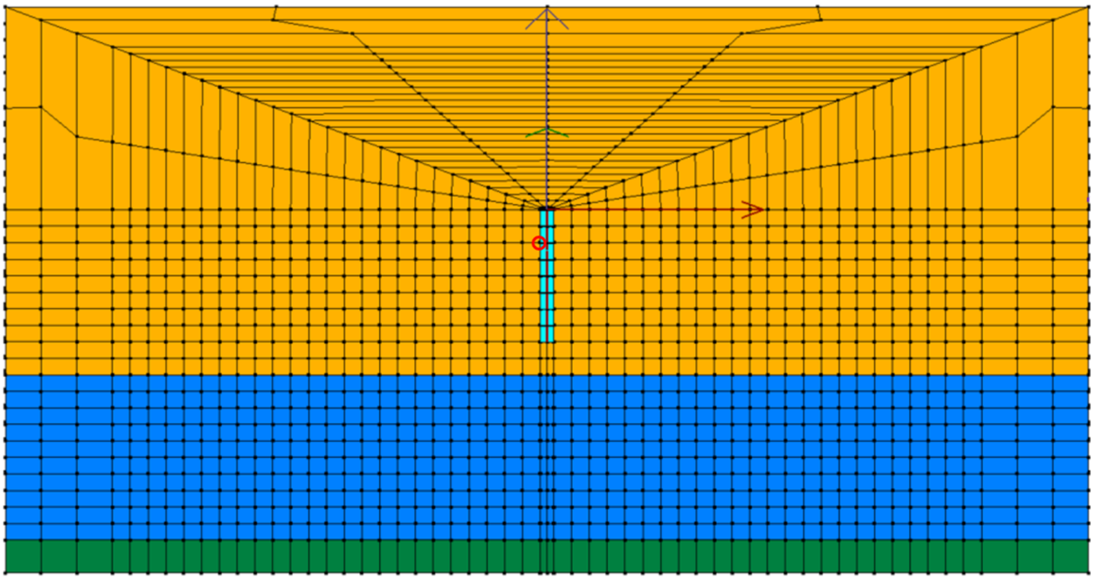

Figure 3.11: Location of the node which response is depicted in Figure 3.12 - illustrative mesh.

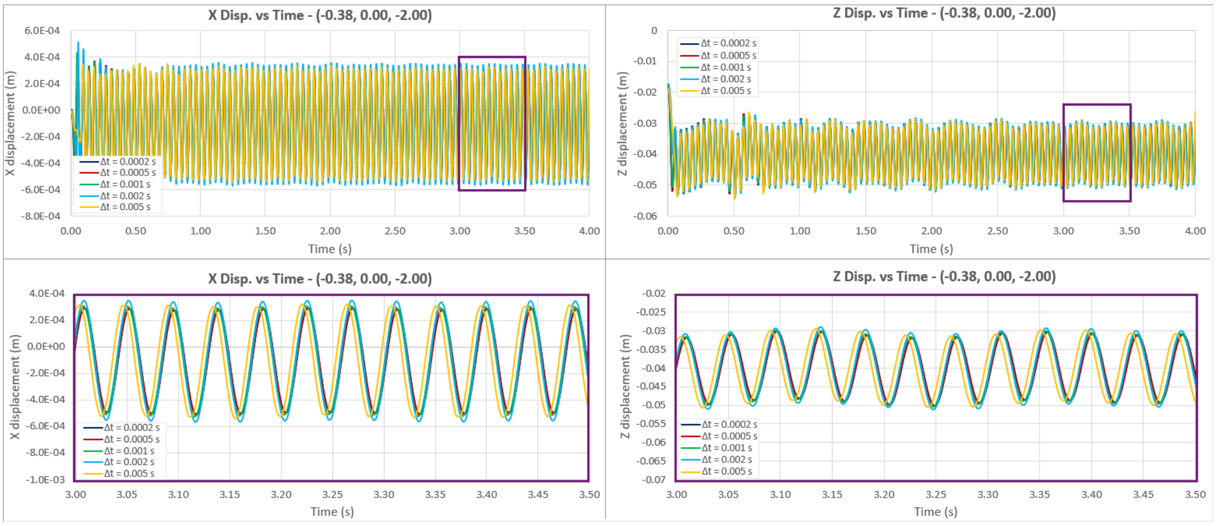

Figure 3.12: Example of the time response in terms of displacement for a node at the vicinity of the pile - different Δt values.

3.5.2 Domain size

After selecting the time-step, the next stage includes the selection of the X, Y and Z sizes for a proper simulation of the soil response. Careful thinking and definition of the location of these boundaries is crucial to guarantee the accuracy of the analytical results, as previously explained, to minimize boundary influence on the calculation outcomes.

Initially, the depth of the mesh is selected by testing different Z values, while maintaining the same considerably large X and Y dimensions (Figure 3.9). The primary rationale behind first choosing the depth and subsequently determining the lateral extent relates to wave propagation. This approach accounts for the quicker attenuation of body waves and the fact that surface waves, which predominantly propagate laterally, cover larger distances before experiencing attenuation. Consequently, waves reaching the lower boundary are likely to attenuate first, making the depth less influential in the model compared to radial distance. Hence, in this stage the main goal is selecting a domain that is deep enough, i.e. body waves are able to dissipate before reaching the bottom boundary.

Furthermore, the soil continuum is considered as elastic for both the mesh's depth and lateral extent assessment. The main reason for this comes from the fact that if a plastic soil is used instead, it will introduce energy dissipation, intrinsic from plastic behaviour. Consequently, the energy transmitted to the boundaries is expected to be reduced when contrasted with the linear scenario, where energy dissipation solely arises from material damping. As a result, relying on a domain size estimation derived from a linear medium provides a reasonably conservative approach.

The tested depths are Z = 2·L = 16 m, Z = 3·L = 24 m, Z = 3.5·L = 28 m, and Z = 4.25·L = 34 m. All of them evaluated with a $\Delta t = 0.001$ seconds, as the suitable time-step defined in the previous section. After the analyses, a Z = 28 m deep soil mesh is chosen. A demonstration of the time response is depicted in Figure 3.14 for the different values tested, focusing on a node situated near the pile's vicinity, at the plane of symmetry and at a depth of 4 meters (red circle in Figure 3.13). The same response is observed in the rest of the nodes throughout the mesh, with outcomes converging consistently from 28 m upwards. Subsequently, different evaluations of time-steps are conducted again for this revised depth, yielding similar outcomes to those previously demonstrated. For this reason, the choice of $\Delta t = 0.001$ seconds is maintained. Furthermore, there are no dashpots integrated at the mesh's bottom because the body waves dissipate almost entirely before they reach this boundary.

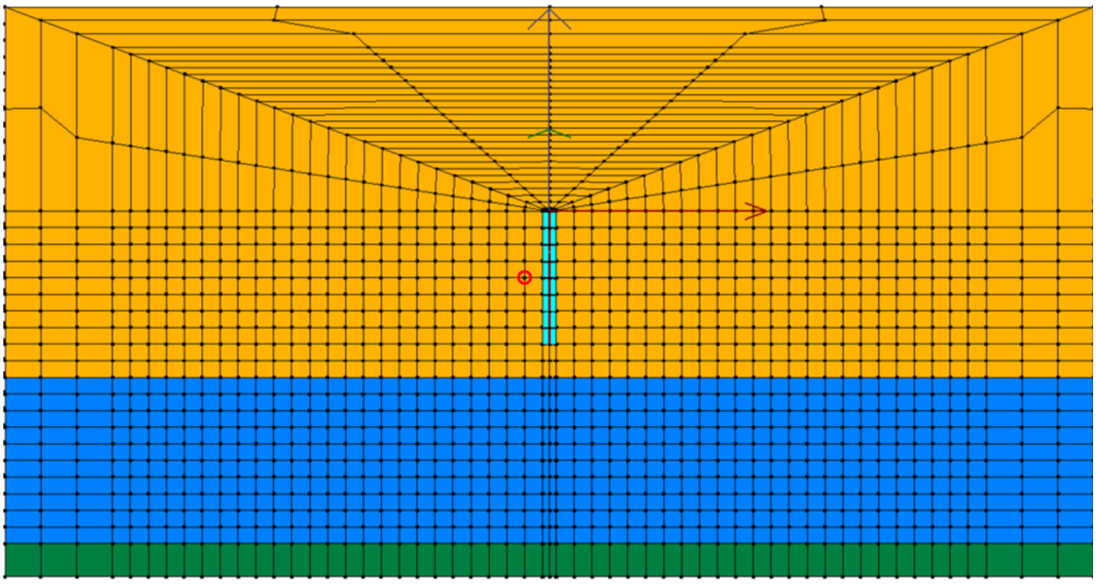

Figure 3.13: Location of the node which response is depicted in Figure 3.14 - illustrative mesh.

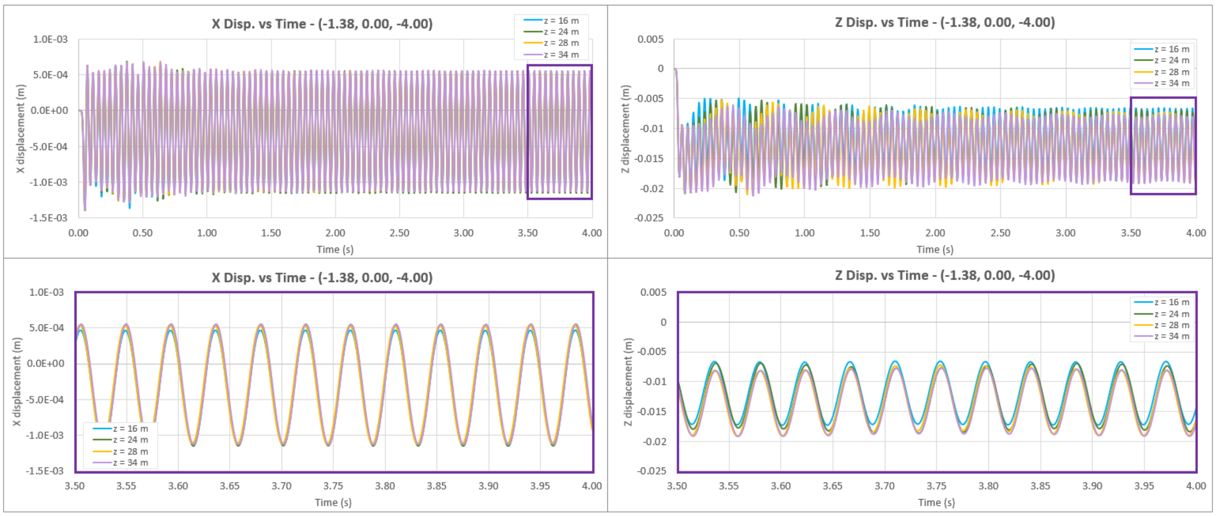

Figure 3.14: Example of the time response in terms of displacement for a node at the vicinity of the pile - different depths.

The same procedure is followed with the lateral distances. Some studies show that a lateral extent of 2 times the Rayleigh-wave length is enough to have accurate results in similar analyses (Schepers et al., n.d.). Nonetheless, in this study the value of this length, for simplicity approximated by the shear-wave length, is approximately 16 m, which in some tests showed not to be sufficiently wide. For this reason, five higher different extents: ± 24 m, ± 30 m, ± 36 m, and ± 40 m, with a Δt = 0.001 seconds and a depth of Z = 28 m, are tested. The results showed a better convergence starting at ± 30 m, even at the boundaries of the mesh. For this reason, a lateral mesh extent of X = ± 30 m and Y = 30 m is chosen, representing a distance of almost 45 times the diameter of the pile from the pile to the outer boundary. An example of the behaviour with this mesh is depicted in Figure 3.16.

Both the lateral and depth dimensions have been proven to produce minimal boundary effects through the assessment and visualization of responses along the mesh boundaries. The waves stemming from pile installation are largely dissipated before reaching these boundaries, ensuring that the simulation results remain almost unaffected by artificial reflections.

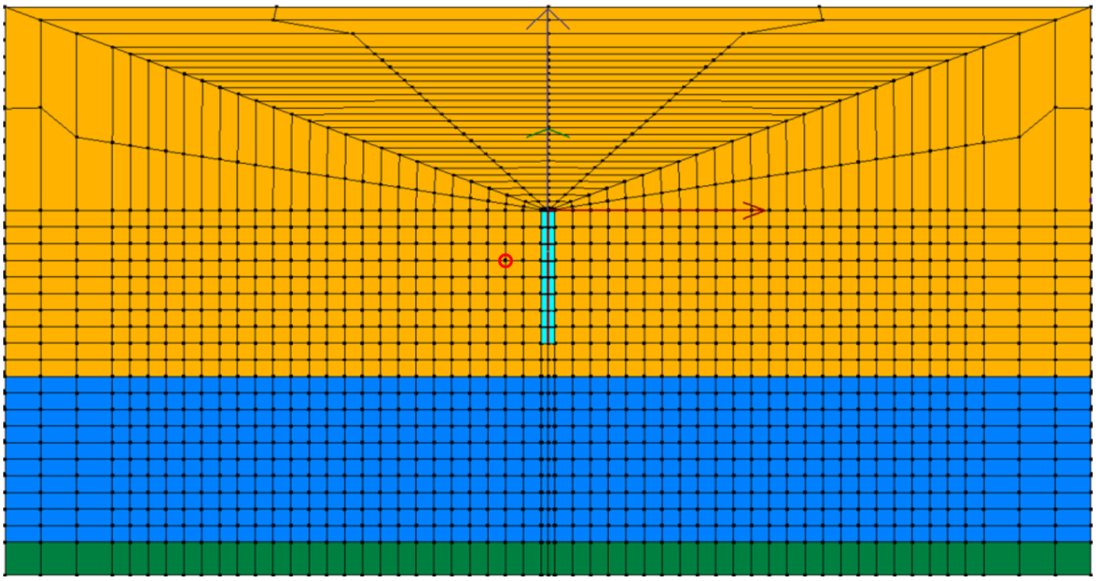

Figure 3.15: Location of the node which response is depicted in Figure 3.16 - illustrative mesh.

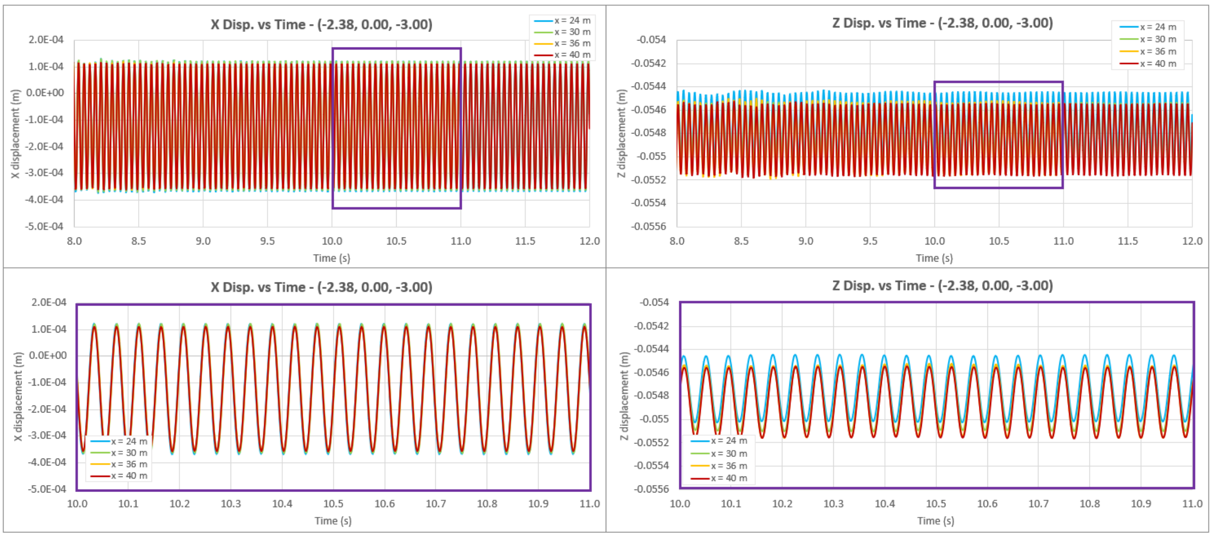

Figure 3.16: Example of the time response in terms of displacement for a node at the vicinity of the pile - different lateral extents.

In this phase of the sensitivity analysis, a trial was conducted to examine the soil's response following the gravitational stage, without any external loads. The primary objective was to confirm that the system is at rest before subjecting it to cyclic and complex excitations, devoid of any residual effects from the gravitational loading or any inherent self-induced disturbances. Furthermore, Fast Fourier Transforms (FFT) were generated for specific node responses to definitively ensure the absence of any external frequencies beyond the loading frequency being introduced into the system. Both observations were validated.

3.5.3 Mesh density

The starting step in determining the mesh size, or mesh density, involves adopting the approach put forth by Watanabe et al. (2017). This approach recommends maintaining at least eight to ten nodes per wavelength of the system in the vicinity of the pile for accuracy. As such, for this research, it is advisable to have an area around the monopile with elements of less than 1.0 meter in height and width. As moving further away from the pile, the element size has the potential to be enlarged. It is important to mention that mesh configurations with element sizes smaller than 0.5 are not evaluated due to the associated expensive computational constraints.

As previously mentioned, the waves' horizontal spread experiences the most significant impact. To address this concern, a mesh featuring elements with a fixed Δz close to the pile of 0.5 meters is chosen. For Δx, three different mesh configurations are tested. The first one involves Δx = 1 meter for distances up to 22 meters from the pile, and then a transition to Δx = 2 meters, referred to as *Mesh 1*. The second configuration starts with Δx = 0.5 meters up to 8 meters from the pile, followed by a transition to Δx = 1 meter up to 20 meters, and then a final transition to Δx = 2 meters, labeled as *Mesh 2*. Lastly, there's *Mesh 3*, which is non-uniform, featuring elements that widen as the distance from the pile increases, until it reaches 1 m elements and ends as *Mesh 2*. The rationale behind employing a coarser mesh density near the domain boundaries stems from the anticipation of minimal deformation occurring in those regions. The three tested meshes are illustrated in Figure 3.17 in two-dimensions for simplicity and clarity.

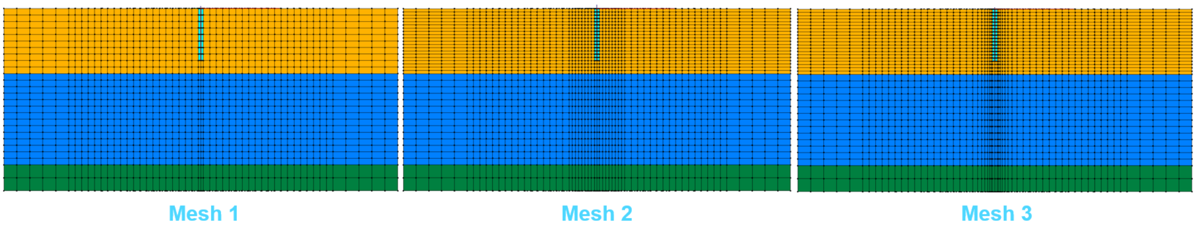

Figure 3.17: Tested meshes for mesh density evaluation and selection.

Since computational effort scales with both mesh density and time-step, the aim is to investigate the potential for utilizing a coarser mesh without sacrificing accuracy. It is evident that achieving an accurate depiction of the events around the pile post-installation, needed for the purpose of this project, requires an increased mesh density in the immediate vicinity of the pile. Upon analyzing the displacement response and stress-strain behaviour of the three distinct meshes, this becomes visible as *Mesh 1* did not represent the local pile-surrounding soil behaviour properly. For this reason, it is disregarded. The disparity in response between the other two examined meshes is relatively comparable, leading to the selection of *Mesh 3* due to its ability to yield results with reduced computational effort and time. It accurately depicts both local and global stress-strain behaviour.

The model resulted in a total of 9,170 nodes and 7,752 elements and, as depicted on the right-hand-side of Figure 3.17, in the lateral direction, the node-to-node distances expands with increasing distance from the pile. Specifically, the mesh resolution is finer in proximity to the pile and gradually becomes coarser towards the lateral boundaries. A summary of the outcomes from the sensitivity analysis is shown below, in Table 3.6, and the final mesh is illustrated in Figure 3.18. It is worth noting that the three colors in this image solely serve to distinguish between various element sizes in the Z-axis and do not signify distinct soil layers.

Table 3.6: Sensitivity Analysis summary

Time-step Δt	10^{-3} s
Domain size in X	60.74 m (±30.37 m)
Domain size in Y	30.37 m
Domain size in Z	28.00 m
Elements size Δx	Increasing with distance to the pile
	Smallest elements next to the pile: 0.15 m
Elements size Δz	0.5 m from 0 to 10 m depth
	1.0 m from 10 m to 24 m depth
	2.0 m from 24 m to 28 m depth

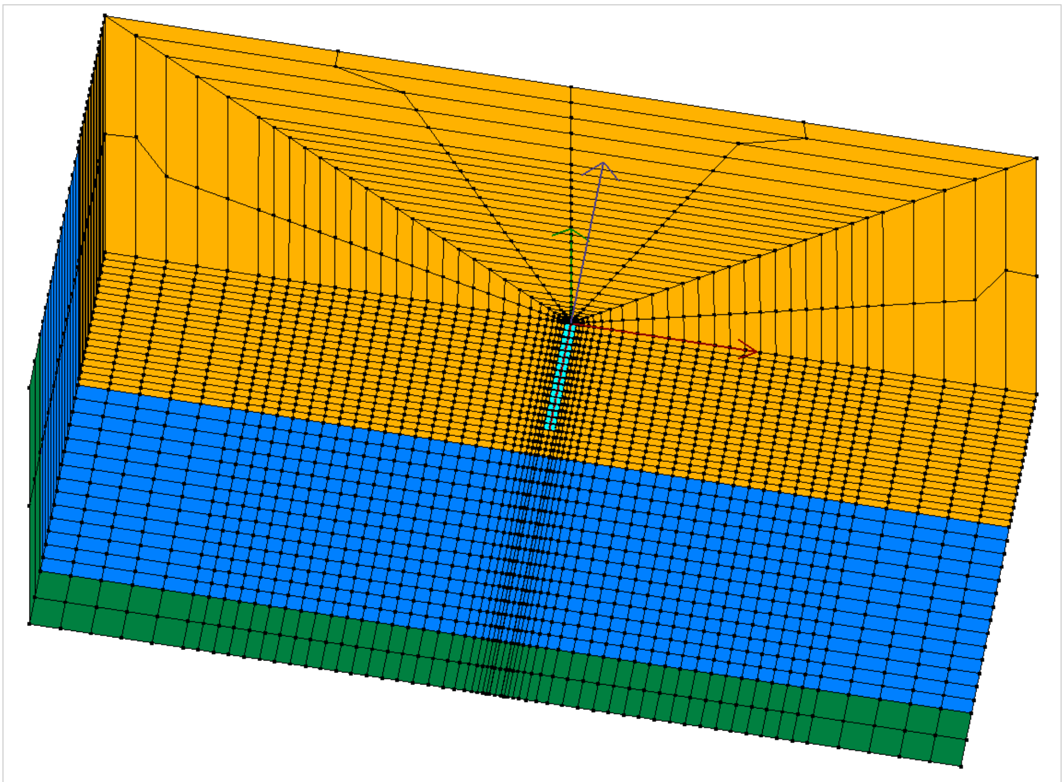

Figure 3.18: Final mesh selected based on the sensitivity analysis.

3.6 Reduced Final Model

Following the completion of the sensitivity analysis, the analyses started with the chosen mesh and the selected attributes outlined in Table 3.6. However, the installation procedure requires between 300 and 600 seconds, depending on the driving frequency. An estimate was made regarding the number of days required to model this duration using the refined mesh, and it exceeded 70 days under the most favorable circumstances. Due to the critical time constraint involved, a decision had to be taken to set aside a particular aspect of the mesh. This was done in such a way that it would not significantly compromise the precision and accuracy of the results, while also reducing the time required by at least half.

In the end, a smaller mesh is set (Figure 3.19), and only the installation loads and effects from the last 4 meters of the pile (from 4 to 8 m depth) are taken into account for the analyses, disregarding the first 4 meters (previously discussed in Section 2.5). It is worth noting that, as mentioned, the diverse colors in the Figure 3.19's mesh solely serve to distinguish between various element sizes in the Z-direction and do not act as a distinction for different soil layers.

Table 3.7: Mesh geometry and time-step for analyses

Time-step Δt	10^{-3} s
Domain size in X	48.74 m ($\pm$24.37 m)
Domain size in Y	24.37 m
Domain size in Z	24.00 m
Elements size Δx	Increasing with distance to the pile
	Smallest elements next to the pile: 0.2 m
Elements size Δz	0.5 m from 3 to 9 m depth
	1.0 m from 0 m to 3 m and from 9 m to 16 m depth
	2.0 m from 16 m to 24 m depth

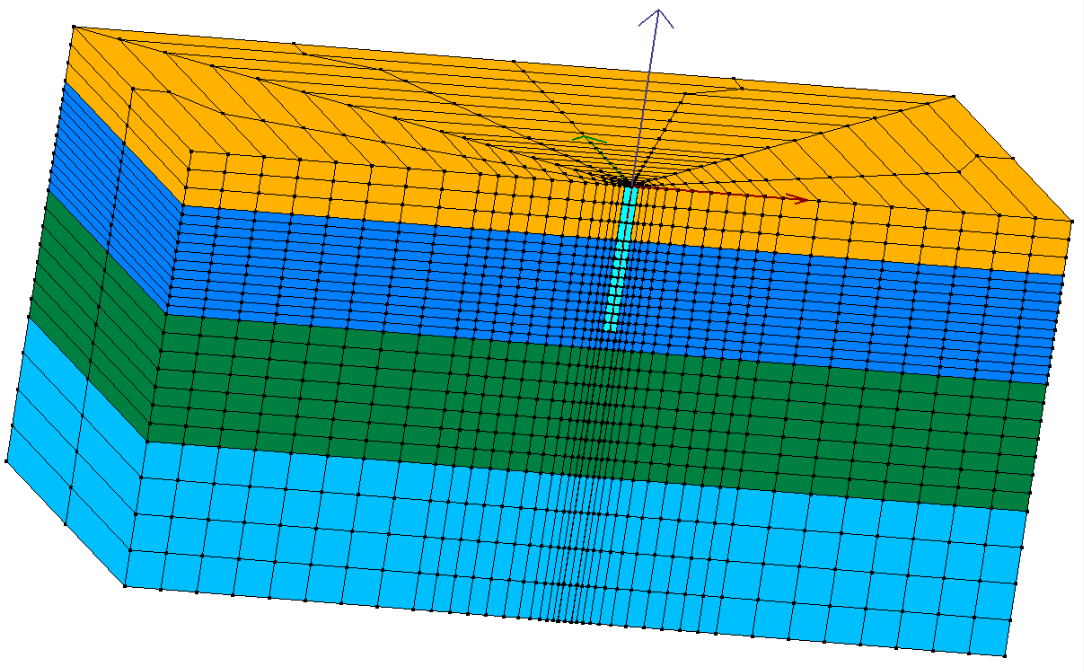

Figure 3.19: Reduced mesh selected to decrease the computation time.

As observed, the mesh dimensions have been adjusted, specifically reducing it by 12 meters along the X-axis (6 meters on each side of the pile), 6 meters along the Y-axis, and 4 meters along the Z-axis, in comparison to the mesh generated by the performance of the sensitivity analysis, discussed in Section 3.5. This decision to opt for a smaller domain rather than a coarser one is driven by the need for more detailed information and resolution in the immediate vicinity of the pile to observe the behaviour of the surrounding soil after installation and under lateral loads. As discussed by many authors, for example Schepers et al. (n.d.): "local mesh refinement in areas of strong stress or deformations gradients is strictly required". During the sensitivity analysis, altering the domain size within the ranges of X = $\pm$30 m and X = $\pm$24 m, or Z = 28 m and Z = 24 m, did not yield as significant an impact on the results as the transition from a coarser mesh (Mesh 1) to denser meshes (Mesh 2 and Mesh 3). The latter substantial change is visually depicted for a node close to the pile in Figure 3.20, but is similar to all the evaluated nodes in this area.

Moreover, the analysis focuses exclusively on the loads generated by installing the lower 4 meters of the monopile, which extends from a depth of 4 meters to 8 meters. This portion is considered the most crucial as it bears the majority of the loads and stresses. These loads are not only higher but also more critical in terms of stress and deformation during installation compared to those generated in the upper 4 meters. Additionally, they penetrate to greater depths, enabling the modelling of soil behaviour at actual, real depths.

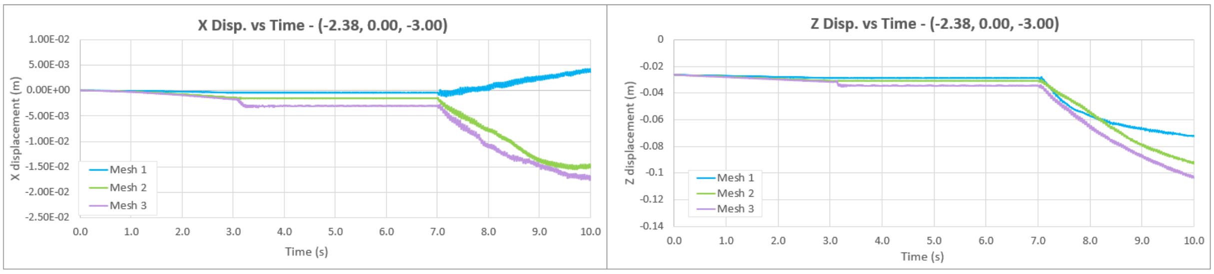

Figure 3.20: Example of the time response in terms of displacement for a node at the vicinity of the pile - Different mesh densities.

It is crucial to emphasize that both options, whether reducing the mesh geometry or element size, introduce errors into the simulation. However, the author deems the former option as the safest, based on the outcomes of the sensitivity analysis. Nevertheless, this adjustment to the model does result in a slight loss of accuracy, leading to the appearance of reflections. Nonetheless, these reflections are to some extent absorbed and attenuated by the dashpots or by the material damping. For all the reasons mentioned, the mesh depicted in Figure 3.19 and described in Table 3.6 is used for the analyses conducted in this research, comprising a total of 4,940 nodes and 4,100 elements and with a mesh resolution that is finer in proximity to the pile and gradually becomes coarser towards the lateral boundaries.

4 | Results and Discussion

Over the preceding chapters, the groundwork has been meticulously laid and the methodology followed is described. In this chapter, the outcomes and core findings that have emerged from this research are outlined, and a discussion is given. The following sections will present the results from the steps described in Chapter 2 using the model detailed in Chapter 3.

It is crucial to emphasize that the findings outlined in the subsequent sections are not entirely conclusive or fully representative of actual conditions. This is due to the simplifications required to execute the simulations with the available computational resources. These findings merely offer an initial insight into the potential behaviour of the soil under such conditions, indicating the necessity for future studies with more realistic features. These simplifications primarily include limiting the pile installation depth to only 4 meters (from 4 m to 8 m depth), instead of the entire pile; employing a simplified mesh; and applying a reduced number of lateral loading cycles.

4.1 Installation Process

During pile driving, the soil around and beneath the pile tip undergoes multiple loading cycles, resulting in the induction of shear stresses and strains into the soil. Furthermore, the vibration of the pile radiates body and surface waves in the soil directly beneath it, leading to its deformation. These loading mechanisms give rise to several soil-related phenomena addressed in this section. Such processes constitute a significant source of uncertainty in the analysis and design of pile foundations, as they are foreseen to impact the post-installation behaviour of such installed foundation.

As noted earlier, limitations in computational resources restrict the analyses to a single vibratory installation frequency (f = 30 Hz). Additionally, only the final 4 meters of the pile installation process are examined, for a pile with an 8 m embedment depth, as they are considered to be the most critical ones in terms of installation effects when compared to the shallower meters. Consequently, for a total driving time of 337 seconds, the last 4 m of driving lasted 288.5 seconds. Another aspect constrained by computational power is the view of the evolution of the installation process: although every time-step of the installation process is simulated and analyzed, only certain instants of the process can be displayed due to the extremely big size of the files, meaning that a sequence of the installation effects for each time-step cannot be depicted.

Figures 4.1 and 4.2 illustrate, respectively, the overall X and Z displacements, and the deformation magnitude of the soil/pile mesh subsequent to the completion of the installation process, before the lateral loading stage. Additionally, detailed depictions of the evolution of both horizontal and vertical displacements for specific nodes situated in close proximity to the pile during the vibro-installation process are presented in Figure 4.3. The deformation magnitude *d* from Figure 4.2 is defined as the square root of the sum of the squares of the displacements in X, Y, and Z, expressed as $d = \sqrt{U_x^2 + U_y^2 + U_z^2}$.

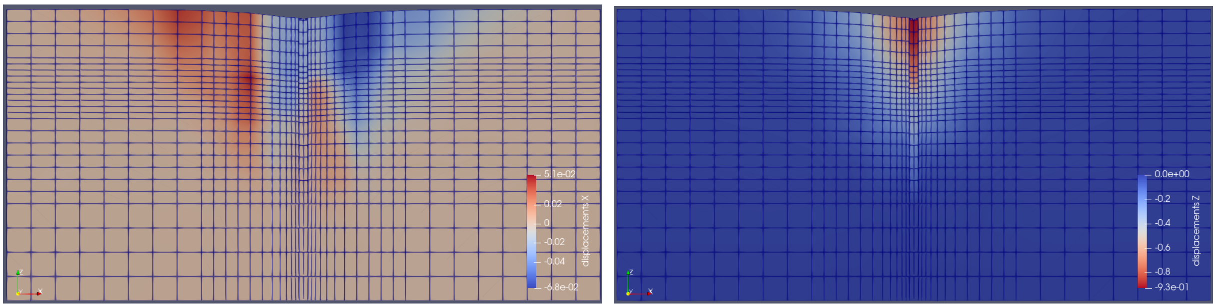

(a) Horizontal displacement X (m)

(b) Vertical displacement Z (m)

Figure 4.1: Total displacements produced in the soil mesh after the 30 Hz vibro-installation process.

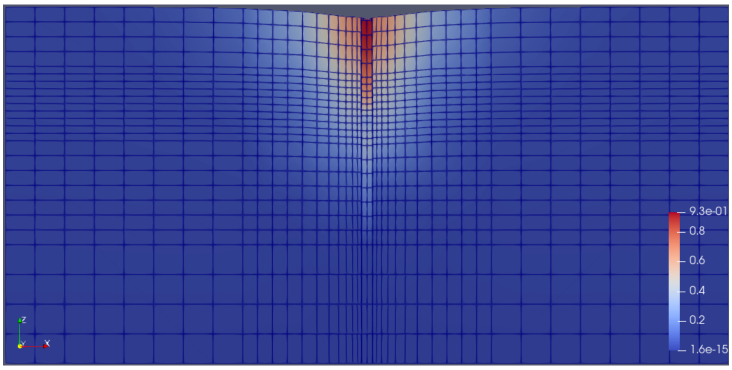

Figure 4.2: Total deformation magnitude in meters.

As observed both in the previous figures (Figures 4.1 and 4.2) and in Figure 4.3, during the pile driving process the soil is vertically and radially pushed out to allow the pile to penetrate. As anticipated, the main impact of vibratory driving is most pronounced in close proximity to the pile, gradually decreasing as the distance from it increases, and becoming negligible when such distance is sufficiently large, i.e. the mesh 'feels' the effects of the load up to 12 diameters away from the pile (1.5 wavelengths approximately), due to non-linearity and damping.

In what regards to the vertical displacement, it is observed that as the pile advanced, settlement of the soil around its shaft and close to the mudline occurred due to the rearrangement of the sandy soil and its densification. Nodes positioned beneath the pile tip underwent downward movement, attributed to the application of normal stresses induced by the pile and its vibratory loads. Every downward motion from the vibration cycles resulted in a subsequent vertical displacement of soil volume. Experimental findings conducted in dry, dense sand support this, revealing a significant rise in stress beneath the pile tip, producing substantial downward displacement of the soil in that area (Yang et al., 2010). Moreover, for nodes at sufficient depth, such as the assessed node at a depth of 16 meters and 2 diameters away (second-to-last plot on Figure 4.3), the vertical displacement was nearly negligible.

Conversely, the horizontal displacement diagrams (*X Disp vs Time* plots in Figure 4.3) illustrate an initial phase during the driving process, wherein the soil was pushed, leading to its outward lateral displacement, away from the pile. This phenomenon arises due to the induction of increasing stresses in the soil by the pile driving, primarily manifesting in the soil surrounding the pile and coming from the vibration waves originating due to installation. Nevertheless, a subsequent stage can be noted, in which the soil positioned slightly away from the pile and nearer to the surface shifted towards the pile after the initial outward motion (Figure 4.1a displaying darker red and blue shades on the left and right sides of the pile, respectively, indicating a shift towards the shaft of the pile). This movement may be attributed to changing volumetric tendencies in the soil.

The soil near the pile shaft may also experience localized dilation as a result of shearing forces generated by the pile's vibrations. This causes the soil to dilate, leading to an increase in the volume.

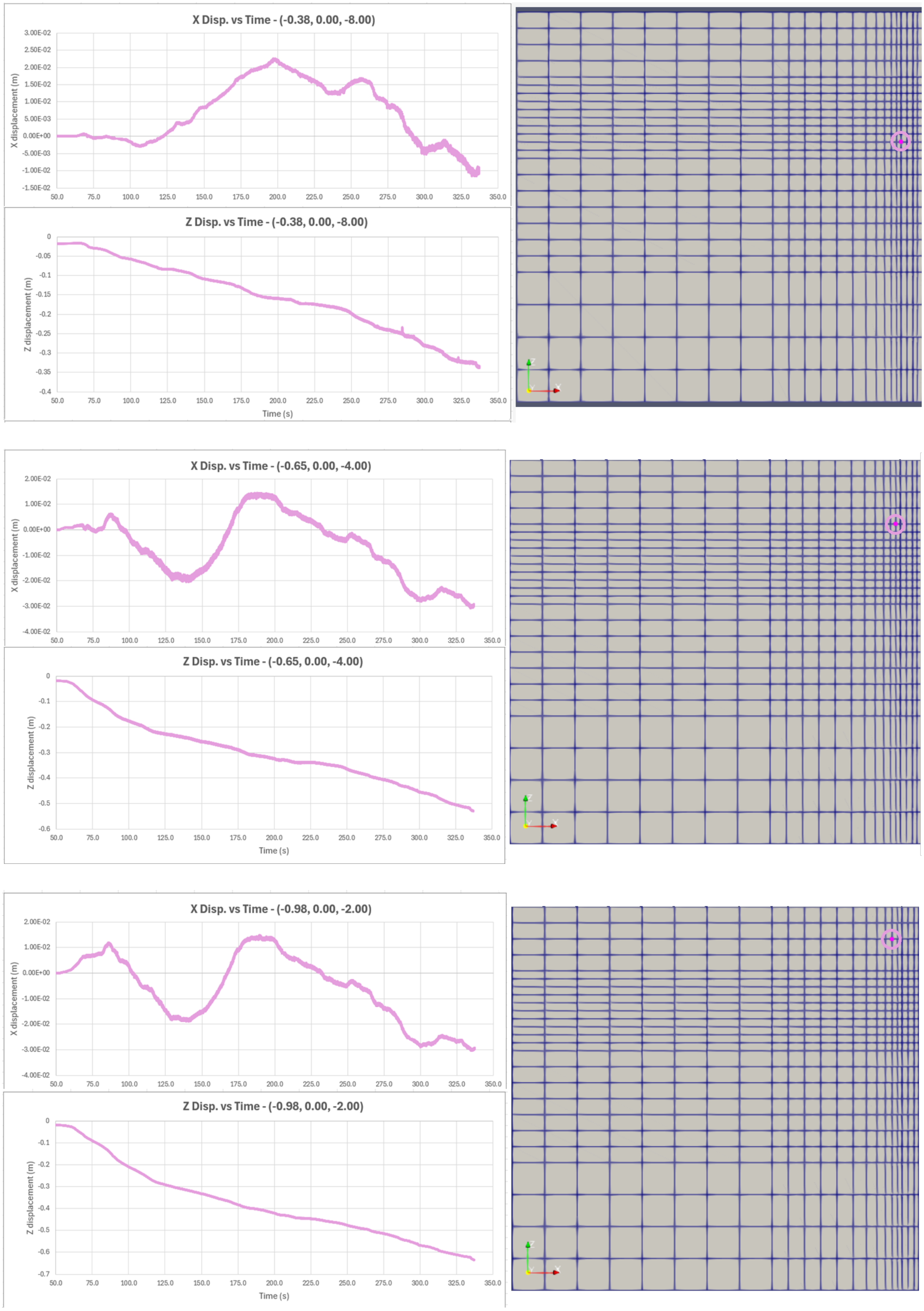

Figure 4.3: Displacements of nodes in the vicinity of the pile during the 30 Hz vibro-installation process

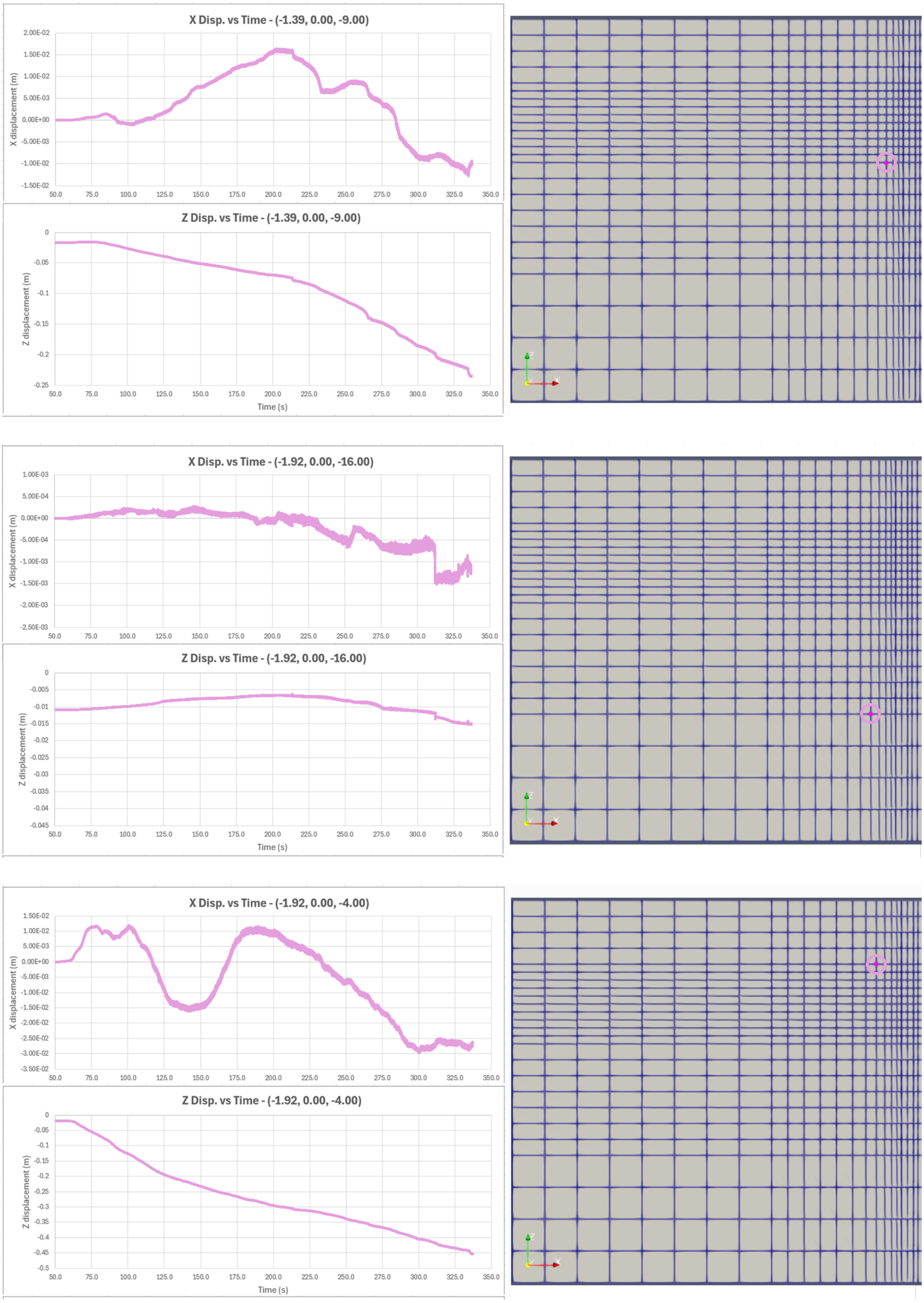

Figure 4.3: Displacements of nodes in the vicinity of the pile during the 30 Hz vibro-installation process

Moreover, Figure 4.4 depicts the distribution of the relative density of the evaluated soil following the vibratory installation process. Prior to installation, the soil's relative density was 0.8, uniform across the entire mesh.

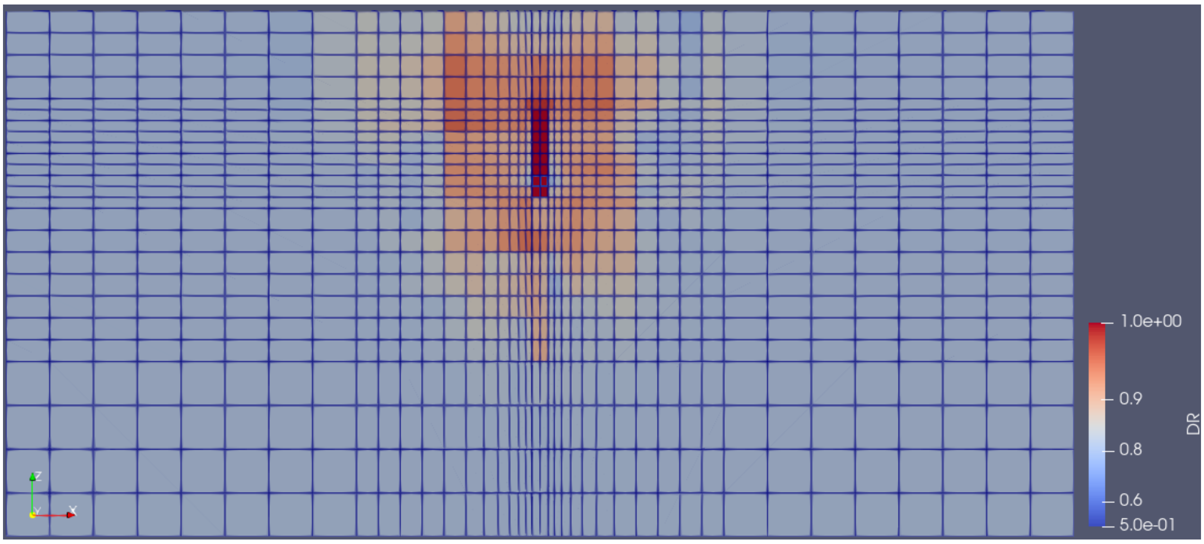

Figure 4.4: Relative density distribution after the vibro-installation process.

By the previous image, displaying the relative density distribution after the vibro-installation process is finalized, it is evidenced that when sandy soils are subjected to cyclic loading, i.e. to numerous vibration cycles, soil densification around the shaft occurs and, as the soil settles at the surface, a net densification is produced. During vibratory installation, the energy is applied to the pile and vibrations are transferred to the soil and start to travel within it. This reduces or modifies confining stresses and, therefore, the mean effective stress. These stress waves affect the soil matrix causing a shear-induced net densification, i.e. increasing the relative density of the soil (due to non-associated plasticity, this model simulates plastic volumetric strains induced by shear stresses). Nonetheless, such increase in relative density is typically more pronounced in loose or medium-dense soils compared to already dense soils. In initially dense soils, such as the investigated in the current study, the vibratory energy might not induce significant compaction, as the soil is already packed closely. However, a relative density of over 90% is noted in the vicinity of the pile's shaft after installation, signifying more than 10% increase compared to the soil's initial condition. This increase may lead to enhanced soil strength and friction along the sides of the pile, as the sand around the shaft is left in an overconsolidated state by the end of installation. In addition, the soil immediately at the interface pile-soil is loosening due to disturbance and due to the shearing effect of the vibro-installation, i.e. when a dense soil is sheared its void ratio may increase (relative density decreases).

Moreover, within the ongoing transmission of vibration loads into the soil, the wave amplitude diminishes as distance increases, due to the damping properties of the soil. In other words, the vibration amplitude decreases further away from the source (pile), as explained multiple times in the past sections, leading to a decrease in vibration amplitude. Consequently, the influence of vibratory pile installation on the relative density of the soil at a greater distance from the pile is typically less pronounced compared to its immediate surroundings. In this instance, as depicted in Figure 4.4, the increase in relative density observed close to the pile fades with distance from it, encountering values at approximately 10D closer to the initial 80% value before installation and soil is found to be left in an almost undisturbed state.

Furthermore, the soil beneath the pile tip undergoes significant compaction, resulting in the highest rise in relative density (with respect to the initial state) by the end of the vibratory installation process in this area. This is attributed to the substantial compressive axial stresses simulated during the installation process as the number of cycles applied increased, ultimately with the possibility of contributing to an increase in the base resistance. This is clearly observed in Figure 4.4. The soil inside the pile presents a high increase in relative density, due to the compaction caused by the vibration and driving force of the pile.

In the figure below, a more detailed examination of the relative density distribution surrounding the pile is depicted, with a scale factor of 2 applied to amplify the displacements, enhancing their visibility during this post-processing phase. In this figure, a heaving in the soil near the top surface of the pile, i.e. at a depth of 4 meters, is observed, due to the phenomenon of volumetric expansion in dense sands. Additionally, the looser state of the soil in the immediate vicinity of the pile becomes more evident and there is a clear interface in which the soil gets denser afterwards.

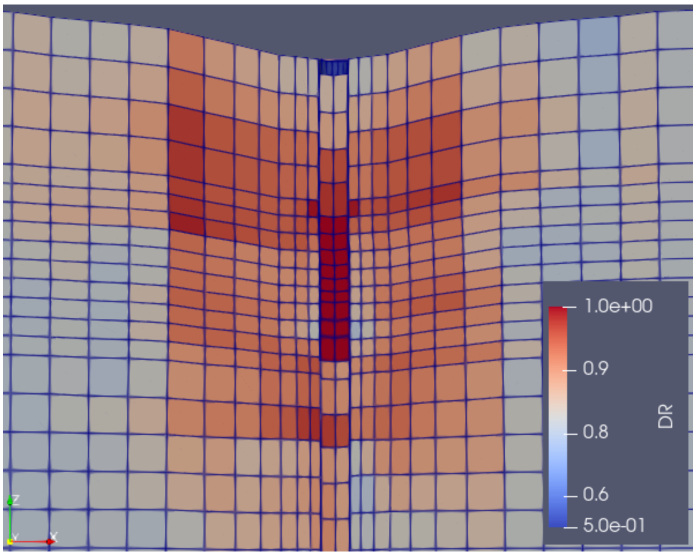

Figure 4.5: Relative density distribution after the vibro-installation, in the vicinity of the pile.

In Figure 4.6 the evolution of the relative density of a soil element located at 6 m depth and at the close vicinity of the pile is examined. It shows the increase in relative density and subsequent reduction as the pile tip is at different depths during vibro-installation.

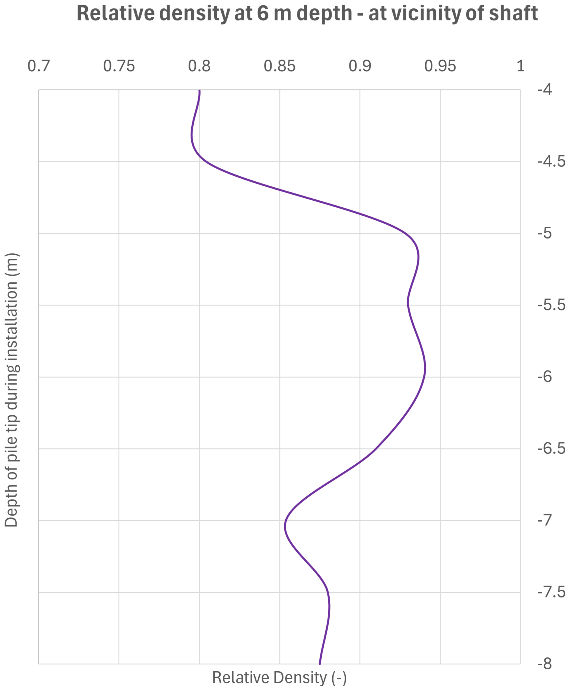

Figure 4.6: Evolution of relative density at a node located at 6 m depth while the pile tip passes different depths.

In addition, Figure 4.7 illustrates the change of the mean effective stress during the driving process. On the left, it displays the distribution before the installation and after the gravity loading stage, while on the right, it presents the distribution after the installation process.

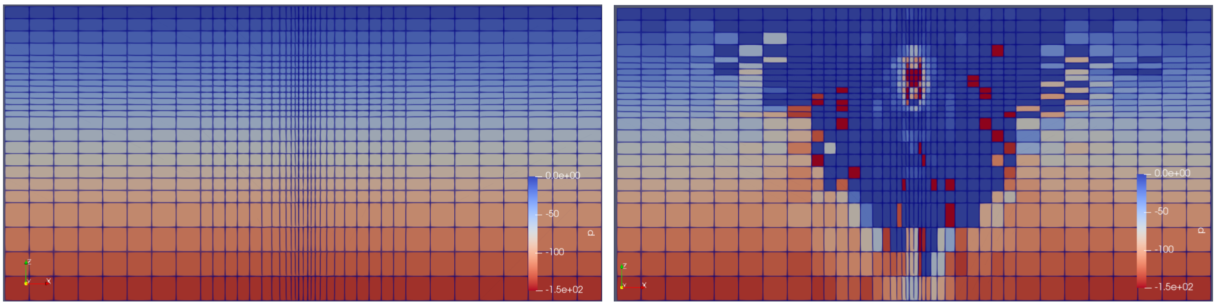

(a) p' before installation (b) p' after installation

Figure 4.7: Mean effective stress before and after the 30 Hz vibro-installation process.

As previously explained, when the sandy soil experiences the vibratory vertical movement induced by the vibro-installation of the pile, shear stresses and strains are transmitted laterally to the adjacent soil. In parallel, normal stresses are induced beneath the pile tip. As the number of applied cycles increases, a densification of the soil and, hence, high stresses, are produced in the latter region, as expected and as observed in Figure 4.7. This combined effect of increased stress, along with the increase in relative density discussed in the previous section, contributes to enhancing the strength of the sandy soil.

While stress amplifies beneath the tip and directly at the immediate shaft-soil interface, a decrease is observed along the shaft, depicted in the figure below (Figure 4.8), with a more detailed examination of the mean stress surrounding the pile, and an applied scale factor of 3 to amplify the displacements. Due to the installation process and its induced cyclic shearing, the radial stress acting on the vicinity of the shaft decreases as the number of cycles increases, which is related to the densification of the soil in that area. Moreover, even though it is slightly shown at depths of 4 and 5 meters in Figure 4.8, if installations beyond 4 meters would have been feasible for assessment, a more pronounced decrease in lateral stresses might have been expected at shallower depths. This stems from the fact that sand positioned under the model pile, after experiencing an intense axial compression, is displaced laterally by the advancing tip and undergoes radial stress reductions as the pile shoulder passes.

The drop of p' supports the net densification that was previously explained and depicted in Figure 4.4. Lastly and in general, the installation influence becomes negligible at a sufficiently large distance from the pile (Figure 4.7).

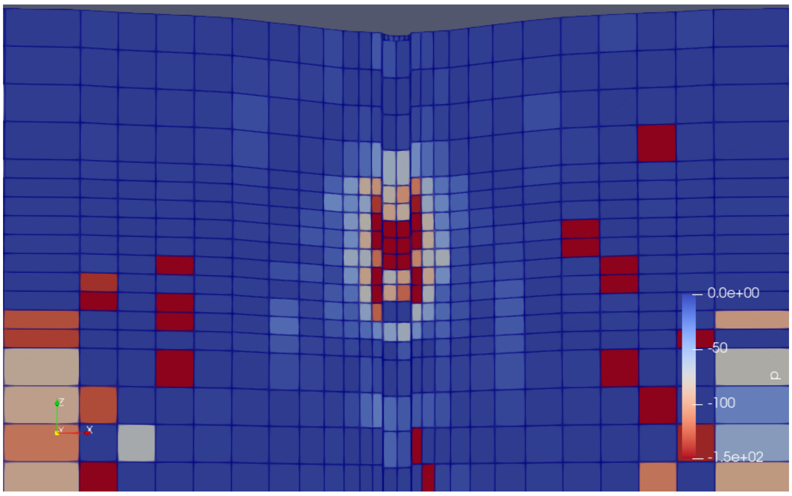

Figure 4.8: Mean effective stress distribution after the vibro-installation process in the vicinity of the pile, with magnified displacements.

The installation of vibratory piles leads to significant changes in the final characteristics and conditions of the sandy soil. Previous observations highlight marked differences in stress levels and void ratios compared to the soil's initial state before installation: there is both an accumulation of horizontal stress and densification of the soil within and surrounding the pile. This dual impact results in an increased soil strength in the vicinity of the pile.

4.2 Lateral Loading

Following the installation phase, the impact of pile installation on the subsequent lateral loading response of piles is evaluated. This involves modelling and applying the subsequent loads from the offshore environment to the system, corresponding to the 10-cycle load in the positive X-direction outlined in Section 2.6 of this report. The reaction of piles to these operational loads is expected to be influenced by the installation process and its effects: the contrasts between the initial in-situ soil conditions and those after installation are assumed to directly affect the lateral pile behaviour. Therefore, considering the effects of installation is crucial for ensuring an accurate prediction of this lateral response, as neglecting these effects is likely to lead to an inaccurate prediction of this response.

In order to incorporate the impact of pile installation, it is necessary to consider the soil conditions after installation prior to the modelling of the subsequent lateral loading. Thus, the soil's post-vibro-installation state, in terms of relative density, stress-strain distribution, and other state-dependent variables, serves as the initial soil conditions for the lateral loading analysis.

Figure 4.9 depicts the lateral displacement increment of the pile, generated during the 10-cycle load simulating the offshore environment, of both the wished-in-place pile (left) and the vibro-installed pile (right). As expected, the effects of the cyclic loads are mostly concentrated in shallower areas, above the point of rotation of the pile.

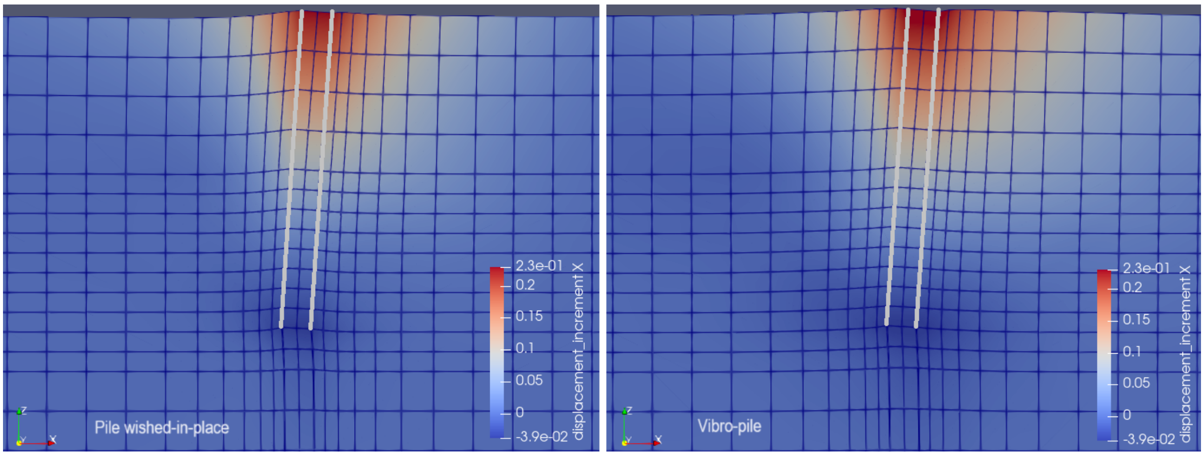

Figure 4.9: Soil horizontal displacement increment after the lateral loading stage (10 loading cycles), with a deformation scale factor of 2.

In Figure 4.9, it is observed that at the conclusion of the ten cycles, there is a larger and more pronounced displacement field on both sides of the pile in the simulation where installation loads are considered, i.e. when the pile installation was modelled and where the changes in soil state induced by installation are taken into account, as opposed to the scenario where the pile is considered as wished-in-place. This is translated into an increased pile rotation in the former case, which might be attributed to the disturbance of the shallower soil located close to the pile during its installation.

Similarly, at deeper levels near the tip of the pile, larger horizontal displacements occur in the vibro-installed pile case in the opposite direction of the applied loads, when compared to the wished-in-place base scenario, i.e. in the latter, the impact of these displacements on the soil mesh is confined primarily to the pile tip. Conversely, in the former case, this impact extends over a significantly broader area. These lateral displacements stem from the reaction of the rotation of the pile head in one direction, producing a counteracting force in the opposite direction.

Additionally, the simulations predict heaving of the soil around the pile at the ground surface, indicating a slightly stronger impact of such heave in the scenario where the installation process is not taken into account.

The information detailed earlier is also depicted in the subsequent figures, namely Figure 4.10, Figure 4.11, and Figure 4.12. These figures illustrate the horizontal displacement of the pile head resulting from the force applied during the lateral loading stage and over the time of the application of such load, and the cumulative displacements occurring with each cycle of lateral loading, respectively. Notably, it should be emphasized that the initial monotonic push and its consequent displacement are not accounted for in the plots. For this reason, a separate plot for the displacement produced in both cases with only the initial monotonic force (before the cycles are applied) is generated and shown in Figure 4.13.

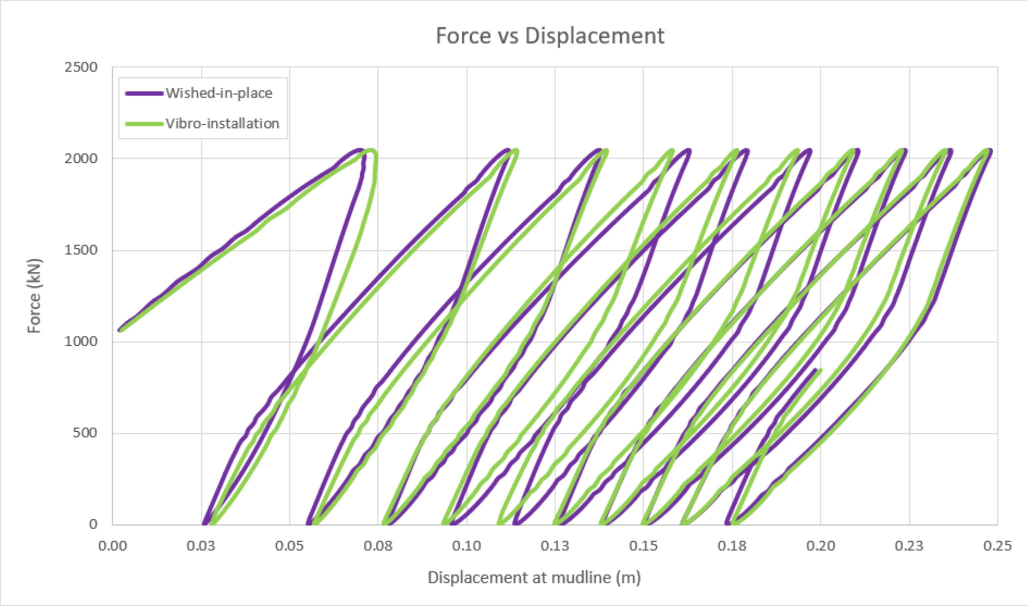

Figure 4.10: Horizontal displacement of the pile head produced by the force applied during lateral loading.

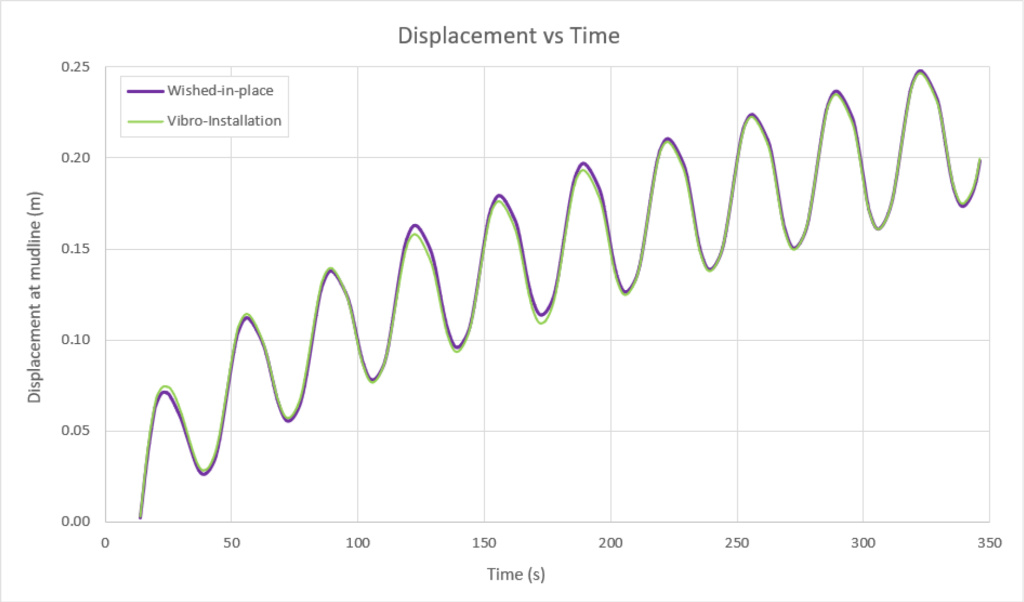

Figure 4.11: Horizontal displacement of the pile head over the time of the application of the lateral load.

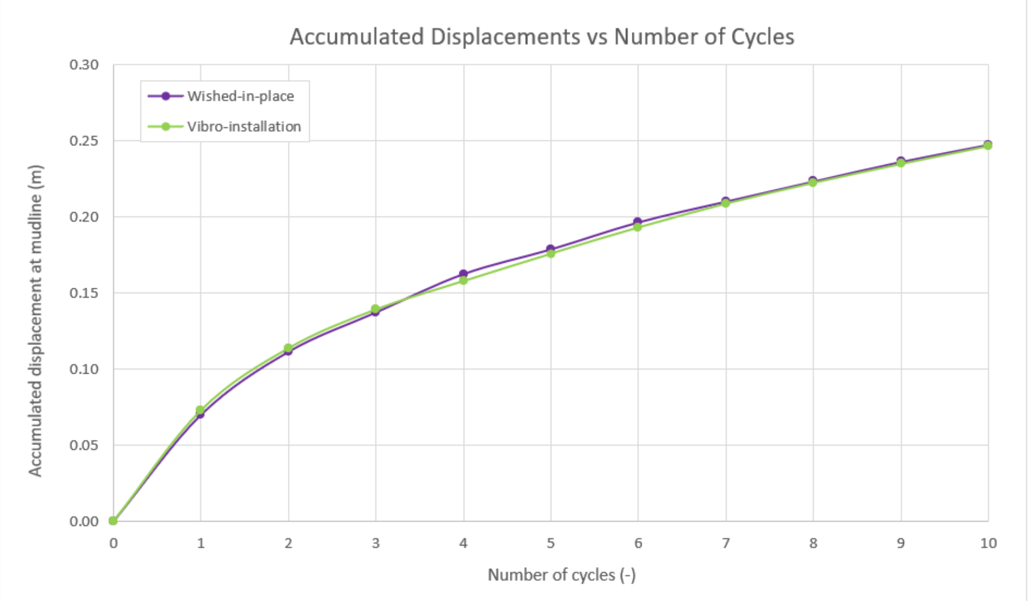

Figure 4.12: Overall view of the accumulated displacements with each of the lateral loading cycles.

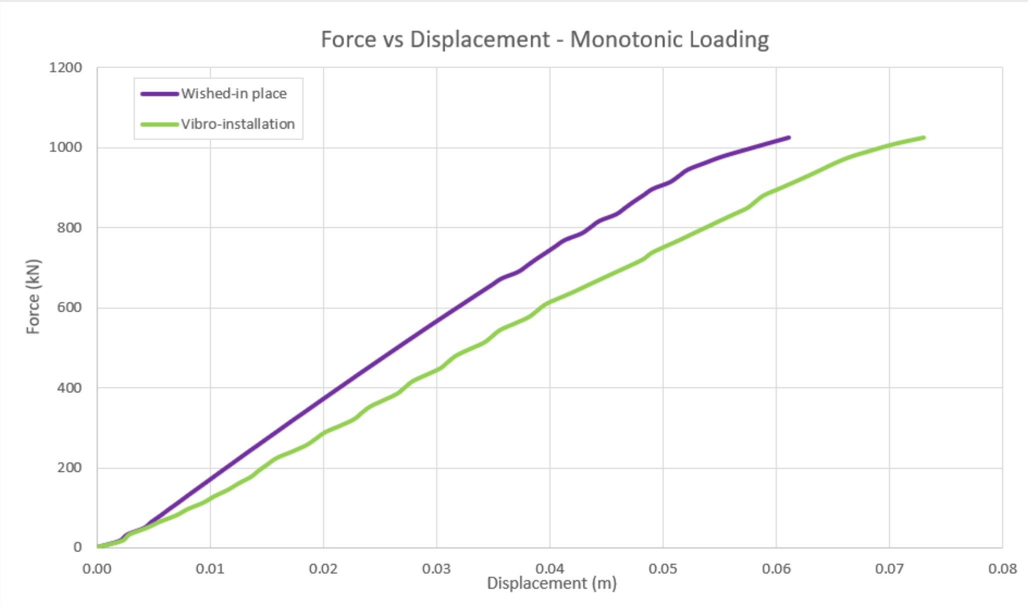

Figure 4.13: Displacements produced during the previous monotonic load stage.

As noted in Figure 4.10 during the initial lateral loading cycles, the vibro-installed pile exhibits greater displacement in response to the applied force than the wished-in-place pile, which coincides with the displacements produced by the first monotonic push, before the cyclic loading start (Figure 4.13). However, starting from before the fourth cycle onward, the situation reverses, with the soil at the mudline experiencing greater strains in the wished-in-place (WIP) scenario. This trend is illustrated in Figure 4.14, which provides a detailed view of the cumulative displacements. Specifically, the middle plot indicates the moment at which the simulation incorporating installation loads begins to accumulate fewer displacements per cycle compared to its WIP counterpart. The last cycles exhibit quite comparable responses and displacements, suggesting that, over time and with ongoing cyclic loading, the impacts and the influence of the installation may decrease and become less significant and, consequently, less relevant when studying the behaviour of the soil. Nonetheless, the only conclusion that can be drawn by this image is that, for N = 10 cycles, the cyclic behaviour is the same for both cases.

Furthermore, despite the vibro-installed pile exhibiting a softer initial response, the initial soil stiffness at the mudline is comparable in both scenarios, albeit naturally higher for the WIP pile. Additionally, as expected, the soil shows slow permanent displacement rates that increase systematically with each applied loading and unloading cycles for both scenarios.

During the 10 cycles of the lateral loading applied at the mudline, it is also possible to observe common features of dry sands subjected to cyclic lateral loads, such as the stiffness showing a gradual increase with the number of cycles. The latter, along with the densification of the soil with each cycle, is proven by each load-cycle producing less displacement increments than the previous cycles.

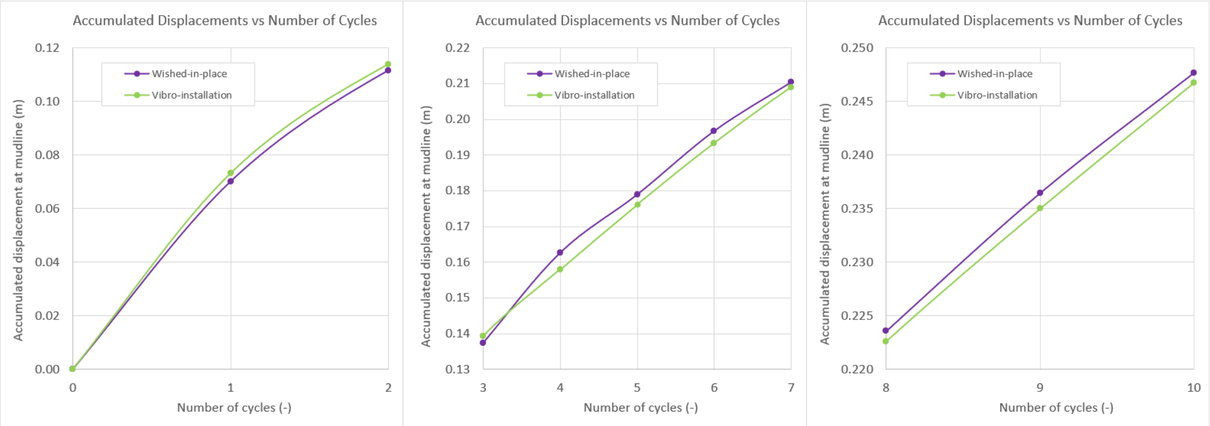

Figure 4.14: Closer view of the accumulated displacements with each of the lateral loading cycles.

The images below illustrate the distribution of the relative density in the soil following the lateral loading stage, depicting both the vibro-installation scenario (Figures 4.15 and 4.16) and the wished-in-place basis scenario (Figures 4.17 and 4.18). The displacement of the pile is represented with a scale factor of 2.

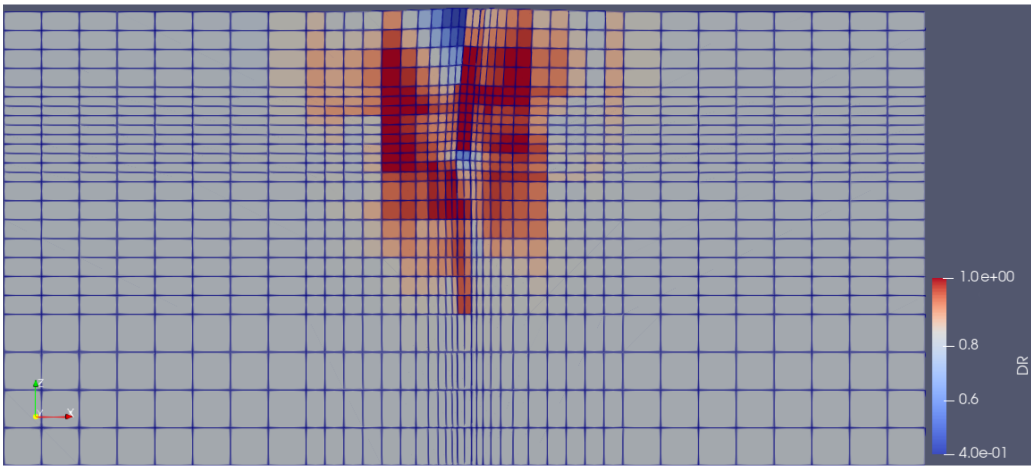

Figure 4.15: Relative density distribution after lateral loading - Pile installed using the vibro-installation method.

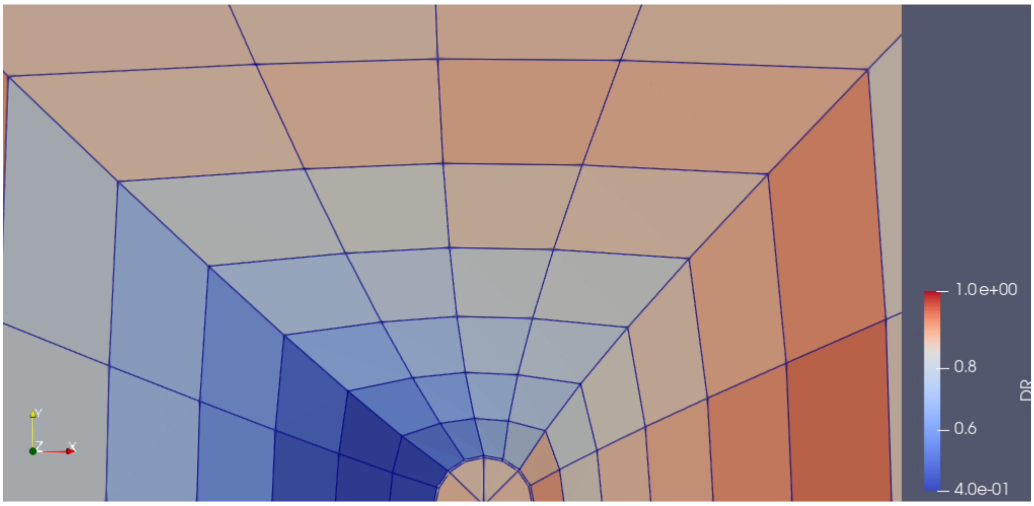

Figure 4.16: Plane view of the relative density distribution at the pile head after lateral loading - Pile installed using the vibro-installation method.

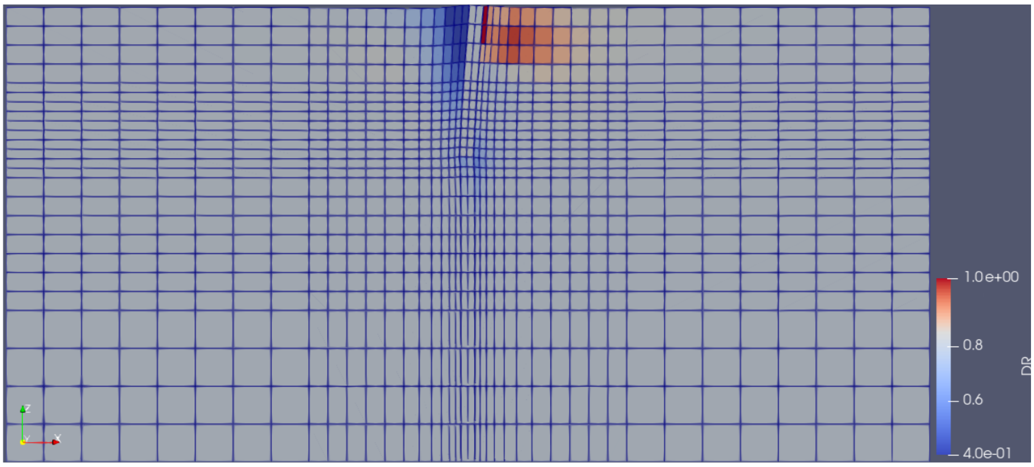

Figure 4.17: Relative density distribution after lateral loading - Pile wished-in-place.

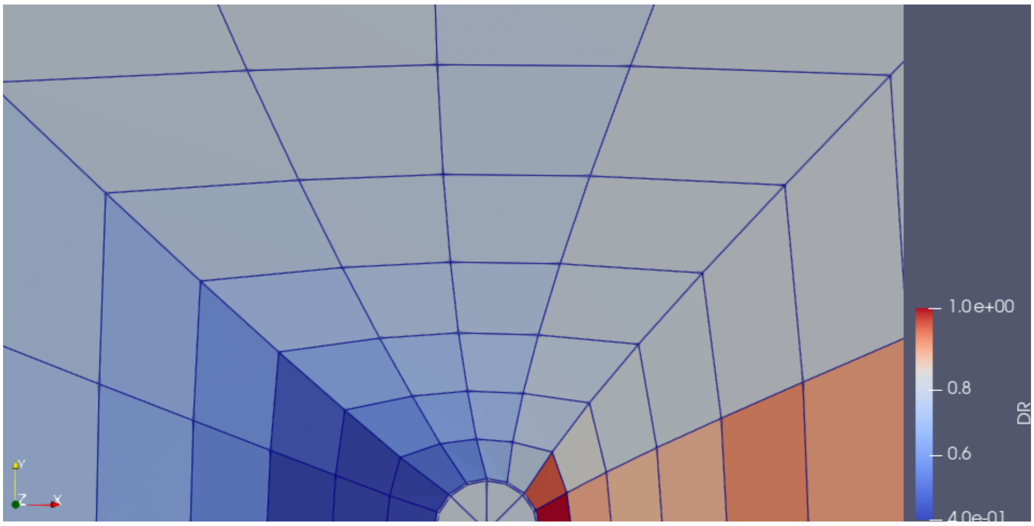

Figure 4.18: Plane view of the relative density distribution at the pile head after lateral loading - Pile wished-in-place.

The preceding figures illustrate the prediction of a strong decrease in the soil's relative density to the left of the pile, for both the vibro-pile and the wished-in-place pile. This phenomenon occur because lateral loading induces shear stresses in the soil adjacent to the pile, potentially leading to loosening of the soil (increasing of void ratio) on the opposite side to the direction of loading. Moreover, there is evidence of localized soil densification on the right side of both piles, due to repeated loading and unloading cycles, enhancing their lateral load-bearing capacity in that particular direction. This is more pronounced in the WIP pile.

When comparing both cases in terms of relative density changes during the cyclic lateral loading stage, it is clear that the already disturbed soil from the installation process becomes even more disturbed during this loading phase, especially in shallower areas. This makes sense, as in this case the soil has undergone plastic deformation, due to the vibrations, and has already experienced strain beyond its yield point, which means that it may require less additional stress to induce further plastic deformation. It is important to note that if the simulation had encompassed the full 8-meter depth of the pile installation, it could have likely resulted in soil densification around the shaft along its entire length and not only in the last 4 meters. Such densification might have had an impact on lateral loading outcomes, potentially constraining the pile's lateral displacement in the simulation where vibro-installation effects are accounted for, as the compacted zone may have provided additional horizontal support for the pile. Consequently, the WIP scenario could have exhibited increased displacements when both cases are compared.

Conversely, significantly higher relative density values are observed near the pile tip and inside the pile in the simulation where the vibratory installation method is employed. This zone holds less significance in simulations where installation is not modelled. Additionally, as the pile rotates under the lateral loading cycles, the soil to the right of the pile tip experiences a reduction in relative density in both cases.

In summary, when comparing the relative density results of both piles, i.e. the WIP pile and the vibro-pile, it becomes evident that the local densification, induced by the lateral loading cycles, contributes to the stiffness increase noted earlier. Additionally, the soil disturbance caused by installation loads primarily explains why this scenario exhibits greater displacements during the initial cycles compared to the WIP scenario.

5 | Final Conclusions

5.1 Final Conclusions

The present study advocates for the broader adoption of vibratory pile driving in offshore wind farm developments, considering its potential for reducing environmental impacts and enhancing pile performance. It employs a numerical approach to explore how vibratory pile driving impacts the lateral behaviour of monopiles in offshore settings. Through the utilization of a 3D Finite Element model and the integration of the Manzari-Dafalias constitutive model for dry sand, it uncovers some insights into the alterations in soil characteristics induced by the installation process, which underscores the importance of accounting for the effects of such process when predicting the performance of monopile foundations under lateral loads, an aspect that is currently under-explored in the literature.

The installation effects were considered by merging two models. The output loads produced in the pile-soil interface from a model that simulates the vibratory installation process are used as an input in a 3D finite-element model that reproduces the non-linear cyclic soil behaviour on a long-term, when the pile is subjected to lateral loads. In this context, a comparison can be drawn to a scenario in which no installation loads are taken into account.

The research highlights the dynamic soil behaviour during vibratory pile driving, emphasizing the vertical and lateral displacements of the foundation soil, contributing to changes in soil density and stress distribution around the pile shaft and tip: soil densification (increase in relative density) occurs at the vicinity of the pile due to the application of the vibrations, leading to an enhancement of the soil's bearing capacity in the area and, hence, of the pile lateral stability. This effect, producing an increase in relative density of up to 10% in the tested dense sands, would have probably been more notorious in initially loose or medium-dense sands.

Additionally, the compaction of soil beneath the pile tip is significant during vibro-installation, resulting in a notable increase in relative density and enhanced soil strength. Conversely, soil loosening occurs in areas located exactly at the immediate vicinity of the shaft of the pile, leading to a decrease in relative density.

The effects of pile installation are shown to influence mildly the subsequent response of the examined pile to lateral loading. Displacement fields during lateral loading simulations show differences between piles installed with vibratory methods and those considered wished-in-place (WIP). According to the results, vibratory-installed piles exhibit greater initial displacements under lateral loading due to soil disturbance during installation. However, the influence of installation diminishes with continued loading cycles. Moreover, the densification induced by lateral loading cycles contributes to increasing soil stiffness, affecting the lateral displacement response of the monopile.

Overall, the findings emphasize the complexity of soil dynamics and the necessity of accounting for installation effects in pile foundation design and analysis. Understanding the mechanisms driving soil displacement and densification during both installation and operational loading stages is crucial. Future studies should further investigate the long-term effects of pile installation on soil behaviour and the subsequent response to various loading conditions, considering a broader range of parameters and realistic soil and loading conditions.

5.2 Limitations and Future Research

Considering the beneficial outcomes associated to vibratory installation, it is recommended to give greater attention to employing this technique for offshore wind monopiles. Therefore, and acknowledging the study's scope limitations, such as the focus on dry sand and a simplified mesh, there is a clear pathway for future investigations to address the specific constraints that were not reached by this research.

Firstly, pile-soil interface elements are not used in the simulations on this research. Since the behaviour at the interface is critical in transferring loads between the pile and the soil, neglecting this interface can lead to significant inaccuracies in the analysis and, hence, hinder the reliability of the results. If further investigation is performed it is advised to include such elements.

In this research, a vibratory-installed pile is compared, using numerical procedures, with a wished-in-place pile. It is advised that future research directly compares the post-vibro-installation lateral behaviour of sandy soils with that of the most commonly used impact driving method, maintaining consistent parameters. If the results favour the vibratory method, it could lead to wider acceptance and implementation of this approach.

On a related note, this research employs the Manzari-Dafalias constitutive model. However, it would be beneficial to perform simulations using different constitutive models for sands to evaluate and analyze the influence this critical modeling aspect has on the results. For instance, the SANISAND model cannot simulate grain crushing, which is relevant during pile driving. Understanding the effects of this limitation on the results would be insightful. Additionally, investigating alternative constitutive models for testing clayey soils could also be valuable.

Furthermore, the study's focus on dry sand restricts its applicability to offshore environments where saturated conditions prevail. The absence of excess pore pressure generation in the simulations overlooks a crucial aspect influencing both installation and lateral responses in real offshore conditions and hinders a comprehensive understanding of pile response across diverse environmental settings, underscoring the necessity for further exploration of coupled processes in future investigations (further aspects on this regard are previously detailed in Section 3.2.2).

Moreover, the study's focus on a limited portion of the pile due to computational constraints, rather than its entirety, may hinder the reliability of the results, as it is a non-realistic scenario and represents a gap in the objectives of this investigation. On the same note, the fact that the optimal mesh size, obtained after a thorough sensitivity analysis, needed to be re-sized due to computational constraints may also have had an influence in the outcomes presented in the previous sections. In general, with increased computational resources, there arises an opportunity not only to simulate the entire length of the pile installation but also to delve deeper into other aspects. For instance, it could be interesting to explore the number of lateral load cycles and the necessary load amplitude required for mitigating the impact of the installation process. Additionally, exploring various vibro-installation frequencies and settings, or even different pile sizes, is pertinent as they directly influence soil behaviour during driving and its subsequent response.

Finally, it is acknowledged that the initial relative density of the sands being tested strongly influences the subsequent effects of the installation process. Therefore, it is advisable to conduct tests across a wider range of initial soil densities to gain a more thorough insight into soil behaviour under diverse conditions. For instance, loose and moderately dense sands may exhibit greater deformations compared to the densely packed sands in the tests, having a stronger impact during the lateral loading stage.

In conclusion, while this study contributes valuable insights into the behaviour of piles in dry sand conditions, its limitations underscore the necessity for future research endeavors to address these constraints and broaden its scope. Constraints related to computational resources emerged as the main research limitation, particularly concerning the capacity to execute a comprehensive analysis encompassing a broader range of scenarios. The need for additional computational power to accommodate more extensive simulations and diverse case studies is evident.

6 | References

Achenbach, J. (1973). *Wave Propagation in Elastic Solids - North-Holland Series in Applied Mathematics and Mechanics*. Elsevier B.V.

Akram, S., & ul Ann, Q. (2015). Newton Raphson Method. *International Journal of Scientific & Engineering Research*, *6*(7), 1748–1752.

al-Omari, R., Fattah, M., & Kallawi, A. (2017). Stress transfer from pile group in saturated and unsaturated soil using theoretical and experimental approaches. *MATEC Web Conference*, *120*(art. ID 06005), 1–12. https://doi.org/10.1051/matecconf/201712006005

Been, K., & Jefferies, M. G. (1985). A state parameter for sands. *Géotechnique*, *35*(2), 99–112.

BNEF. (2018). 2017 Offshore Wind Market Outlook. *Bloomberg New Energy Finance, NY, USA - Retrieved from: https://about.bnef.com/blog/global-offshore-wind-market-set-to-grow-sixfold-by-2030/*.

Bosscher, P. J., Menclova, E., Russel, J. S., & Wahl, R. E. (1998). Estimating Bearing Capacity of Piles Installed with Vibratory Drivers. *US Army Corps of Engineers, Washington, DC, USA*.

Casagrande, A. (1936). Characteristics of cohesionless soils affecting the stability of slopes and earthfills. *Journal of the Boston Society of Civil Engineers*, 257–275.

Chopra, A. K. (1995). *Dynamics of Structures - Theory and Applications to Earthquake Engineering* (Vol. 3). New Jersey: Prentice-Hall, Inc.

Ekanayake, S., Liyanapathirana, D., & Leo, C. (2013). Influence zone around a closed-ended pile during vibratory driving. *Soil Dynamics and Earthquake Engineering*, *53*, 26–36. https://doi.org/10.1016/j.soildyn.2013.06.005

European Offshore Wind Farms Map Public. (2023). *WindEurope: Brussels, Belgium*.

Feng, Z., & Deschamps, R. J. (2000). A Study of the Factors Influencing the Penetration and Capacity of Vibratory Driven Piles. *Soils and Foundations*, *40*(3), 43–54. https://doi.org/10.3208/sandf.40.3_43

Haiderali, A., Nakashima, M., & Madabhushi, G. (2015). Cyclic lateral loading of monopiles for offshore wind turbines. *Proceedings of the 3rd International Symposium on Frontiers in Offshore Geotechnics (ISFOG)*, 711–716. https://doi.org/10.1201/b18442-97

Hilber, H. M., Hughes, T. J. R., & Taylor, R. L. (1977). Improved numerical dissipation for time integration algorithms in structural dynamics. *Earthquake Engineering and Structural Dynamics*, *5*, 283–292.

Holeyman, A. E. (2002). Soil Behavior under Vibratory Driving.

Hughes, T. J. R., & Hilber, H. M. (1978). Collocation, dissipation and overshoot for time integration schemes in structural dynamics. *Earthquake Engineering and Structural Dynamics*, *6*, 99–117.

Hughes, T. J. R. (1987). *The Finite Element Method: Linear Static and Dynamic Finite Element Analysis*. New Jersey: Prentice-Hall, Inc. pp. 1-48.

Jamiolkowski, M., Presti, D. L., & Manassero, M. (2003). Evaluation of Relative Density and Shear Strength of Sands from CPT and DMT. *Geotechnical Special Publication*, 201–238. https://doi.org/10.1061/40659(2003)7

Jeremić, B., Jie, G., Preisig, M., & Tafazzoli, N. (2009). Time domain simulation of soil-foundation-structure interaction in non-uniform soils. *Earthquake Engineering and Structural Dynamics*, *38*(5), 699–718. https://doi.org/10.1002/eqe.896

Kabeta, W. F. (2022). Effects of full displacement pile installation on the stress and deformation state of surrounding soil: review. *Archives of Civil Engineering*, *68*(4), 445–466. https://doi.org/10.24425/ace.2022.143048

Kementzetzidis, E., Corciulo, S., Versteijlen, W. G., & Pisanò, F. (2019). Geotechnical aspects of offshore wind turbine dynamics from 3D non-linear soil-structure simulations. *Soil Dynamics and Earthquake Engineering*, *120*, 181–199. https://doi.org/10.1016/j.soildyn.2019.01.037

Kim, H. S. (2014). A Study on the Performance of Absorbing Boundaries Using Dashpot. *Engineering*, *6*, 593–600. https://doi.org/10.4236/eng.2014.610060

Kontoe, S., Zdravkovic, L., & Potts, D. (2008). An assessment of time integration schemes for dynamic geotechnical problems. *Computers and Geotechnics*, *35*, 253–264. https://doi.org/10.1016/j.compgeo.2007.05.001

Li, X., & Wang, Y. (1998). Linear representation of steady-state line for sand. *Journal of Geotechnical and Geoenvironmental Engineering*, *124*(12), 1215–1217.

Lysmer, J., & Kuhlemeyer, R. (1969). Finite dynamic model for infinite media. *ASCE Journal of the Engineering Mechanics Division*, *95*(EM4), 859–877.

Manzari, M. T., & Dafalias, Y. F. (1997). A critical state two-surface plasticity model for sands. *Géotechnique*, *47*(2), 255–272.

Manzari, M. T., & Dafalias, Y. F. (2004). Simple Plasticity Sand Model Accounting for Fabric Change Effects. *Journal of Engineering Mechanics*, *130*(6), 622–634. https://doi.org/10.1061/(ASCE)0733-9399(2004)130:6(622)

Massarsch, K. R., Wersäll, C., & Fellenius, B. H. (2021). Vibratory driving of piles and sheet piles – State of practice. *Proceedings of the Institution of Civil Engineers, ICE – Geotechnical Engineering*, *174*(1). https://doi.org/10.1680/jgeen.20.00127

McGann, C. R., Arduino, P., & Mackenzie-Helnwein, P. (2015). A stabilized single-point finite element formulation for three-dimensional dynamic analysis of saturated soils. *Computers and Geotechnics*, *66*, 126–141. https://doi.org/10.1016/j.compgeo.2015.01.002

Merchant, N. (2019). Underwater noise abatement: Economic factors and policy options. *Environmental Science & Policy*, *92*, 116–123.

Metrikine, A., Tsouvalas, A., Segeren, M., Elkadi, A., Tehrani, F., Sanchez Gomez, S., Atkinson, R., Pisanò, F., Kementzetzidis, E., Tsetas, A., Molenkamp, T., van Beek, K., & de vries, P. (2020). GDP: A New Technology for Gentle Driving of (Mono)Piles.

Nedwell, J., Turnpenny, A., Langworthy, J., & Edwards, B. (2003). Measurements of underwater noise during piling at the Red Funnel Terminal, Southampton, and observations of its effect on caged fish. *Report Reference: 558 R 0207*.

Negrut, D., Rampalli, R., Ottarsson, G., & Sajdak, A. (2007). On an Implementation of the Hilber-Hughes-Taylor Method in the Context of Index 3 Differential-Algebraic Equations of Multibody Dynamics. *Journal of Computational and Nonlinear Dynamics*, *2*, 73–85.

Newmark, N. M. (1959). A method of computation for structural dynamics. *Journal of the Engineering Mechanics Division*, *85*, 67–94.

O'Kelly, B., & Arshad, M. (2016). *Offshore Wind Turbine Foundations – Analysis and Design*. Woodhead Publishing. https://doi.org/10.1016/B978-0-08-100779-2.00020-9

Ong, C. L., Newcomb, D., & Siddharthan, R. (n.d.). Comparison of Dynamic and Static Backcalculation Moduli for Three-Layer Pavements. *Transportation Research Record*, *1293*, 86–92.

OpenSees Official Webpage. (2006). Retrieved August 9, 2023, from https://opensees.berkeley.edu/

Pisanò, F. (2022). Computational Soil Dynamics: One-phase problems - Lecture Slides, Soil Dynamics course, TU Delft.

Ramirez, J., Barrero, A. R., Chen, L., Dashti, S., Ghofrani, A., Taiebat, M., & Arduino, P. (2018). Site Response in a Layered Liquefiable Deposit: Evaluation of Different Numerical Tools and Methodologies with Centrifuge Experimental Results. *Journal of Geotechnical and Geoenvironmental Engineering*, *144*(10). https://doi.org/10.1061/(ASCE)GT.1943-5606.0001947

Ramírez, L., Fraile, D., & Brindley, G. (2020). Offshore Wind in Europe: Key Trends and Statistics 2019. Technical Report. *WindEurope: Brussels, Belgium*.

Ramírez, L., Fraile, D., & Brindley, G. (2021). Offshore Wind in Europe: Key Trends and Statistics 2020. Technical Report. *WindEurope: Brussels, Belgium*.

Rowe, P. W. (1962). The stress-dilatancy relation for static equilibrium of an assembly of particles in contact. *Proceedings of the Royal Society, Series A*, *269*, 500–527.

Roy, A., Chow, S., O'Loughlin, C., Randolph, M., & Whyte, S. (2020). Use of a bounding surface model in predicting element tests and capacity in boundary value problems.

Sánchez, S., López-Gutiérrez, J.-S., Negro, V., & Esteban, M. D. (2019). Foundations in Offshore Wind Farms: Evolution, Characteristics and Range of Use. Analysis of Main Dimensional Parameters in Monopile Foundations. *Journal of Marine Science and Engineering*, *7*(12), 441.

Schepers, W., Brinkgreve, R., & Appel, S. (n.d.). Recommendations on finite element modelling of non-seismic excitation in soil-structure interaction problems.

Schofield, A., & Wroth, P. (1968). *Critical State Soil Mechanics*. McGraw Hill.

Staubach, P., Machaček, J., Bienen, B., & Wichtmann, T. (2022). Long-term response of piles to cyclic lateral loading following vibratory and impact driving in water-saturated sand. *Journal of Geotechnical and Geoenvironmental Engineering*, *148*(11).

Strang, G., & Fix, G. J. (1973). *An analysis of the finite element method*. Prentice-Hall, Inc.

Sunday, K., & Brennan, F. (2021). A review of offshore wind monopiles structural design achievements and challenges. *Ocean Engineering*, *235*, 109409.

Tsetas, A., Tsouvalas, A., & Metrikine, A. (2023). A non-linear three-dimensional pile–soil model for vibratory pile installation in layered media. *International Journal of Solids and Structures*, *269*, 112202.

Upadhyaya, S. (2005). Stress-strain and Soil Strength. In D. Hillel (Ed.), *Encyclopedia of Soils in the Environment* (pp. 38–54). Elsevier. https://doi.org/10.1016/B0-12-348530-4/00507-5

van Rhijn, J. (2017). *Reduction of underwater piling noise: An optimization of the impact force to reduce underwater noise during the installation of a large sized monopile (Master's Thesis)*.

Wang, H., Lehane, B., Bransby, M., Wang, L., Hong, Y., & Askarinejad, A. (2023). Lateral behavior of monopiles in sand under monotonic loading: Insights and a new simple design model. *Ocean Engineering*, *277*. https://doi.org/10.1016/j.oceaneng.2023.114334

Watanabe, K., Pisanò, F., & Jeremić, B. (2017). Discretization effects in the finite element simulation of seismic waves in elastic and elastic-plastic media. *Engineering with Computers*, *33*, 519–545. https://doi.org/10.1007/s00366-016-0488-4

Wichtmann, T., Fuentes, W., & Triantafyllidis, T. (2019). Inspection of three sophisticated constitutive models based on monotonic and cyclic tests on fine sand: Hypoplasticity vs. Sanisand vs. ISA. *Soil Dynamics and Earthquake Engineering*, *124*, 172–183. https://doi.org/10.1016/j.soildyn.2019.05.001

Wood, D. M. (1991). *Critical states. In Soil Behaviour and Critical State Soil Mechanics*. Cambridge University Press - pp. 139-174. https://doi.org/10.1017/CBO9781139878272.007

Xie, M., & Lopez-Querol, S. (2021). Numerical Simulations of the Monotonic and Cyclic Behaviour of Offshore Wind Turbine Monopile Foundations in Clayey Soils. *Journal of Marine Science and Engineering*, *9*(9). https://doi.org/10.3390/jmse9091036

Yang, Z., Jardine, R., Zhu, B., Foray, P., & Tsuha, C. (2010). Sand grain crushing and interface shearing during displacement pile installation in sand. *Géotechnique*, *60*(6), 469–482. https://doi.org/10.1680/geot.2010.60.6.469

Zienkiewicz, O. C., Chan, A. H. C., Pastor, M., Schrefler, B. A., & Shiomi, T. (1999). *Computational Geomechanics with special Reference to Earthquake Engineering*. John Wiley and Sons.